ACTIVE FLOW CONTROL IN HIGH-SPEED INTERNAL FLOWS

A Dissertation
Presented to
The Academic Faculty

by

Abraham Naroll Gissen

In Partial Fulfillment
of the Requirements for the Degree
Doctor of Philosophy in the
School of Mechanical Engineering

Georgia Institute of Technology

May 2015

ACTIVE FLOW CONTROL IN HIGH-SPEED INTERNAL FLOWS

Approved by:

Professor Ari Glezer, Committee Chair
School of Mechanical Engineering
Georgia Institute of Technology

Professor Lakshmi Sankar
School of Aerospace Engineering
Georgia Institute of Technology

Professor Jechiel Jagoda
School of Aerospace Engineering
Georgia Institute of Technology

Bojan Vukasinovic, Ph.D.
School of Mechanical Engineering
Georgia Institute of Technology

Professor Mark Costello
School of Mechanical Engineering
Georgia Institute of Technology

James Mace, Ph.D.
Technical Fellow
The Boeing Company

Date Approved: January 23 2015

To Frada

ACKNOWLEDGEMENTS

This work was made possible through the support of both the Air-Force Research Lab (AFRL) and the Boeing Corporation.

I would like to thank my thesis adviser, Dr. Glezer, who has taught me a number of invaluable lessons over the years. I would also like to thank my thesis committee, Dr. Jagoda, Dr. Costello, Dr. Sankar, Dr. Vukasinovic and Dr. James Mace, Ph.D. Thank you for your time and assistance with this document. Thank you Dr. Vukasinovic also for your guidance and technical advice over the years.

This thesis would not have been possible without all of the help, support and assistance provided by the past and present members of the Fluid Mechanics Research Lab and for the unflagging support of my friends and family who sustained me throughout this process. I would also like to thank my soon-to-be-wife, Andrea, without whom many things in my life would not be possible.

TABLE OF CONTENTS

LIST OF FIGURES

CHAPTER 1

INTRODUCTION

1.1 Motivation

Flow separation over internal or external curved aerodynamic surfaces that is typically associated with adverse local pressure gradient is significantly exacerbated by compressibility effects and the appearance of shocks in transonic and supersonic flows. The complex interaction of the shock with the surface boundary layer can trigger flow separation within a short distance downstream (or at the shock) of the shock that is characterized and influenced by unsteady coupling between the separating flow and the shock. Flow separation is typically accompanied by profound changes in the flow structure and the associated pressure and shear stress distributions over the aerodynamic surface, and consequently by significant penalties in the performance of external (airframes) and internal (propulsion) aerodynamic systems. In external flows such shock-induced separation can result in drag due to the combination of separated flow and wave drag (Pearcey, 1959), flutter (Edwards, 1996) due to the global instabilities interaction with the structure, and degradation of the surrounding aero-optical environment (Gordeyev et al. 2013), while in internal flows within propulsion systems separation can result in catastrophic structural damage (Hadjadj and Onofri, 2009, Verma 2009).

The effects of shock-induced separation on an external aerodynamic surface was considered by Pearcey (1959) who investigated such interactions over a 10% thick R.A.E. 102 airfoil at $M = 0.83$ using pressure and force measurements, and showed shock induced global instabilities. These instabilities of the shock-induced separating flow over an airfoil can result in oscillatory changes in the aerodynamic loads and therefore transonic buffeting which can lead to catastrophic structural damage (Lee 2001, Crouch 2009). The time scales of these oscillations are long compared to the convective time

scale (Jacquin 2009) and can lead to excitation of low-frequency structural modes. Therefore, control of the transonic shock and the separating shear layer could expand the flight envelopes of high speed aircraft and provide higher safety margins for commercial aircraft.

The formation of shocks over aerodynamic bluff bodies can lead to three-dimensional, highly unsteady, separation. Beresh et al. (2013) investigated the unsteady motion of the shock and the induced changes in the flow field over a hemisphere and showed that the shock motion is driven by the downstream recirculation region feedback for strongly separated flows. These flow phenomena are particularly important in the use of airborne lasers systems that are typically housed in external turrets. Even at subsonic flight speeds ($M = 0.6$) a transonic shock that forms over such a turret leads to unsteady optical aberrations in the optical path that that are hard to control or correct for (Kyrazis, 2013). These aero-optical effects were investigated by Gordeyev et. al. (2013) who suggested that stabilizing these flows would improve the aero-optical environment. Vukasinovic et al. (2013) used active flow control of the separating flow at subsonic speeds to improve the aero-optical environment.

Compressible separation and shock formation also adversely affect the performance of propulsion systems. For example, the nozzles on the space shuttle's main engine are optimized for use in space and therefore are underexpanded during low altitude operation (eg. the shuttle main engine on startup). The resulting shock-boundary layer interaction often leads to separated flow within the nozzle (Hadjadj and Onofri, 2009), which is similar to the shock induced separated flow studied in this thesis. Shock induced separation in rocket nozzles causes non-uniform and unsteady flow leading to what is referred to as 'side-loads.' These side loads can be severe enough to cause structural failure (Nave and Coffey 1973), but designing nozzles which are robust enough to withstand these loads is not feasible due to the undesirable weight penalty (Verma, 2009). If the shocks could be stabilized (and thus stabilizing or even eliminating the side

loading) in some manner during this portion of the flight, significant weight and optimization (thrust at vacuum for given fuel burn rate) gains could be realized.

Compressible flow separation, and specifically shock-induced separation (and shock boundary layer interactions) have been investigated extensively over the past 40-50 years, with specific emphasis on their control using passive or active flow control approaches. This dissertation primarily focuses on active manipulation of the separating flow over a two-dimensional curved surface (using jet actuation) with the objective of exploiting the coupling between the separated flow in the presence of an upstream shock to indirectly control the shock. This control approach relies on the reciprocal (subsonic) coupling between the shock and the incipient separating flow, and the receptivity of the separated flow to fluidic actuation. Active flow control is used to modify the separated flow (by inducing partial attachment) and the pressure perturbations that accompany these changes couple to the shock through the subsonic flow and affect its static and dynamic characteristics.

1.2 Literature Review

1.2.1 Characteristics of Shock Boundary Layer Interactions

The flow physics of the interactions of shocks with surface boundary layers has been the subject of extensive investigations since the 1940s. The early investigations of Ferri (1939), Liepmann (1946, 1951) and Ackeret (1947) established details of the complex interaction of shocks with laminar and turbulent boundary layers at transonic speeds. The interaction of a shock with a boundary layer results in significant thickening of the boundary layer and may be accompanied by local flow separation downstream of the shock. Adamson and Messiter (1980) reviewed models of this complex shock boundary layer interaction with particular attention to the application of numerical and analytical models and their limitations when applied to a variety of shock related flows. An investigation of a supersonic shock over a compression ramp by Andreopoulos and Muck

(1987) showed that the interactions of shocks with turbulence can lead to substantial unsteadiness and deformation of the shock while the characteristic velocity, time- and length-scales of the turbulence change considerably.

The fundamental characteristics of transonic shocks have been the subject of numerous investigations. Liu and Squire (1987) used holographic interferometry to visualize a transonic shock formed over a curved surface, the induced separation, and illustrated the dependence between shock induced separation Mach number and local surface curvature. Delery (1983) measured the velocity and turbulence distributions using a hotwire probe near the wall in the presence of shock boundary layer interaction at transonic speeds. These extensive measurements of the boundary layer characteristics (e.g., streamwise velocity, turbulent kinetic energy and turbulent shear stress) allowed for validation of turbulence models. Sartor et al. (2012) investigated shock-induced separation over a curved surface using PIV, showing the evolution of a number of parameters (velocity, Reynolds shear stress, 2D kinetic energy) that are relevant to the evolution of the shock induced separated shear layer.

The influence of shocks on transonic flow over airfoils has been of much interest due to unfavorable flight characteristics of traditional subsonic airfoils at high transonic speeds. Much of which was investigated initially by Pearcey and Holder, (1954) showing separation and the potential for flutter of the control surfaces, similar to subsonic separation, and a number of these issues were alleviated following the adoption of supercritical airfoil design.

The separation over an airfoil at transonic speeds was categorized by Pearcey (1954) according to the severity of the shock-induced separation. These categories are shown in a series of sketches that were reproduced by Babinsky and Harvey (2011), and are included for reference in Figure 1.1. Figure 1.1a shows a shock that is preceded by a supersonic bubble upstream (enclosed by the dashed line and marked $M > 1$) at low free stream Mach numbers, where the shock does not impart a strong enough pressure change

to separate the flow. As the free stream Mach number increases, the shock wave causes the flow downstream to separate (due to a reduction in momentum and the flow inability to overcome the adverse pressure gradient, Figure 1.1b), which can reattach before reaching the trailing edge of the airfoil. At higher speeds (Figure 1.1c) the pressure ratio across the shock increases which increases the severity of the separation, and eventually, the flow does not reattach upstream of the trailing edge of the airfoil (Figure 1.1d). As the free stream Mach number increases (Figure a-d), the size of the upstream supersonic bubble tends to increase. In external flows, such as the one shown here, disturbances which originate downstream (from the shear layer, from the mechanical oscillation of trailing edge etc) can propagate upstream either by traveling around the supersonic bubble in the subsonic free stream or through the boundary layer. In internal flows (as in the present work), an increases in the size of the supersonic bubble with increasing Mach number eventually leads to supersonic flow across the entire span of the duct. This condition of supersonic flow spanning the facility is referred to as choking and disturbances downstream can propagate upstream only through the (subsonic) boundary layer. Further discussion of the flow field at transonic speeds is given by Nixon et al. (1989).

1.2.2 Manipulation of Transonic Shock Waves using Flow Control Approaches

The adverse effects of the formation of shock waves in external and internal flows have prompted much interest in a number of passive and active flow control approaches for the mitigation of these effects. This review of some of the flow control devices applied to the control of shocks is organized into passive and active flow control with a focus on methods that aim to effect the shock (shape, position, affected drag) or the resulting separation (reattachment, upstream boundary layer modification etc).

Passive flow control

Passive flow control is typically effected in the absence of external power. Conventional passive flow control approaches (slots and vortex generating vanes) with the aim of

controlling the boundary layer characteristics upstream of the shock (reenergizing the boundary layer through the introduction of streamwise vorticity) applied to a variety of flows (transonic and supersonic) suffering from adverse drag effects due to shocks were reviewed in detail by Pearcey (1954) including an overview of airfoil shapes including supercritical airfoils which are better suited than traditional airfoils in the transonic regime. In a more recent review of shock interactions with turbulent boundary layers in both internal and external flows, Delery (1985) described the general nature of the interaction and reviewed a number of flow control strategies. He discussed both passive (vortex generators and local changes in surface contour) and active (suction, blowing, bleed and surface cooling) control, both of which were aimed at reducing the adverse effects associated with the shock foot interaction domain (instabilities, drag, incipient separation etc.) while avoiding large increases in shock strength which are sometimes associated with changes in the local pressure field imparted by the flow control. Delery (1985) noted that some of these techniques can be used to either modify the boundary layer upstream of the shock (e.g. vortex generating vanes) to increase its "resistance" to separation (by energizing the boundary layer) or can be applied underneath the shock using porous surfaces or cavities immediately downstream of the interaction domain of the shock foot in order to provide a pathway for feedback between the upstream and downstream side of the shock.

Passive flow control devices have also been used to mitigate the adverse effects of shock in other geometries (i.e. not airfoils). The study of mitigation of the unsteady effects of shock induced separation was further studied by Barter and Dolling (1993). In an experimental study performed in a compression corner at M = 4.92, they demonstrated that a doublet array (a stacked array modified ramp type vortex generator (wheeler type))placed upstream of the compression corner was effective in reducing the RMS fluctuations of pressure downstream from the shock as well as reductions in fluctuations in the shock position. The use of passive devices at higher Mach number to reduce the

unsteadiness of the shock induced separation was demonstrated, and further illustrates the efficacy of streamwise vorticity production for the control of these types of flows. Holden and Babinsky (2007) showed that both ramp and vane type vortex generators (having characteristic height and spacing that are 0.6 boundary layer thickness) suppressed separation induced by a shock within a 2-D duct (178 mm x 114 mm) at $M = 1.5$. However, these authors noted that VGs placed directly underneath the shock, while effective at reducing separation, led to an increase in wave drag generated by the shock.

Vortex generators that are placed upstream of the shock (ramps and paired split ramps of various configurations) were used in a numerical investigation by Lee et al. (2011) who demonstrated suppression of incipient shock induced separation of the flow over an airfoil-like curved surface at $M = 1.3$. Applications of passive devices at transonic speeds were demonstrated by Gordeyev et al. (2013) who used a passive fence placed upstream of a wall mounted half cylinder at $M = 0.54$. The authors reported that the shock was not observed with the fence in place. The lack of shock consequently improved the aero-optical environment of the shock-induced separated flow, as the density gradient associated with the shock is no longer present. For a more comprehensive review of passive flow control devices please see a recent review by Babinsky and Harvey (2011), that includes a comprehensive discussion of shock boundary layer interactions and their control through passive devices (bumps, vortex generators, cavities) and includes a number of the works discussed above.

Active Flow Control

Active flow control that is based on externally-powered (electromechanical, pneumatic, or chemical) actuation has become prevalent over the past several decades because it not only affords high control authority but also enables regulation of the actuation in both open and closed loop control.

Several investigators have considered mitigation of shock-induced separation by modification of the boundary layer upstream of the shock using continuous active suction and/or blowing. Wallis and Stuart (1958) demonstrated the use of a spanwise array of nine round vortex generator jets of diameter 0.020" emanating normal to the surface upstream from the shock on an airfoil-shaped bump on the surface at transonic speeds in order to attach the shock induced separated flow. These authors showed that streamwise vorticity concentrations generated by these jets have favorable effects both upstream and downstream of the transonic shock, in terms of reenergizing the boundary layer upstream from the shock, as indicated by a reduction in the propensity for separation downstream from the shock as visualized by schlieren. It is noteworthy that this control approach leads to streamwise displacement of the shock due to the reduction in the separation domain. The vortex generating jets were found to translate the shock along the surface and move the separation point. Flow control placed downstream of the shock boundary layer interaction was explored by Englar (1970) who investigated several blowing strategies applied to a variety of trailing edge geometries on elliptic airfoils at transonic speeds (M = 0.3-0.9) and showed that tangential blowing of a 2-D slot jet over an elliptic trailing edge provided the best performance with regard to improved lift and reduced drag.

In a review of shock interactions with turbulent boundary layers in both internal and external flows, Delery (1985) described the general nature of the interaction and reviewed a number of flow control strategies. He discussed both passive (vortex generators and local changes in surface contour) and active (suction, blowing, bleed and surface cooling) control, both of which were aimed at reducing the adverse effects associated with the shock foot interaction domain (instabilities, drag, incipient separation etc) while avoiding large increases in shock strength which are sometimes associated with changes in the local pressure field imparted by the flow control. Delery (1985) noted that some of these techniques can be used to modify the boundary layer upstream

of the shock (through suction for example) to increase its "resistance" to separation (by energizing the boundary layer). Delery also reported that suction applied in the shock interaction domain (where the shock interacts with the boundary layer) reduces the propensity for the shock to separate the flow, decreases the interaction domain, and increases the shock strength. Delery pointed out that the application of suction directly downstream from the interaction region is more efficient (changes imparted for the energy used in the flow control devices) and has similar (but less efficient) affects as when the suction is applied upstream.

Further investigation of upstream boundary layer modifications were investigated by Krogmann et al. (1985) who demonstrated that suction (single slot, double slot, and a perforated strip) upstream of a normal shock over an airfoil (supercritical airfoil VFW-VA-2) in transonic flow at off-design conditions (i.e., an airfoil that is not optimized for transonic speeds) could lead to reduction in boundary layer thickness and improved the overall aerodynamic performance through changes in shock location, lift, drag and delayed separation downstream of the shock. The authors reported that this actuation method suppressed buffet, and therefore can be used for reduction of buffet-excited flutter. These authors noted that even the presence of the inactive suction slots (and underlying cavity) had led to significant reduction in separation and buffeting ostensibly due to cavity feedback (i.e. vortex shedding from the cavity driven flow). Wave drag, which is the added drag due to the presence of a shock, is generally reduced on external aerodynamics through the use supercritical airfoils. Additionally flow control devices are sometimes deployed to mitigate wave drag effects. The work that has been done at developing flow control techniques to control wave drag often have added benefits including reduced shock unsteadiness. Flow control techniques for reduction of wave drag over variety of airfoil shapes in transonic flow M = 0.5-1.8 were explored as part of the EuroShock II project (Stanewsky et al. 2002). This project involved both internal and external flows, with one of the goals being reduction in wave drag. One method studied

used slots and porous surfaces combined with suction applied at various locations both inside and outside of the slot. Depending on location and suction rates, this approach was effective in reducing wave drag and improving lift over several of the airfoil configurations examined. High suction rates (compared to the free stream momentum) applied directly beneath the shock were found to reduce some of the large scale unsteadiness associated with the shock induced separation.

Souverein and Debieve (2010) continued the investigation of the use of actuation placed upstream from the shock using a spanwise array of continuous round jets (10 jets distributed across 100mm) for generation of concentrations of streamwise vorticity in order to suppress boundary layer separation induced by an incident shock impinging on a flat surface at supersonic speeds ($M = 2.3$), and noted that the reduction in the characteristic scale of the separation bubble generated by the shock was accompanied by an increase in the frequency of the energetic spectral components of the reflected shock (as measured by hot wire and PIV measurements).

Other geometries (i.e. not airfoils) have also seen the application of active flow control devices. For example, the effectiveness of novel flow control actuation technologies (plasma, thermally driven synthetic jets etc.) for the control of shock boundary layer interactions has been investigated by a number of researchers. Kalra et al. (2006 and 2009) conducted numerical and experimental studies of the effects of magneto-gas dynamic plasma actuators on an incident shock with a resulting separation bubble. They reported a decrease in the size of the separation bubble in the shock induced separated region with best results when the plasma actuator was positioned at the point where the shock impinged on the boundary layer. Control of the motion of a shock formed by a compression ramp ($M = 3$) flow was demonstrated by Narayanaswamy et al. (2010). An array of eight thermally driven synthetic jets (using electric discharge in a cavity) used to lock shock-wave oscillations to the jet pulsating frequency (about 2 kHz) indicated potential for shock stabilization through forcing the shock position at controllable

actuation frequencies. Work on flow control devices both upstream and downstream from a transonic shock induced separation was explored by Vukasinovic et al. (2013) with two active flow control approaches on a wall mounted curved surface, upstream (of the shock) normal blowing and downstream (of the shock) tangential blowing using an array of fluidic oscillating jets to control a transonic shock and its coupled flow separation. An emphasis was placed on the large scale unsteadiness of the separated flow and the streamwise motion of the shock with the main findings revolving around the ability to control the shock position through acting on the downstream separated flow.

1.2.3Flow Control Technologies

This section reviews flow control actuation technologies that are relevant to the present investigations, namely pulsed jets and fluidic oscillators. For a comprehensive review of flow control devices please see Cattafesta and Sheplak, (2010).

Arrays of pulsed jets (e.g., Cattafesta and Sheplak, 2010) issuing through arrays of orifices at the flow boundary have been used to effect time-periodic flow actuation mostly for separation control and are typically regulated by a fast response valve (e.g., a piezoelectrically driven valve, Kudar, 2007). In the presence of a cross flow over a surface, the pulsed jets generate a periodic streamwise vortex with a sense that is determined by the slant and skew of the exit orifice as the sense of the shear is a function of both the azimuthal angle and direction with respect to the local flow in the boundary layer(Kostas et al. 2007). Earlier works have demonstrated that time-periodic actuation by streamwise vortices can delay flow separation over airfoils and flaps and improve their aerodynamic performance at low speed ($M < 0.2$, e.g., Seifert et al. 1993). However, the utility of this approach has also been extended to higher Mach numbers in the presence of compressibility effects ($0.1 < M < 0.5$), e.g., McManus and Magill, 1996). Pulsed jets have also been applied for control of separation in internal flow applications (e.g., turbine blade cascades, Bons et al. 2001,).

Unlike pulsed jets that require a control valve, fluidic oscillating jets (also known as sweeping jets)produce oscillating jets without any moving parts. The unsteadiness of the jets is generated by unstable interaction between two air streams. There are a number of different geometries which generate these types of oscillating jets which have been studied extensively by Arwatz et al. (2008), Gregory (2013) and Ragu (2013).

Fluidic oscillators are attractive for flow control applications because they introduce a large amount of small scale structures, thus providing efficiency (power, air usage etc.) improvements when compared to traditional steady blowing techniques, due to the enhanced mixing introduced by the oscillations of the jets. DeSalvo et al. (2010) demonstrated suppression of separation using fluidic oscillating jets in order to increase the lift generated by simplified, lightweight, flaps (through reattachment of the flow over the flap) for use on commercial aircraft. Fluidic oscillators have also been used for improving rudder control through suppression of separation in order to delay stall and improve 'lift' performance (Roman et al., 2012). Fluidic oscillators were also used for suppression of cavity flow oscillations by breaking up the main shedding frequency which can often excite destructive structural modes (Raman and Raghu 2004). Finally, Vukasinovic et al, (2013) used fluidic oscillators for controlling the evolution of the shear layer that is formed by shock induced separation.

Synthetic jets which generate a 'train' of self-advected vortex rings, synthesized from the surrounding fluid, have been used extensively for separation control in external and internal flows. Unlike fluidic oscillators and pulsed jets, synthetic jets do not require a fluid (air) source and are engendered from the ambient fluid. The details of the flow physics of these jets and their operation has been documented in numerous publications (e.g., Smith and Glezer, 1998, Glezer and Amity, 2002, Holman et al., 2005), as well as their application to flow control (e.g., Amitay et al., 1998, Honohan et al., 2000). A more recent review of the use of synthetic jets in flow control can be found in Glezer (2011). While their utility for flow control on commercial aircraft has been considered (e.g.,

Kibens and Bower, 2004), a significant challenge has been their effectiveness in high speed flows. Several investigators (e.g., Gilarranz et al., 2005, Crittenden and Glezer, 2006) explored the development of high-speed, compressible synthetic jets that are formed by piston drivers driven by electric motors, which led to the generation of high momentum jets.

In the present dissertation pulsed jets are used for imparting rapid stepwise changes in the downstream boundary conditions as well as pulsed actuation (Chapters 5 and 6), fluidic oscillators are used for quasi-steady control of the separated shear layer for both for subsonic and supersonic flows (Chapter 4 and 7), and high-speed synthetic jets are used for the control of secondary flows (Chapter 8).

1.3 Thesis Structure

1.3.1Fundamental Questions

The primary goal of the present dissertation is to address the following fundamental questions:

1. *Can flow separation over diverging curved surfaces in internal flows be effectively controlled at elevated subsonic Mach numbers?*

   Separation control has been primarily investigated in external flows and less so in internal flows (cf. section 1.2.). The present focus is to demonstrate the fundamental control aspects of separation in an adverse pressure gradient within the canonical internal flow geometry considered in the present dissertation.

2. *Can transonic shock induced separation be controlled using the present (momentum-based) active flow control approaches? If so, can control of the coupling between the separation and the shock be exploited for manipulation of the shock structure and stability?*

   To begin with, the viability of the flow control technique must be established. The relationship between the shock position and the flow control parameters (jet

strength, timing, response time, etc.) is important both from a practical engineering perspective and to gain an understanding of the underlying mechanism of action.

3. *How is the coupled separation/shock flow affected by the magnitude of the actuation?*

   A major advantage of a momentum-based active flow control solution is the ability to control the magnitude of the actuation. Quantification of the dependence between the effects of the flow control and the supply momentum elucidates trends that are essential not only to the eventual engineering application of such devices but also provides further insight into the underlying mechanism of action of the flow control.

4. *What are the characteristic time scales that are associated with the response of the flow (separation and the upstream shock) to the indirect actuation? Specifically, what is the characteristic response to the onset and termination of the actuation?*

   The time scales associated with the flow response to temporal step changes in the actuation yield information on the inherent dynamic characteristics of flow. Specifically, these time scales are characteristic of the shock response to the actuation and therefore understanding of the mechanisms of flow controls interaction with the base flow. This understanding is crucial for implementation of a successful real-time controller and these parameters should be investigated over a range of speeds.

5. *How do the time scales associated with the flow affect repeated (time-periodic) actuation?*

   Repetitive, time periodic actuation might give rise to hysteresis effects in the controlled flow in terms of the shock response to the actuation. These effects provide insight into the fundamental characteristics both of the method of action (pulsed flow control) and of the parameters which would be used for the deployment of a closed loop flow control system.

6. *How can the flow control concepts developed in the dissertation be applied to challenging transonic flow effects in practical systems?*

The concepts developed in the work on transonic shock waves need to be extended to encompass other geometries and flow regimes in order to demonstrate the flexibility and applicability of such developed concepts.

1.3.2 Overview of Thesis Structure

The present dissertation focuses on fundamental understanding of the effects of flow control in high speed internal flows with emphasis on active manipulation of the separating flow over a two-dimensional curved surface in the absence and presence of a transonic shock. In the presence of a shock, the objective is to exploit the reciprocal coupling between the separated flow and the upstream shock to indirectly control the shock position and stability.

This document begins with an introduction and literature review (Chapter 1) that is followed by a discussion of the experimental setup and specifically of the basic flow duct with a curved surface insert that is used for the fundamental investigations of the control of the separating shear layer using fluidic actuation (Chapter 2). The evolution of the transonic base flow is discussed in Chapter 3.

Chapter 4 discusses the manipulation of the reciprocal (subsonic) coupling between the shock and the incipient separating flow, and the receptivity of the separated flow to fluidic actuation are investigated using quasi-steady high-frequency actuation. The modification of the separated flow (by inducing partial attachment) couples to the shock and affects its static and dynamic characteristics.

The following segment of the investigation presented in Chapter 5 focuses on the temporal transition between the quasi-steady flow states. Transitory effects measured and presented in this chapter provide assessment of the time scales associated with the shock motion and therefore the bandwidth that would be required from future flow control systems.

Chapter 6 focuses on extending the work done in Chapter 5, with specific emphasis on the timing of repeated flow control actuation pulses. Examination of hysteresis associated with actuation frequency at different pressure ratios provides some insight into both the mechanism of the shock motion and the dynamics of the transonic flow field.

The concepts developed in Chapters 4-6 are applied to other challenging flow applications. In Chapter 7 the approach used for mitigation of the separation over a 2-D curved surface in Chapter 4 is extended to a three dimensional geometry. It is demonstrated that this approach can significantly decrease the losses through a complex reverser duct at Mach numbers up to 0.5. A second example is included in Chapter 8 which explores the concept of controlling the dynamics of an unsteady and unstable secondary flow in an offset diffuser duct at Mach numbers up to 0.5.

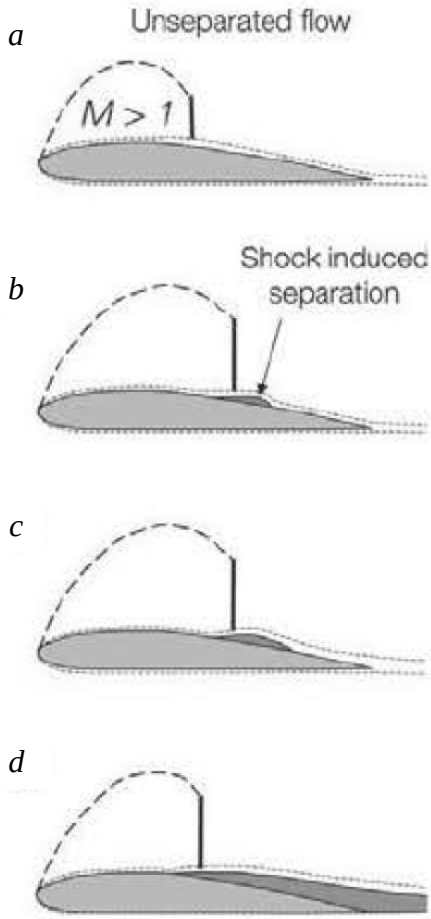

Figure 1.1 *Transonic shock induced separation as characterized by Pearcey (1954) and reproduced by Babinsky and Harvey (2011), for increasing oncoming Mach number (a-d).*

CHAPTER 2

EXPERIMENTAL SETUP

This chapter describes the experimental apparatus and techniques that were used in investigations of the coupling between the separated flow over a two-dimensional curved surface in the absence and presence of an upstream transonic shock and the use of active flow control to manipulate the separation for indirect control of the shock. As noted in Chapter 1, this approach was also applied in two applications, namely mitigation of the losses through a complex reverser duct (M = 0.5, Chapter 7) and control of the dynamics of the secondary flow in an offset diffuser duct (M = 0.5, Chapter 8). The experimental apparatus that was used in each of these two investigations are described separately in these Chapters.

2.1 The High-Speed Wind Tunnel

The primary experiments were performed in a small, open-return pull-down high-speed subsonic wind tunnel that is driven by a speed-controlled 150 HP blower fan. A cartoon of the Georgia Tech high speed tunnel is shown in Figure 2.1. The air is drawn into a contraction (Figure 2.1a) that has a 1.8m square entrance and a 12.7 cm square exit, creating a decrease in cross section that occurs over 2.1m. The air is then drawn through the test section (Figure 2.1b). The test section is 0.7m long and nominally 12.7cm square, and, in this configuration, the facility can sustain speeds of M = 0.74. In order to attain higher speeds, a curved insert (Figure 2.3a) is installed into the upper surface of the test section. A cartoon of the test section with a sample curved insert installed is shown in Figure 2.2. Following the air passing through the test section (Figure 2.1b), the air is drawn into a (4.8m long) expansion (0.7m square) which has padded walls and a 90 degree bend. These features in the expansion (Figure 2.1c) are present in order to

minimize the amount of noise generated by the fan that is propagated upstream to the test section. After the air is drawn through the first half of the wind tunnel (Figure 2.1 a-c), it passes through the fan (Figure 2.1d) and is forced through a muffler section (Figure 2.1e). This muffler section is 5.5m in length and is annular in cross section with the center section and outer section packed with mono-filament fiberglass to absorb the acoustic energy in the system and reduce the noise generated by the facility. Finally, the air is forced through a water cooled heat exchanger (Figure 2.1f) that was designed to reduce the exit air temperature to ambient conditions.

A schematic of the test section is shown in Figure 2.2a. The schematic illustrates the curved surface used to generate higher speed flow on the upper surface of the flow path, and the static chamber above the flow path is used to house flow control actuators so that they are not exposed to atmospheric pressures. The sidewalls of the test section (removed in this view for clarity) are made of 25.4mm thick Lexan. Due to the optical aberrations in the plastic, two (one in both windows) float glass inserts were embedded into the windows to aid with the schlieren visualizations.

Calibration of the flow through the facility begun with the installation of two static pressure ports and a temperature probe which were integrated into the tunnel wall both for calibration and monitoring purposes. The static pressure port, p_i, and temperature sensor (thermocouple) are positioned immediately downstream from the tunnel inlet contraction (Figure 2.1a) on the bottom wall. The second pressure port, p_e, is placed just upstream from the test section (Figure 2.1b) exit plane on the bottom wall. The flow rate through the duct is calibrated using a pitot probe at its center with all four walls of the test section flat (i.e. no surface curvature present). This pitot probe is removed once the relationship between the static pressure(s), p_e, p_i, and the Mach number at the inlet of the contraction is determined. The calibration is done relative to the pressure drop across the inlet contraction ($\Delta p = p_{atm} - p_i$) and is shown non-dimensionalized by the atmospheric pressure in the lab during the acquisition of the data (p_{atm} = 98584Pa) in Figure 2.2b.

During further data acquisition, the pressure ratio across the test section (p_i/p_e) is used to set up the flow through the test section and ensure that the variety of tests performed in this facility were all run at the same conditions.

2.2 The Test Surface Insert

In the present experiments, the top wall of the test section (Figure 2.2a) is fitted with a converging-diverging curved test surface insert that is comprised of a gradual converging ramp and a diverging section that terminates at the surface of the test section. The geometry of this insert is shown in Figure 2.3. The coordinate system used throughout the work performed in this wind tunnel (Chapters 3-6) uses a coordinate system where the origin is at the apex of the contraction and positive x and y ordinate values are defined as streamwise and cross stream respectively. The convex insert is designed to generate a transonic shock and shock-induced separation when the cross flow is fast enough to generate a shock (p_i/p_e<1.28). The surface smoothly and tangentially forms a contraction with a height of H = 20mm at the apex of the curved surface at x/H = 0. Downstream of the apex the surface has a radius of 4H and extends to L = 2.6H(x/H = 2.6) past the apex. The insert model is comprised of three streamwise sections. The upstream section forms a fixed segment, the ramp, the center section is the main interchangeable (labeled as the flow control insert) section that houses the flow control hardware, and the downstream section blends into the test section wall.

The flow over the curved insert is characterized using a variety of instrumentation devices the location of which is shown in Figure 2.4. The insert model is instrumented with a streamwise array of 15 static pressure ports, not shown, (p_1 through p_{15}) along its centerline ($2 < x/H < 2$) and high frequency pressure sensors p_{d1}, p_{d2}, p_{d3}, p_{d4}at x/H = -2.95, 3, 4 and 5, respectively), as shown in Figure 2.4. The location of the static pressure taps are defined relative to the apex of the insert (x/H = 0). The static pressure is presented in terms of the compressible pressure coefficient C_p, for which the reference

pressure p_{ref} (Figure 2.3) and the Mach number M(measured at the inlet of the test section with a pitot probe) are used as the reference parameters. The static pressure distributions are measured using an Esterline 98RK-1 pressure scanner with 34.47kPa 9816 modules. Each static pressure measurement is an average of 125,000 samples. The accuracy of the D200 sensors in the 9816 module is within 52Pa (0.1% of full scale).

The dynamic pressure sensors p_{d1}, p_{d2}, p_{d3}, and p_{d4}, are flush-mounted to the surface in the locations shown in Figure 2.4. Meggit 8510B-5 pressure transducers are used to measure the dynamics of the pressure at these locations in the facility. The accuracy of these transducers is ± 0.2% of full scale. The upstream sensor (p_{d1}) is used for monitoring the pressure fluctuations in the oncoming flow while the downstream sensors ($p_{d2\text{-}4}$) monitor the pressure fluctuations within the separated flow domain downstream of the curved insert. Due to the nature of the results discussed in Chapter 3, it was decided to move the dynamic pressure sensor in the 'p_{d1}' position downstream for the testing conducted in Chapter 4 and 5. The three dynamic pressure sensors considered in Chapter 4 and 5 are flush-mounted along the centerline and labeled as p_{d2}, p_{d3}, and p_{d4}, at x/H = 3, 4 and 5, respectively (Figure 2.4).

The flow through the test section is characterized over the full range of available facility conditions(up to p_i/p_e = 1.41) by the static pressures, p_i and p_e, that are located at the inlet and outlet of the test section, respectively. These pressure are used as references in order to define the flow state through the facility and are shown in terms of the pressure ratio p_i/p_e in Figure 2.5. Both p_i and p_e decrease with increasing tunnel speed until the upstream pressure begins to level, which indicates that the test section becomes choked and its mass flow rate becomes invariant. Further increase in the blower suction only lowers the back pressure as illustrated by the continued decrease in p_e when p_i is invariant (marked in red in Figure 6a). After the test section flow becomes choked, the upstream pressure becomes invariant and, instead of using the upstream Mach number as a reference parameter, the pressure ratio, p_i/p_e, is used to characterize the upstream flow

over the entire flow range, as shown in Figure 2.5b,characterizing the dependence of the test section Mach number on the pressure ratio, p_i/p_e, up to the choking condition (dashed line).In the pulsed-jet flow control applications (Chapter 4 and 5), the flow control elements precluded the installation of the static pressure taps along the curved elliptic surface. Therefore, the static pressure ports along the flow control insert were not present for those tests. Instead, the downstream, interchangeable section had five static pressure ports installed along the model centerline at x/H = 3.4, 4.5, 5.5, 6, and 6.6.

2.3 The Particle Image Velocity (PIV) System

A schematic of the PIV system is shown in Figure 2.6. The laser (Figure 2.6a) illumination was provided by a Quantronix Darwin Duo YLF laser which is capable of a double pulse up to 4kHz. The light is then sent through two spherical lenses (Figure 2.6 b and c, focal length of 100mm and 300mm) with the first lens used to mitigate beam divergence. The light sheet is generated using a cylindrical lens (focal length of 125mm) after which the light sheet is turned vertically (using a 10.16cm diameter mirror) and passed through the bottom of the test section, Figure 2.6f (cf. Figure 2.2a). The flow is visualized using a high speed Vision Research Phantom V.2 camera which records the illuminated fields. In order to improve the optical quality of the measurements (both PIV and schlerien, please see section 2.4), glass optical windows are installed in the side of the test section (not shown). In Chapters 3 and 4, each set of data is recorded at 3,133 Hz and the time average flow fields and the statistics derived from the instantaneous velocity fields are based on ensembles of 2,700 image pairs. In Chapter 5, the PIV is taken at 2.7kHz (in order to capture events which occur over longer time scales), with each phase being the average of about 500 phase-locked fields, whereas the time averaged fields are averages of 2,700 image pairs. As the surface described in Figure 2.3 is on the upper test section wall, all PIV flow fields are shown in an inverted view, for convenience. The field of view for the schlieren (see section 2.4) and PIV is shown in Figure 2.7, where the

extents of the PIV ($0.5 < x/H < 3.52$, $-0.8 < y/H < 2.1$) and the schlieren setup (similar extents) are shown.

Due to the high laser intensity necessary for the high-speed PIV, intense surface reflections masked the flow immediately near the surface in spite of surface anti-reflective treatments. Therefore, all the measured flow fields exclude the near-wall region (a region of approximate thickness $0.3H$) which is masked in the present measurements. Also, the PIV field of view extends across the edge of the glass optical window(see discussion of test section Figure 2.2),and, therefore, the edge of the field of view is not resolved and is masked as well.

The present planar high-speed PIV measurements are used to extract the instantaneous position of the shock (Figure 2.8a). To extract the shock position, the horizontal component of velocity is first plotted at each discretized elevation, y/H, such as the one marked by the dashed line in Figure 2.8a. The corresponding instantaneous velocity traces are shown in Figure 2.8b in grey, with the average velocity overlaid in red for clarity. All velocity fields are shown relative to the reference velocity U_{ref} of the oncoming flow when the flow is choked (cf. Figure 2.5). U_{ref} is the velocity at the inlet of the test section where the cross section is 12.7cm square. When a shock is present in the flow field, the velocity increment across the shock is quite distinguishable. For a given realization (i.e., snapshot of the flow field), the shock position for each elevation (~36 points per H, discretized by the PIV vector grid),y/H, is defined by finding the minimum slope within the velocity 'jump' region. A curve is fit to the velocity profile across the shock and the first derivative is taken; the minimum slope is taken as an approximation of the shock location. Shock positions associated with the velocity traces (Figure 2.8b) are shown in the form of a histogram in Figure 2.8c, where $n_i = N_i/\sum N_i$.N is the number of measured shock positions for each spatial bin $\Delta x/H$. The bin spacing was arbitrarily selected to provide a balance between the number of samples per bin and characterization of the distribution. The bin spacing was kept constant throughout all

characterizations of the shock position for the PIV. This process is repeated for all elevations, y/H, in each PIV realization, and the positions are displayed on top of a time-averaged raster plot of the time averaged flow (Figure 2.8a) which also illustrates a full domain of the shock motion for a given flow condition. The shock motion can be characterized by calculating various statistics based on the shock position.

The particle image velocity is computed using DaVis 8.1. The processing scheme uses a round integration window with multi-pass and decreasing interrogation window size. In this case, the window decreased from 48x48 to 16x16 with 50% overlap and 5 passes for each size was used in order to fully resolve the sharp gradients associated with the shock.

There are a number of sources of error for PIV (as addressed by Adrian and Westerweel, 2011). In order to quantify the error associated with the PIV in this thesis, the RMS of the velocity is calculated over 2,700 velocity fields for a variety of locations within the field of view and a range of pressure ratios. The RMS is the sum of the error in the determination of the velocity plus the turbulent fluctuations. With this in mind, the RMS of the velocity field was calculated at a position of $y/H = 1$ and $x/H = 0$, where the flow is known to be supersonic and, due to the short inlet, the turbulence levels are considered to be very small. As such, the turbulence in the flow at the apex away from the surface can be considered nominally zero. The average RMS (non-dimensionalized by the average velocity at that point), calculated over 10 data sets (each with 2,700 images) at ($y/H = 1$ and $x/H = 0$), was found to be 0.1%. This was considered to be the error associated with the PIV measurements.

2.4 The Schlieren System

The flow fields were also characterized by schlieren visualization, where the field of view is centered about the aft section of the test surface over approximately the same extents as the PIV ($0.5 < x/H < 3.52$, $-0.8 < y/H < 2.1$), shown schematically in Figure 2.7. The schlieren visualization system is shown in Figure 2.9. The light is generated by a light

engine (Microscope LED Illuminator, Metaphase MP-LED-150, Figure 2.9a) generally used for lighting microscopes. The light generated travels to the collecting optics through a 'liquid' light guide (not shown). The collection optics (Figure 2.9b) are a microscope objective where the light travels through the objective providing a very small focal spot. In order to cut off the optical aberrations associated with the light guide (and light engine), the light passes through an 800 μm pinhole (Figure 2.9c). Next, the light is collimated by the primary main lens (Figure 2.9d) after which the light passes into the test section (Figure 2.9f) through a glass insert (Figure 2.9e) that was installed into the Plexiglas windows in order to improve the optical performance of the system. The collimated light interacts with the density gradients in the test section (Figure 2.9f) before exiting through a second glass insert (not labeled). The collimated light is collected by a secondary lens (Figure 2.9g, identical to the primary lens) after which it passes by a knife edge (Figure 2.9h) before being collected by the camera.

The single-pass schlieren system utilizes a continuous light source. For the data presented in Chapters 3 and 5, the schlieren images were captured with a PCO-tech Pixelfly camera (14 bit, 1392 x 1040) at a rate of 15 Hz with an exposure of 5 μs. In the results presented in Chapter 4 the schlieren images were recorded by the Phantom v.2 camera at 8 kHz frame rate as the highest time resolution of the shock transient motions was sought to be resolved.

There are two methods used in this thesis to determine the shock position, applied to both the PIV and schlieren measurements. Despite the inherent differences between these measurement techniques, the statistical method used to extract the shock position is similar for both (cf. Chapter 2 Figure 2.8 and Chapter 5, Figure 5.6). Given that a Gaussian curve fit is used to find the most probable shock location for both techniques (PIV and schlieren), it is possible to use the Gaussian fit parameters to estimate the RMS values and, thereby, the maximum error associated with this technique. For both methods, the Gaussian fit parameters indicate that w/H = 0.05-0.17, where w is the

distance from the time average location of the shock to the location that corresponds to the 95% confidence interval. As this is the RMS summed with the turbulence, it is considered an upper bound of the error associated with the measurements of the shock position. Additional details about the application of schlerien quantification of the shock position are presented at the beginning of Chapter 4.

2.5 Flow Control Actuators

In the present investigations, the evolution of the flow over the curved test surface is controlled by manipulation of separation on the aft section of the insert with specific emphasis on exploiting control of shock-induced separation to affect the dynamic characteristics of the shock. The investigations described in Chapters 4 utilize fluidic actuation based on oscillating jets, while the investigations in Chapters 5 and 6 are based on pulsed jets.

2.5.1 Fluidic Oscillator Jet Actuators

For the study presented in Chapter 3, instead of passive control devices typically used in the control of transonic shock (Hoden and Babinski, 2007), the present work utilizes their fluidic counterpart, namely, fluidic oscillating jets.

The fluidic oscillators used in this study are of the jet interaction type. Some of the mechanisms are described below. For a much more thorough examination of the physical mechanism behind the operation of the jets, please see Gregory and Tomac (2013). Figure 2.10 schematically shows some of the internal interaction of the jet which result in oscillations of the jet, both a schematic of the interaction inside the cavity and the resulting exit flow as visualized by schlieren recorded in still air. The fluidic oscillating jet cavity has two entrances which cause two air jets to interact in an unstable fashion. Figure 2.10a shows the primary exit jet emanating from the exit nominally vertically as the two jets are instantaneously balanced against each other. The exit of the fluidic oscillating cavity acts as a coanda surface. This, combined with the unstable interaction

of the jets inside the faculty, causes the primary exit jet to 'stick' to one side of the exit orifice, as is seen in the vectoring of jet in the sheileren image of Figure 2.10b. As the vortex pair formed by the right hand jet (shown in green in Figure 2.10b) takes up more and more of the cavity (Figure 2.10c), the exit jet is vectored further to the right as shown in Figure 2.10c. This situation is unstable and the next step (not shown) results in the right hand vortex (shown in green) forcing the left hand jet to circulate and the right hand jet to dominate the exit flow causing the same process to occur but with the opposite symmetry. For reference, the exit orifice of the jet is 1.5mm across. The height of the jets defines the height of the overhang within which the array of jets is housed.

The jet array is placed under an overhang with a step of 1.25mm that is designed to redirect the exit flow such that it emanates tangentially to the surface. Seventeen oscillating jets are equidistantly distributed across the model span (60H). Each jet orifice is 1.5 × 1.5 mm on the sides and neighboring jets are spaced 7.5 mm apart. The jet oscillating frequency is a weak function of the fluidic oscillator flow rate and, for a typical flow rates utilized in the current test, the frequency is approximately 10 kHz, as measured by a hotwire anemometer. The jet operation is defined by the C_q, which is the ratio between the total mass flow rate through the jet array and the mass flow rate through the test section.

2.5.2 Pulsed Jet Actuators

In the present investigations, pulsed jet actuators are used to provide a clear phase or timing reference relative to the actuation waveform. The pulsed jet actuators are externally triggered and create a corresponding flow response. This is unlike the operation of the fluidic oscillating jets, in which the oscillations of the jets have a random phase relative to each other. Such a phase reference enables measurements of the flow response in reference to transitory actuation, such as its onset and termination. Such control of individual jets also opens a possibility for asynchronous temporal and spatial actuation and, therefore, closed-loop, active control.

The pulsed jets in the present work are integrated into the surface geometry in exactly the same manner as the fluidic oscillating jets, and they utilize the same air supply. A schematic indicating the layout of the pulsed jet flow control is shown in Figure 2.12. The air supply is routed to a plenum that is integrated into the flow control insert which distributes air to each fast response valve. The valves selected are Festo MHJ10-S2,5-QS-4-MF. The valves supply air to a channel which allows the flow to exit tangentially to the elliptic surface. Seven pulsed-jet actuators are equidistantly distributed across the model span past the apex. Each jet orifice is 0.75 × 4.86 mm, and neighboring jets are spaced 12 mm apart. The characteristics of these valves are described in conjunction with Chapter 4. These jets are characterized using a hot wire velocity probe. However, due to the compressible nature of the flow at the speeds exiting the jets, the hotwire is calibrated to the multiple of the density and velocity, i.e., relative to the unit mass flow rate (Stainback and Nagabushana1990). As the mass flow rate to the jets is measured at the air supply line, it is possible to generate a calibration curve. This calibration curve is shown in Figure 2.13 and is used for characterization of the jets' 'strength' in the rest of the thesis. The error is estimated to be within the error of the hot wire measurements (±1% of measured values).

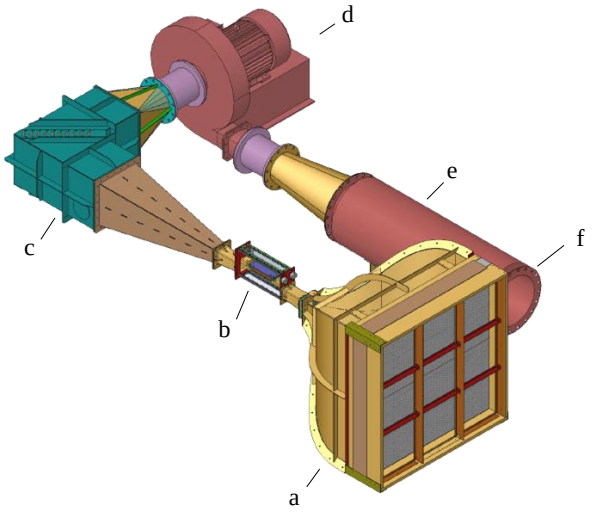

Figure 2.1*Wind tunnel schematic, the air is drawn into the contraction (a), the test section (b) and an expansion (c) before entering the fan (d) after which the air is driven through a muffler section (e) before exiting the facility through a heat exchanger (f).*

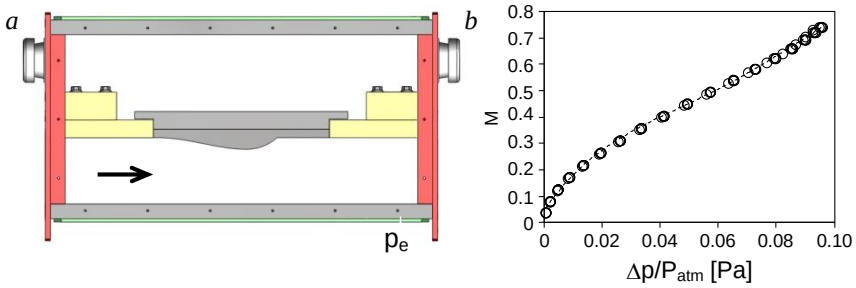

Figure 2.2*Test section schematics (a) and calibration (b).*

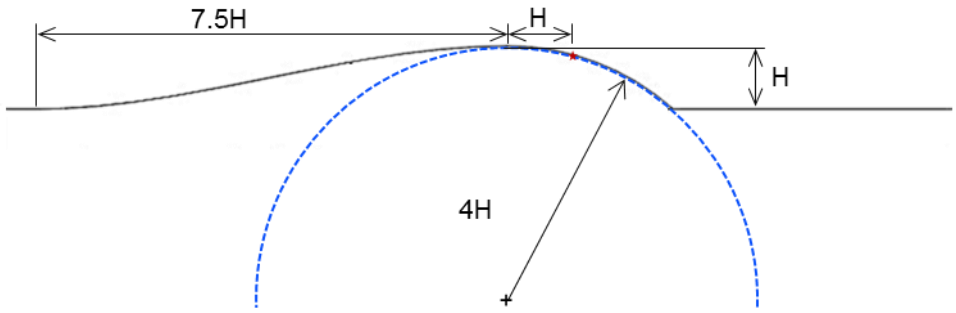

Figure 2.3 *The convex flow geometry.*

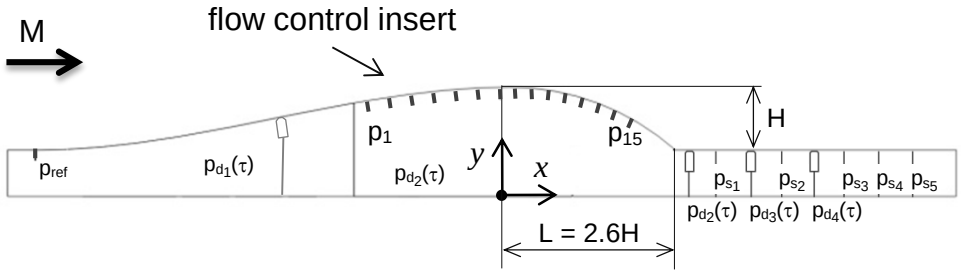

Figure 2.4 *Schematics of the flow diagnostics used for the time-resolved characterization.*

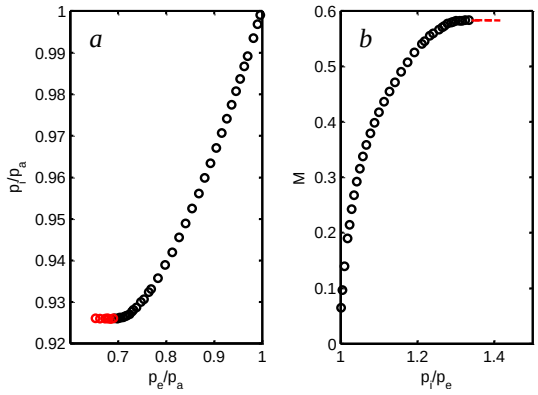

Figure 2.5 *Characterization of the tunnel flow over the test ramp geometry: pressure pi downstream from the inlet contraction with p_e at the test section end (a) and tunnel Mach number with the p_i/p_e (b).*

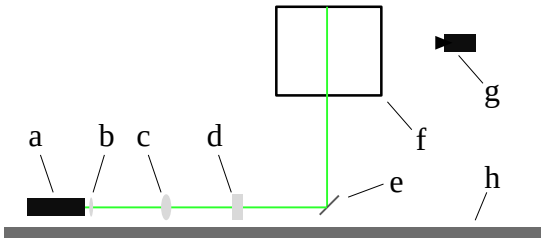

Figure 2.6 *A schematic showing the components of the PIV system the laser (a) generates a beam of light (shown in green), which passes through two spherical lenses (b) and (c) before passing through a cylindrical lens (d) after which the sheet that is formed is sent to the test section (f) where the flow can be visualized using the camera (g), the entire PIV system rests on an optical table (h)*

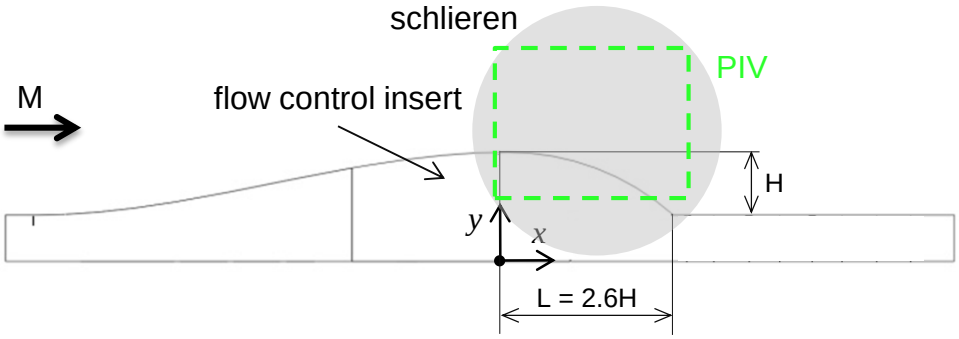

Figure 2.7 *A schematic showing the locations of the Schlieren and PIV measuring domains*

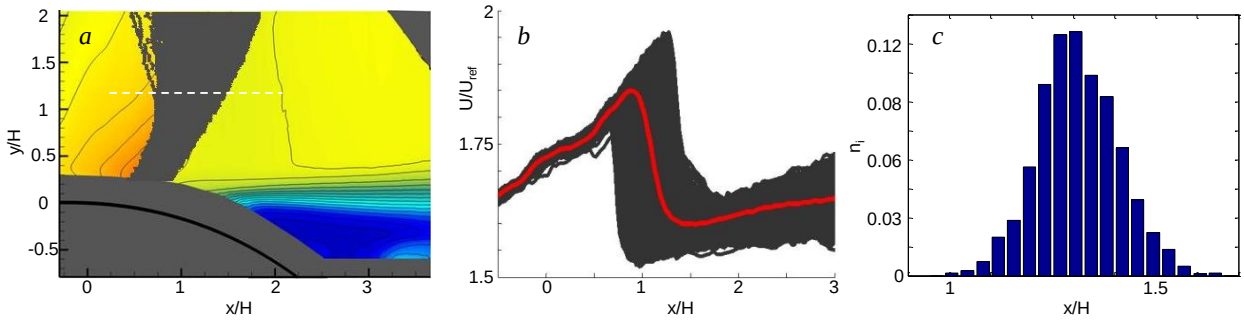

Figure 2.8*Overlapped discretized shock positions for the baseline flow at p_i/p_e = 1.36 (a), the corresponding streamwise velocity profiles across the shock (b) at the marked elevation, and histogram of the shock streamwise positions x/H (c).*

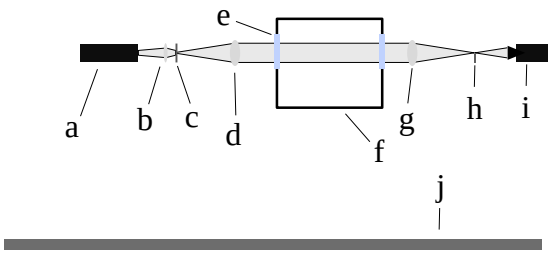

Figure 2.9 *A schematic showing the components of the Schlerien system, light is generated (a) where it passes through a collecting lens (b) and then through a pinhole (c), next the light passes through the first main lens (d) after which the collimated light is admitted to the test section through a glass window (e), whereby the light interacts with the flow traveling through the test section (f), after which it passes through a second main lens (g), a cut off edge (h) and is finally captured by the camera (i). The entire assembly is supported by an optical rail (not shown) and supported on an optical table (j)*

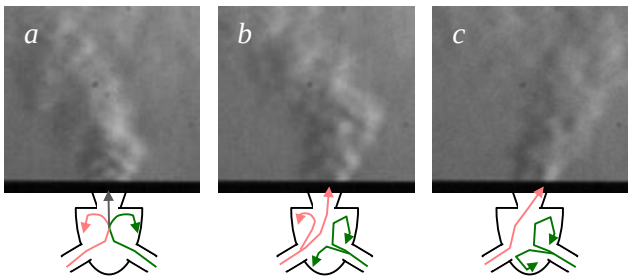

Figure 2.10 *Schematic of the fluidic oscillating jet operation showing schematically the unstable interaction between the two inlet ports that lead to an oscillation of the exit port and the schlieren visualization of the exit.*

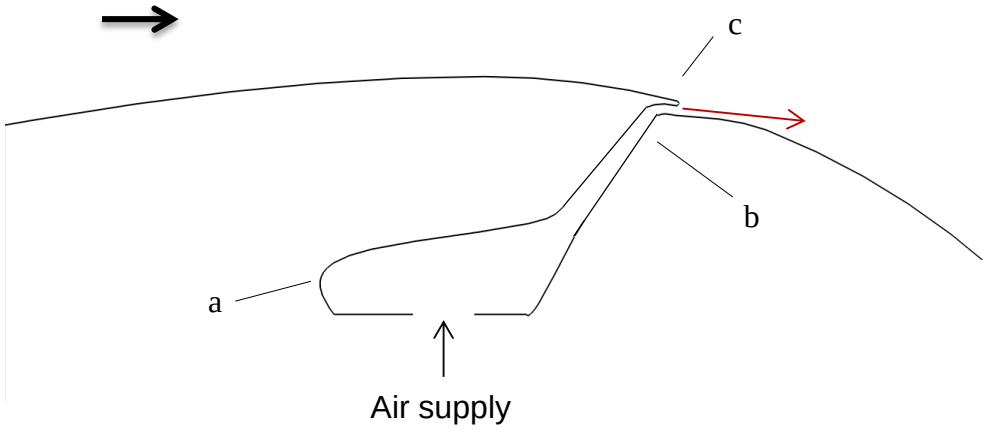

Figure 2.11*Schematics of the fluidic oscillator flow control, indicating the location of the air plenum (a), oscillator array location (b) and exit overhang (c)*

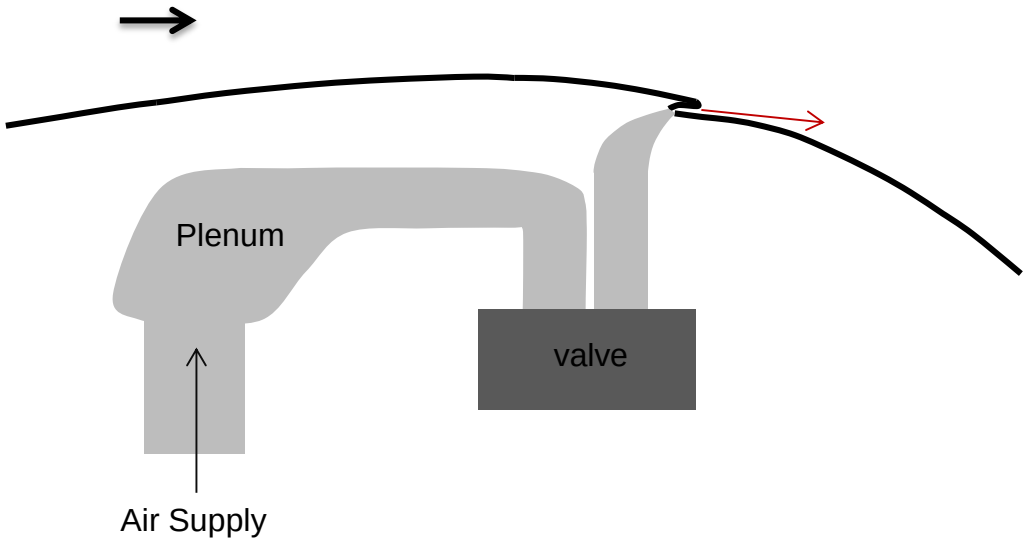

Figure 2.12 *Schematics of the pulse jet flow control, indicating the location of the air supply, plenum and control valve.*

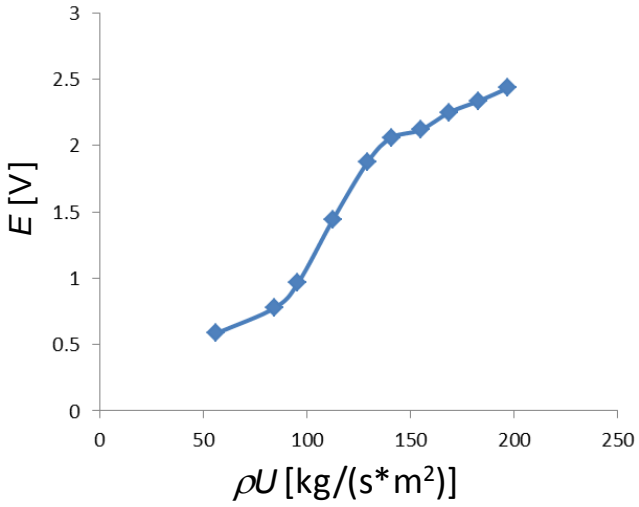

Figure 2.13 *The hotwire calibration curve.*

CHAPTER 3

CHARACTERIZATION OF THE BASE FLOW

The base flow over the curved surface insert within the test section (cf. Chapter 2) is characterized in detail in the absence of flow actuation with specific attention to the structure and position of the formed shock. To begin with, the dependence of the static pressures at the inlet and outlet of the test section (p_i and p_e, respectively, cf. Figure 2.1) over a full range of the tunnel speeds (p_i/p_e = 1.1 to 1.45) is shown in Figure 3.1. As the tunnel speed increases, both p_i and p_e decrease monotonically, until p_i begins to level, which indicates test section choking. Since the mass flow rate through the test section becomes invariant when the flow is choked, further increase in suction that is effected by the system's blower (downstream) results only in further lowering of the back pressure, illustrated by continued decrease in p_e while p_i is invariant (marked in red in Figure 3.1a). The flow at the test section can be characterized using the upstream Mach number and the downstream pressures p_e as reference parameters when the flow is pre-choked and choked flow, respectively, or alternatively, the flow can be characterized using the pressure ratio p_i/p_e throughout. Figure 3.1b shows a variation of the test section Mach number with the pressure ratio p_i/p_e until the flow becomes choked as shown by the red dashed horizontal line.

The characteristics of the base flow separation over the curved surface (that includes the integrated flow control actuators) at increasing pressure ratios are illustrated in a series of schlieren images as shown in Figures 3.2a-e. Prior to formation of a shock past the apex of the ramp, the only sharp density gradients exhibited in the flow field are generated by the incipient separating shear layer as a result of the adverse pressure gradient, as seen in Figure 3.2a(M = 0.54, p_i/p_e = 1.22). As shown in Figure 3.2a, the separation is locked to the orifice of the inactive actuation jets (cf. Chapter 2) and formation of the shear layer is

accompanied by shedding of large-scale vorticity concentrations. The adverse pressure gradient upstream of separation is also marked by significant density gradients. As the Mach number (or pressure ratio) is increased, a highly unsteady vertical shock is observed at about $M = 0.57$ ($p_i/p_e = 1.26$, Figure 3.2b), and although not clearly visible here, leads to an upstream migration of the separation. The shock becomes stronger and its streamwise oscillations diminish somewhat (although it is still highly unsteady) as the Mach number increases (Figures 3.2c-e, $p_i/p_e = 1.30, 1.35, 1.39$). The shock also tilts downstream (and extends away from the surface) as the Mach number increases, as a result of its downstream migration and the changes in the curvature of the surface and in the direction of the local flow. Eventually, the shock extends to the opposite wall of the test section and the flow in the test section becomes choked. As noted above, the formation of the shock shifts the flow separation upstream (compare Figures 3.2c and a), and the shock-induced separation migrates downstream with the shock.

Some features of the attachment of the separated base flow to the flat surface downstream of the ramp insert are inferred from surface oil visualization within the domain $1 < x/H < 7$ (Figure 3.3) for four pressure ratios $p_i/p_e = 1.17$ (subsonic), 1.3 and 1.35 (pre-choked), and 1.4 (choked). Oil is applied to the surface downstream of the ramp at $x/H > 2.6$. The nominally two-dimensional flow geometry leads to a symmetric streakline pattern downstream of the ramp indicating symmetry about the center plane, but with a strong effect of the side walls on each side of the test section. Of particular note is the oil streakline pattern that corresponds to flow attachment. As with any surface oil flow visualization the flow attachment is indicated by high concentrations of the visualization paint, with the streaks of paint indicating the direction of the shear stress along the surface. The attachment region is indicated by the dashed line which indicates that this region moves downstream (3.3a-c) and is in the same location for $p_i/p_e = 1.35$ and 1.4 (3.3c and d). When the flow is subsonic, the attachment (Figure 3.3a) appears two-dimensional along a narrow region along the centerline of the duct. At the edges, the

corner flows generated by the interface between the wall and the surface of the model cause rotational flows which is seen in the swirling patterns along the curved surface at the spanwise extents of the wind tunnel model (the present investigation has not attempted to mitigate the effects of corner flow since their effect on the flow in the center segment of the span was judged to be minimal). However, as the Mach number increases, the reattachment region assumes a horseshoe shape, which can be seen in the structure indicated by the intersection of the dashed line and the centerline of the duct for each image respectively (Figures 3.3c, e, and g). This three dimensional separation is affected by corner flows that can be seen in the lower and upper third of the elliptic surface ($x/H < 2.6$), which implies that the flow along the walls does not behave in the same fashion as that along the centerline. These spanwise non-uniformities give rise to three-dimensional separation as is evident by non-spanwise reattachment seen at $x/H > 2.6$ in Figure 3.3. There is a clear downstream extension of the separated domain at transition from the subsonic flow separation due to the adverse pressure gradient (Figure 3.3a), and transonic shock-induced separation (Figure 3.3c). The downstream extent of the separation domain (as indicated by the dashed line) translates further downstream with an increase in pressure ratio (Figure 3.3e), until the flow becomes choked and there are no further significant changes in separation.

The streamwise distributions of the static pressure along the curved surface in the absence and presence of the (inactive) actuator jets are shown in Figures 3.4a and b, respectively over a range of tunnel speeds. Upstream of the apex ($-2 < x/H < 0$) the streamwise variation of the pressure exhibits the typical evolution of a mildly converging duct as the flow accelerates with the contraction. In the absence of the flow control array (3.4a) there is a much clearer upstream shift in separation point as the shock induces separation ($p_i/p_e > 1.25$), which is predominantly due to the higher concentration of static pressure taps near the point of separation. Flow separation downstream of the apex varies with the tunnel pressure ratio. In the absence of the jet orifices (Figures 3.4a),

when the flow is subsonic ($p_i/p_e < 1.27$) separation occurs at $x/H \approx 1.5$. The initial formation of a shock ($p_i/p_e = 1.27$) shifts separation upstream but it does not appear to be immediately downstream of the shock, while for $p_i/p_e \geq 1.29$ the separation is clearly induced by and locked to the shock. As result, the separation migrates downstream with increasing pressure ratio due to the streamwise translation of the shock with increasing pressure ratio (as marked by the dashed line in Figure 3.4). The presence of the actuators locks the separation at low speeds prior to the appearance of a shock (at $x/H = 1, p_i/p_e < 1.25$, Figure 3.4). As shown in Figure 3.2c, the appearance of the shock leads to separation that migrates downstream as the tunnel speed increases. The pressure distributions also indicate that the flow becomes choked as the Mach number increases, as is evidenced by the collapse of the pressure distributions onto a single same curve for $p_i/p_e > 1.29$.

Streamwise distributions of the static pressure are also measured along the flat surface downstream of the curved insert($3.5 < x/H < 6.5$) for $1.17 < p_i/p_e < 1.42$ in increments of $\Delta(p_i/p_e) = 0.024$, as shown in Figure 3.5 (in the absence of the actuation jets). These data show that as a result of flow divergence within the duct (the flow cross section increases past $x/H > 0$), there is a streamwise increase in the static pressure along the duct over all pressure ratios. As expected, as the pressure ratio across the duct increases, the static pressure (for a given p_i/p_e) decreases (i.e., becomes more negative). It is noteworthy that at low speed ($1.17 < p_i/p_e < 1.23$), the flow appears to form a closed bubble along the centerline, downstream of the ramp ($2.5 < x/H < 4.5$) thereby leading to a local favorable streamwise pressure gradient that is followed by an expansion at the downstream end of the measurement domain.

The formation of a shock within the test section is characterized using planar high-speed PIV measurements (cf. Chapter 2). In addition to measurements of the flow over the curved surface, the PIV data are used to extract the instantaneous shock position. As noted in Chapter 2, due to reflections on the surface of the test section, the flow

immediately next to the surface couldn't be resolved in the present setup, and therefore the present measured flow fields exclude the near-wall region (along a region of approximately 0.3H).

Samples of the time-averaged flow field (using color raster plots of the streamwise velocity component *U*) showing subsonic separation (induced by the adverse pressure gradient over the curved surface) and shock-induced separation are included in Figures 3.6a and b, respectively. It should be noted that the grey area in all PIV images presented (e.g. Figure 3.6) indicates area over which data was unable to be computed due to surface reflections (the surface is illustrated by the dark black line). These data are acquired at pressure ratios p_i/p_e that are below (Figure 3.6a) and above (Figure 3.6b) the critical pressure ratio for the shock formation. Prior to shock formation (Figure 3.6a), the flow accelerates up to the ramp apex ($x/H < 0$) and then decelerates ($x/H > 0$) as the boundary later thickens and the flow ultimately separates at $x/H = 1.75$. Following separation, the ensuing shear layer spreads in the cross stream direction towards the bottom flat surface, ostensibly as a result of strong entrainment from the separated flow domain. However, when the critical Mach number is reached at the apex, the flow continues to accelerate and terminates in a transonic normal shock as shown in Figure 3.6b. The underlying shock-boundary layer interaction induces discontinuous boundary layer thickening which, combined with the adverse pressure gradient, induces premature flow separation at $x/H = 1.25$. Compared to the subsonic separation, the shock-induced separation results in a significant increase in the cross stream extent of the separated flow domain and increased cross-stream spreading of the shear layer.

Using the velocity at the apex ($x/H = 1$) at a height of ($y/H = 1$), (≈ 350m/s for the choked flow), and the cross stream extent of the duct at the apex of the contraction, the Reynolds number is $Re \approx 2.5 \times 10^6$. The high Reynolds number and the fact that the flow is most likely tripped due to a small (< 0.25 mm) step at the transition segment between the inlet

(Figure 2.1a) and the test section (Figure 2.1b), indicate that the flow is turbulent as it approaches the apex of the contraction.

The cross stream shock position and structure are extracted from instantaneous streamwise distributions of the streamwise velocity component at each cross stream elevation y/H. Such a distribution (normalized by U_{ref} which is the speed at the inlet of the test section computed from M in Figure 3.1b) is shown in Figure 3.7b along with the time-averaged distribution (in red). In the presence of a shock, there is a distinct velocity jump across the shock. The shock position at each elevation y/H at a specific instant in time is defined by finding the minimum slope within the velocity jump. As part of the present investigations, a procedure was developed for extracting the most probable shock structure for a given cross flow, as illustrated in Figure 3.7. Figure 3.7a shows the time averaged flow field (cf. Figure 3.7) and is superposed with traces that mark the instantaneous shock positions (that are extracted as explained below) for each of the realization that are used in the time-average and illustrates the extent of the shock fluctuations. As noted in connection with extracting the position of the time-averaged shock in Figure 3.7b, the shock position is extracted from the slope of the velocity jump of the instantaneous streamwise distributions of the streamwise velocity component at each cross stream elevations y/H. Shock positions associated with the velocity traces in Figure 3.7b are shown in the form of a histogram in Figure 3.7c, where $n_i = N_i/\sum N_i$ for each spatial bin $\Delta x/H$. This process is repeated for each realization for all y/H. The resulting traces that mark the shock position for each realization are displayed on top of a time-averaged raster plot in Figure 3.7a, and illustrates the shock motion (or fluctuations) for the given pressure ratio. The histogram can enable the selection of a subset of a shock population that is the 'most probable' based on the selection criterion.

Cross stream profiles of shock structures that are extracted from the PIV measurements over a range of the pressure ratios p_i/p_e are shown in Figure 3.8a and corresponding cross stream distributions of shock strength are shown in Figure 3.8b in terms of the ratio of the

velocity just upstream (U_u) and just downstream (U_d) of the shock. The same data for the case where the flow control is present but inactive is shown in 3.8c and d. With the actuators present (Figure 3.8c) the shock root ($y/H < 0.5$) appears to persist further upstream compared to the case without the actuators present (Figure 3.8a), which is due to the shock forming at the discontinuity generated by the installation of the flow control. The shock strength is comparable and very similar for both cases; compare Figure 3.8b and d. These data demonstrate that the shock root displacement is minimal ($\Delta(x/H) = 0$ for $1.32 < p_i/p_e < 1.27$, $y/H < 0.6$) while the flow is not choked, which is the case both with and without the flow control present. The primary effect on the shock is the slight increase in tilt with p_i/p_e. However, once the flow is choked ($1.29 < p_i/p_e$), the streamwise shock displacement increases with p_i/p_e and is accompanied with progressive streamwise tilt. As shown in Figure 3.8b and d, the strength of the shock decreases with cross stream elevation from the surface. The shock intensifies as p_i/p_e increases and as it is displaced and tilts downstream. Further increase in p_i/p_e beyond 1.29 shows that as the shock begins to transition into an oblique shock, its strength near the root begins to diminish (as shown at $y/H < 0.5$), while it significantly increases away from the surface, rendering the shock strength more uniform in the y direction. For $p_i/p_e > 1.34$ there is clear streamwise weakening of the shock while the gradient of shock strength becomes less pronounced away from the surface (e.g., $y/H > 0.6$). At the highest pressure ratio $p_i/p_e = 1.39$, the flow is choked and the shock exhibits a clear weakening (compared to $p_i/p_e = 1.34$) as it is translated in the streamwise direction with further increase in tilt as is evidenced at $y/H > 0.6$ in Figure 3.8b and d. This increase in shock strength results in an expected increase in wave drag that would be measured in external aerodynamics applications (Babinsky and Harvey, 2011).

The Mach numbers upstream and downstream of the shock are computed by extracting the corresponding velocities (denoted with subscripts"1" and "2", respectively) are determined by finding the maximum and minimum velocity on either side of the rapid

change in the streamwise distribution of the velocity (cf. Figure 3.7b). These velocities, along with the local shock slope, are used to compute the normal (V_n) and tangential (V_t) velocity component relative to the shock. The upstream and downstream Mach numbers are computed using the expression the modified speed of sound

$$a_1 = \sqrt{\frac{\gamma+1}{2}\left(V_{n1}V_{n2} + \frac{\gamma-1}{\gamma+1}\left({V_t}^2 - {V_1}^2\right)\right)},$$

(John and Keith 2006) . This equation is used to generate the profiles shown in Figure 3.9. The profiles are color coded by pressure ratio across the test section and the curves at sub-sonic values are downstream from the shock. The upstream Mach number increases with the pressure ratio, (at y/H = 1.6, M = 1.05 for p_i/p_e = 1.29, and M = 1.117 for p_i/p_e = 1.39. At p_i/p_e = 1.36 and 1.39 the downstream Mach number exceeds unity for y/H < 0.32). This region of supersonic flow downstream from the shock near the wall is often referred to as a supersonic 'tongue'. These Mach numbers indicate that disturbances propagate upstream either around the shock (at pressure ratios, p_i/p_e < 1.32, where the facility is not choked) or through the boundary layer where the flow is subsonic in a thin layer near the wall.

Additional insight into the shock dynamics is sought through a measure of its oscillation about its most probable position and the correlation of its displacement with the static pressure in the separated flow domain. The evolution of the shock is illustrated in Figure 3.10 in terms of the cross stream distributions of the standard deviation of its streamwise oscillations (Figure 3.10a), and of the correlation between the surface pressure signal $p_{d2}(\tau)$ and the instantaneous shock position $x(\tau)$ (Figure 3.10b). The profiles of both standard deviation and cross correlation are similar both with and without the flow control installed, therefore the case where the flow control is present but inactive is shown in Figure 3.8. The distributions at the lowest tunnel speed (p_i/p_e = 1.27) apparently differ significantly from the rest (cf. the distributions in Figure 3.8). The

reason for this difference is that at this pressure ratio the separation is not induced by the shock. The data in Figure 3.10a show that the magnitude of shock oscillations increases with cross stream elevation for all flow speeds. Only for the shock that forms at $p_i/p = 1.27$ is the variation of the oscillation magnitude with height stronger compared to the other cases. The correlation of the measured surface pressure $p_{d2}(\tau)$ and the shock position $x(\tau)$ (Figure 3.9b) clearly indicates strong dependence of an increase in either. Another notable feature is that the correlation has a sharp (nearly discontinuous) increase in magnitude as the pressure ratio increases. There is a rather weak correlation at the lowest pressure ratio at which the separation is not induced by the shock (i.e. subsonic separation), and once the shock induces the separation, there is a significant increase in the correlation between the measured pressure and shock position. Finally, once the flow is choked, the magnitude of the correlation level increases even further to levels that are in excess of 0.8.

As it is illustrated in Figure 3.7, the ensemble average of the captured PIV flow field for a given flow condition may not fully represent the shock position, strength and structure. In order to sharpen the shock-related features of the flow fields, the full ensemble of the PIV data sets is further conditionally averaged over the spatial bins $\Delta x/H$ (cf. Figure 3.7c). After the most probable shock position is deducted from the histogram (see Figure 3.7c) at the peak occurrence, all the flow fields that contain the shock within the most probable spatial bin are subsequently averaged. In order to generate the flow fields, the flow field is examined at $y/H = 1$ and the resulting histogram dictates which flow fields are averaged. The resulting conditionally-averaged flow fields for different pressure ratios p_i/p_e are shown in Figure 3.11 in terms of the contour plots of the streamwise velocity component. It should be noted that conditionally averaging based on the shock motion (upstream or downstream) within the bin resulted in indistinguishable flow fields, which could be a consequence of a narrow spatial bin $\Delta x/H$. Comparison between the ensemble- and conditionally-averaged flow fields, such as Figure 3.6b and Figure 3.11c,

shows that the 'most probable' conditionally-averaged shock position coincides with the averaged shock position, while the former resolves sharper velocity gradients associated with the shock and hence better isolates the shock. Nonetheless, all the major flow features are adequately captured even in the ensemble-averaged flow fields. As the pressure ratio increases (Figure 3.11a-f) the shock translates downstream and tilts in the streamwise direction (as shown in Figure 3.7). Commensurate with Figure 3.4, the separation point can be seen to first move upstream (Figure 3.11a-c), and then move downstream for further increases in pressure ratio as the shock translates downstream (Figure 3.11c-f).

Further illustration of the flow in the presence of the shock are shown in Figures 3.12a and b using 'waterfall' plots of the conditionally-averaged streamwise velocity component extracted from the PIV data for $p_i/p_e = 1.27$ and 1.39, corresponding to the pre-choked and choked flow regimes, respectively. A strong velocity gradient (characterized in Figure 3.7) is evident near the root of the normal shock in Figure 3.12a, which diminishes away from the surface, indicating the (time-averaged) shock weakens significantly with cross flow distance from the surface. However, when the flow is choked, the shock extends in the cross stream direction and is tilted in the streamwise direction with reasonably uniform cross stream strength, as is evident from the velocity gradient across the shock (Figure 3.12b). The flow fields are also shown with the actuators installed but inactive in Figure 3.12c and d, which are nearly indistinguishable from the corresponding plots with the actuator not present for the same pressure ratio.

The measurements of the base flow emphasize that since the flow downstream of the transonic shock is subsonic, pressure disturbances can propagate upstream and induce temporal imbalance of the pressure field across the shock. It is also reasonable to expect that upstream pressure fluctuations that are carried through the upstream boundary layer can result in disturbances downstream from the shock and affect the formation and evolution of the separating shear layer and flow attachment downstream of the shock.

Given the relation between the time-averaged pressure measured by p_{d2} downstream of the curved insert and the time average shock displacement (Figure 3.8), it is expected that there is a strong correlation between the instantaneous pressure $p_d(\tau)$ and the instantaneous shock position $x(\tau)$. Figure 3.13a and b show simultaneous time traces of the shock position and pressure. These traces indicate a clear correlation between the two time traces, which are emphasized using dashed lines at several large excursions. Furthermore, each positive excursion in the pressure is associated with positive excursion in the shock location, and vice versa. To quantify the corresponding flow fields at these particular instances, three instantaneous velocity fields are shown at times that correspond to the large excursions in pressure from the high level at A to the low level at C, passing through the average level at B, as marked in Figure 3.13b. The corresponding contour plots of the streamwise velocity component are shown in Figures 3.13c–e, respectively (PIV measurements at $p_i/p_e = 1.34$). The captured flow fields demonstrate that the shock not only moves downstream along with a decrease in the pressure (from A to C), but it also changes its shape by continuously increasing its streamwise tilt with the streamwise displacement. Similarly, the shock decreases its tilt with the upstream motion (not shown). Although instantaneous flow fields are not necessarily sufficient for determination of the flow separation point with the captured shock displacement, the velocity fields shown suggest that the flow separation point dynamically shifts along with the shock displacement. Further evidence of the synchronous displacement of the shock and the flow separation is seen in the shear layer velocity as shown in Figure 3.13f for $x/H = 2.5$. These profiles indicate a downstream shift in the shear layer profile that is directly proportional to the corresponding shock position x, which is another evidence of the shift in flow separation with x, i.e., the coupling between the shock position and incipient flow separation.

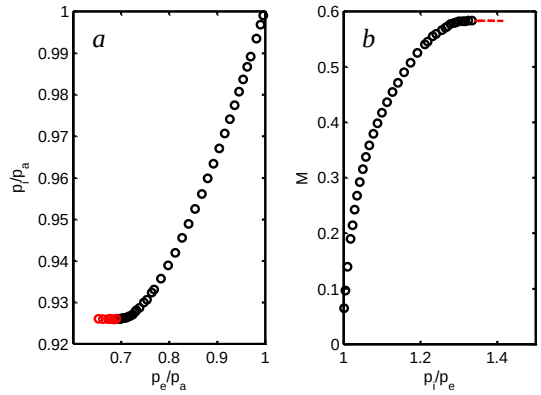

Figure 3.1 *Characterization of the tunnel flow over the test ramp geometry: pressure pi downstream from the inlet contraction with p_e at the test section end (a) and tunnel Mach number with the p_i/p_e (b).*

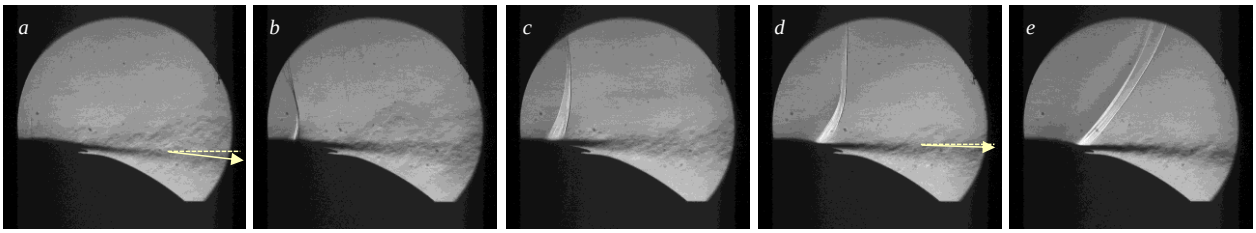

Figure 3.2 *Schlieren visualization of the baseline flow separation for p_i/p_e = 1.22 (a), 1.26 (b), 1.30 (c), 1.35 (d), and 1.39 (e).*

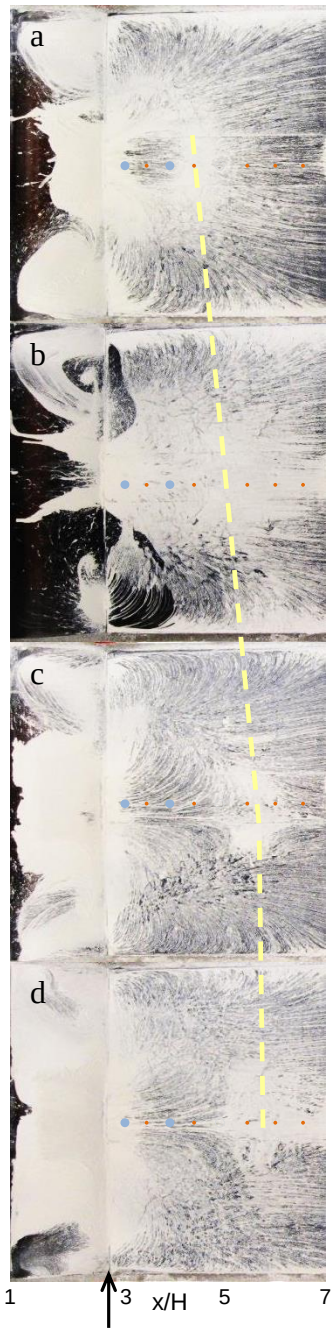

Figure 3.3 *Surface oil-flow visualization within the domain 1<x/H<7 across the entire span of the test section the base flow at p_i/p_e = 1.17 (a), 1.3 (b), 1.35 (c), and 1.4 (d). The spanwise positions of the actuation jets are marked by arrows on the left of each image. The arrow at the bottom of the figure indicates the end of the elliptic surface and the beginning of the planar section. The yellow dashed line indicates the approximate location of the reattachment region.*

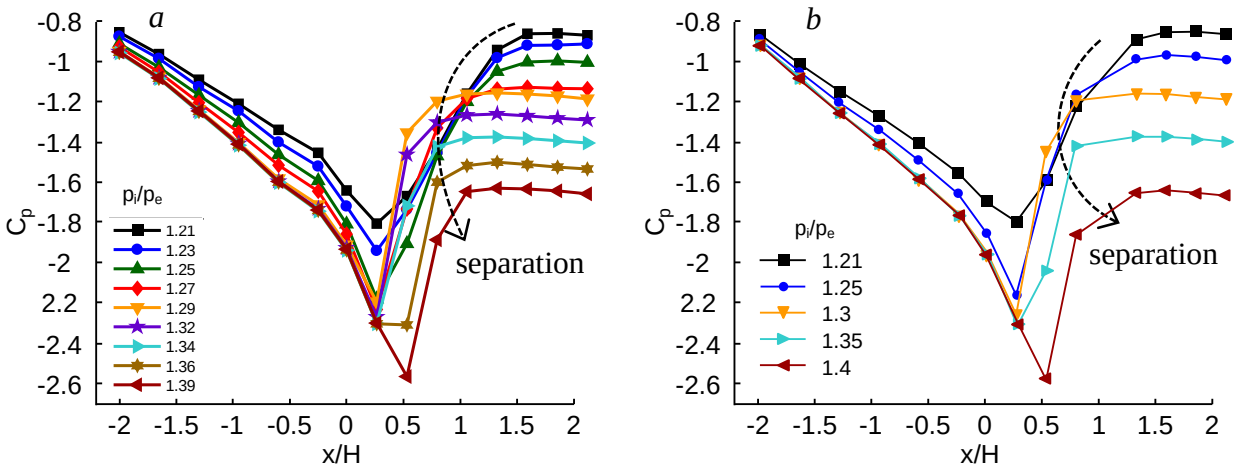

Figure 3.4 *Surface static pressure profiles with increasing p_i/p_e, for the base case and with the flow control present but inactive.*

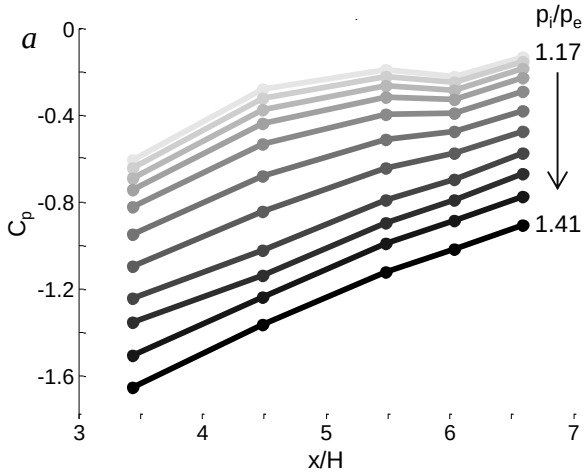

Figure 3.5 *Static pressure profiles for the baseline (a) and the flow upon full actuation (b) for a range of the pressure ratios p_i/p_e = 1.17 – 1.42.*

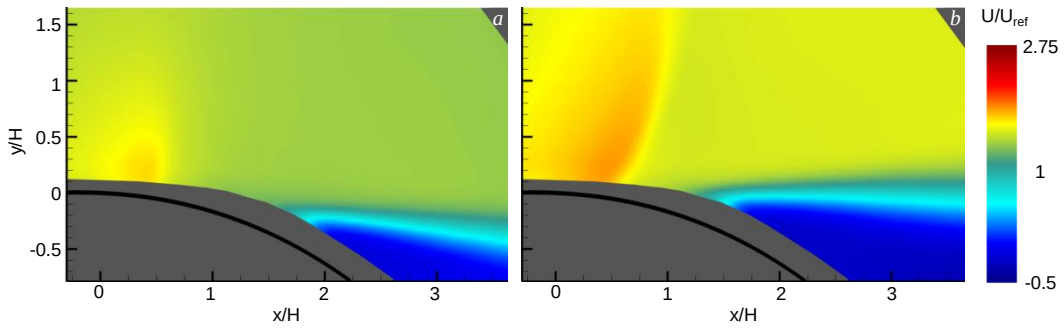

Figure 3.6 *Raster plot of the time average streamwise velocity component for the baseline flow subsonic (a, p_i/p_e = 1.25) and shock-induced (b, p_i/p_e = 1.32) separation.*

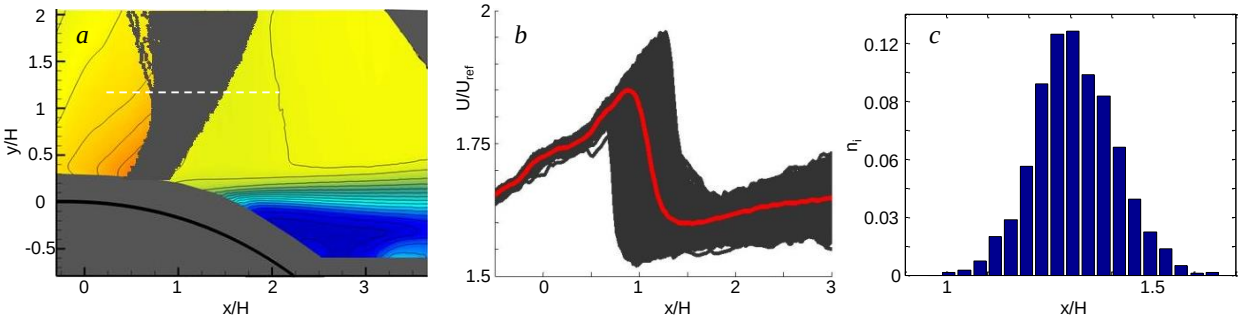

Figure 3.7*Overlapped discretized shock positions for the baseline flow at p_i/p_e = 1.36 (a), the corresponding streamwise velocity profiles across the shock at the marked elevation (b), and histogram of the shock streamwise positions x/H (c).*

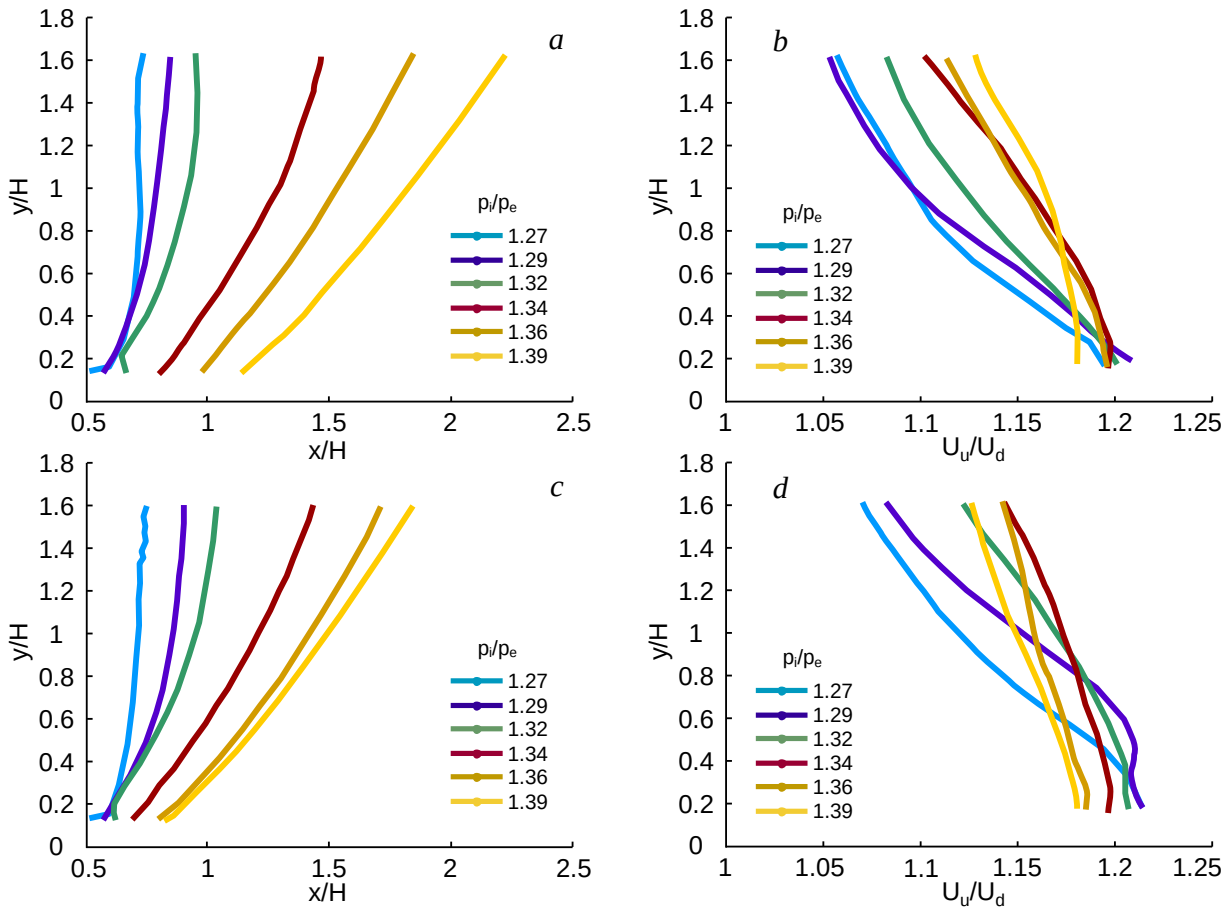

Figure 3.8*The shock evolution in shape and position (a) and 'strength' (b) with p_i/p_e, for the base flow (a and b) and the flow control installed but not active (c and d).*

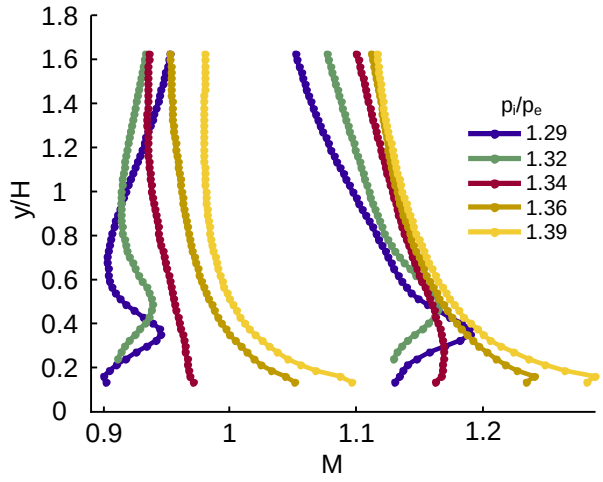

Figure 3.9 *The upstream and downstream Mach numbers across the shock for a range of pressure ratios across the test section.*

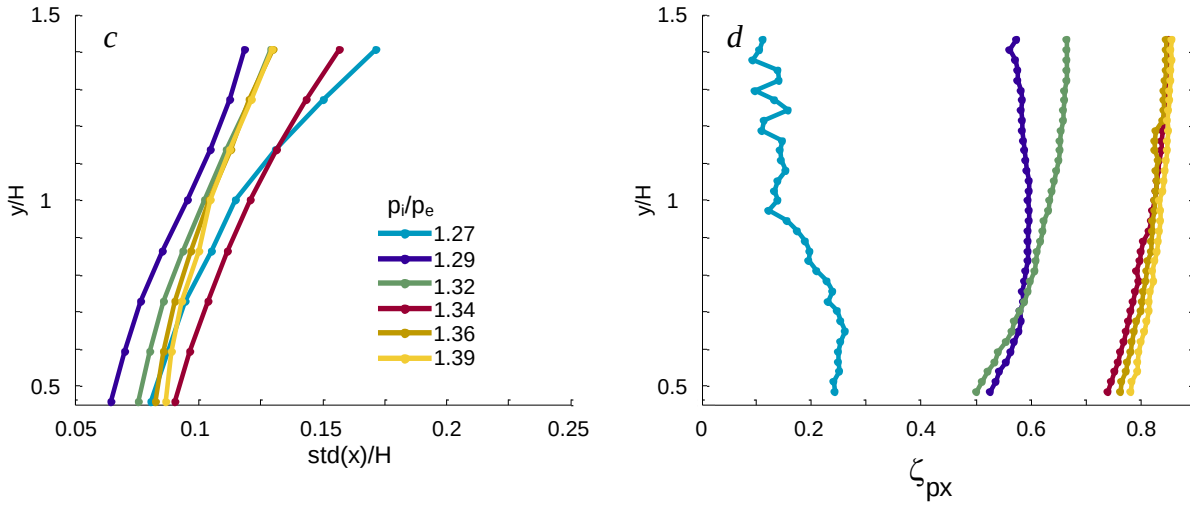

Figure 3.10*Standard deviation of the shock position (a) and cross-correlation between the shock position and the pressure p_{d2} (b) with the elevation y for the uncontrolled flows.*

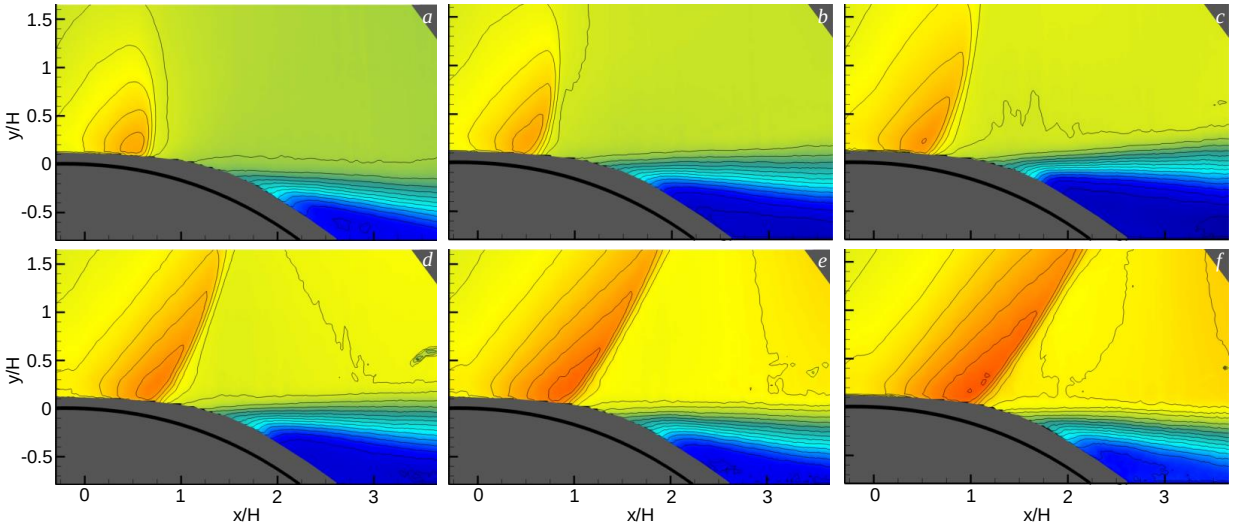

Figure 3.11*Raster plots of the conditionally-averaged time average streamwise velocity component for the most-probable shock location at p_i/p_e = 1.27 (a), 1.29 (b), 1.32 (c), 1.34 (d), 1.36 (e), and 1.39 (f).*

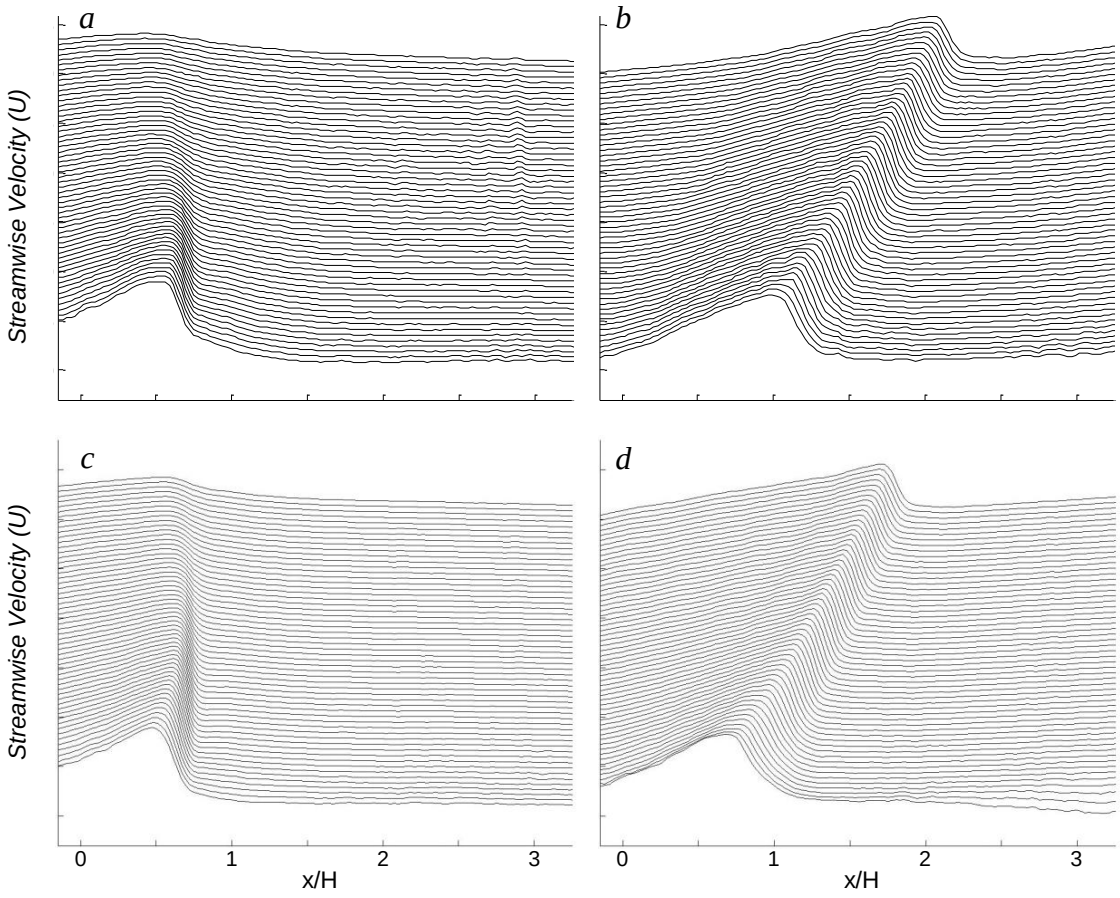

Figure 3.12*Streamwise 'waterfall' velocity profiles for the transonic shock at p_i/p_e = 1.27 (a) and 1.39 (b) without the actuator present and with the actuation present but inactive for p_i/p_e = 1.27 (c) and 1.35 (d).*

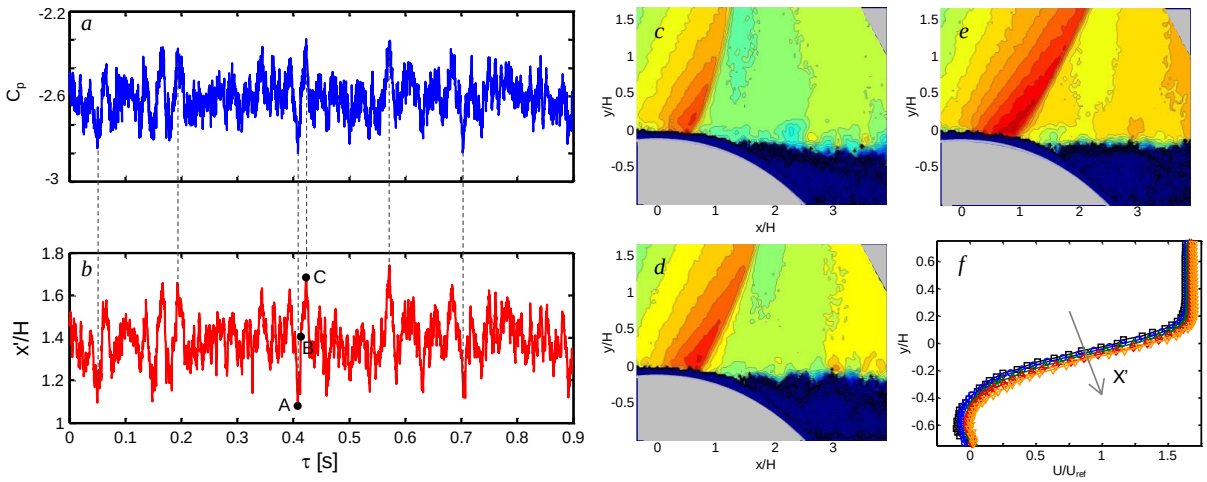

Figure 3.13*Time-traces of the downstream dynamic C_p (a) and the corresponding shock positions x/H (b) for the uncontrolled flow at p_i/p_e = 1.36. Instantaneous flow fields corresponding to times A, B, and C, are shown in (c), (d), and (e), respectively. Shear layer profiles at x/H = 2.5 are shown (f) for conditionally-sampled velocity fields with respect to the shock position.*

CHAPTER 4

INDIRECT CONTROL OF THE SHOCK BY CONTROLLING SHOCK-INDUCED SEPARATION USING FLUIDIC ACTUATION

In the present research, the dynamics of a transonic flow is *indirectly* controlled by manipulation of separation on the diverging segment of the curved test surface. Of specific interest is control of the dynamics shock-induced separation (when a shock is present) that stems from the interaction of the shock with the surface boundary layer. This control approach relies on the reciprocal (subsonic) coupling between the shock, incipient separating shear layer and the inherent unsteadiness of the separated flow. Active flow control is used to modify the separated flow (by inducing partial attachment) and the pressure perturbations that accompany these changes couple to the shock through the subsonic flow, and affect its static and dynamic characteristics. The work described in Chapters 4-6 focuses on investigations of the effects of fluidic actuation using oscillating jets (Chapter 4) and pulsed jets (Chapters 5 and 6) on the base flow and the shock structure and stability.

4.1 Actuation Effects on the Coupling between the Separating Flow and the Shock ($p_i/p_e = 1.34$)

The effects of fluidic actuation on flow separation and thereby on the shock are investigated using a spanwise array of oscillating jets (cf. Chapter 2 section 2.5.1) that are integrated into the curved test surface and issue tangentially at $x/H = 1$. To begin with, the effects of the actuation on the flow field are investigated at an intermediate pressure ratio ($p_i/p_e = 1.34$) for which the flow features are representative of the general trends within the pressure ratio range of the present investigations ($1.25 < p_i/p_e < 1.4$; the effects of the actuation at other pressure ratios is discussed in section 4.2).

The effects of the actuation on the flow are investigated using schlerien visualization (Figure 4.1). The flow features in the absence of actuation (but with the jet array installed) are evident in Figure 4.1a. Unlike the smooth test surface, the image shows the orifice of the actuation jets that issue tangentially to the surface at $x/H = 1$. Similar to the flow features in Figure 3.2c, the appearance of the shock and its interaction with the surface boundary layer locks the separation to the shock itself, as is indicated by the onset of separation at the root of the shock (at $x/H \approx 0.8$). Note that the general features of the separating shear layer are similar to those of the separating shear layer in the absence of the actuators. In the present experiments, the actuators are deliberately placed *downstream* from of separation and effect separation control in the absence and presence of the shock. Activation of the jet actuation ($C_q \cdot 10^3 = 2.3$, Figure 4.1b) is accompanied by several changes in the flow field. First, the actuation jet is visible at the orifice (marked by a white streak, compare Figure 4.1a and 4.1b near the actuator overhang). Both the shock and the location of separation are translated downstream upon actuation (to $x/H \approx 1$, the streamwise translation of the shock is further quantified in Figure 4.8). This image suggests that the actuation leads to significant spreading of the high- and low-speed edges of the shear layer, which indicates enhanced entrainment by the small-scale motions induced by the actuation jets, that are also evident by enhanced mixing, as indicated by reduced density gradients. Furthermore, the low-speed edge of the shear layer appears to become attached to the surface through $x/H \approx 1.1$. When jets are operated at a higher flow rate ($C_q \cdot 10^3 = 4.5$, Figure 4.1c), a lambda shock is formed. The main shock is translated to $x/H \approx 1$ (or nearly the downstream edge of the jet orifice) and the root of the leading leg of the lambda shock is located at $x/H \approx 1.3$. The flow appears to be attached between the upstream and downstream legs of the lambda shock, and furthermore the shear layer is bent towards the surface. It should also be noted that the cross stream spreading of the shear layer is significantly enhanced compared to Figure

4.1b, as is evident by it low and high-speed edges. The schlieren image suggests that the low-speed edge of the shear layer is attached to the curved surface through the downstream edge of the image.

The performance of the actuation at $p_i/p_e = 1.34$ is further assessed from examination of the streamwise distribution of the static pressures over the curved surface (cf. Figure 2.3) as shown in Figure 4.2. As for the base flow, when the actuation is inactive, the pressure decreases monotonically as the flow accelerates within the converging segment of the test section that is formed by the curved flow insert, with a local minimum at the apex followed by pressure recovery (and an adverse pressure gradient). The flow separates at $x/H = 1$ (over the orifice of the actuator array), as indicated by the nominally invariant pressure distribution at $x/H > 1$. In the presence of actuation ($C_q \cdot 10^3 = 4.5$), the pressure distribution for $x/H < 0.25$ is nearly unchanged (the flow at the apex of the contraction is supersonic at this pressure ratio) and the magnitude of the suction continues to increase through $C_p \times 10^3 = 4.5$ at $x/H = 0.25$ as the flow becomes attached and the shock moves downstream (cf. Figure 4.1b and 4.1c). The flow appears to be attached due to the actuation through $x/H \approx 1.5$, where the pressure becomes nominally invariant.

Color raster plots of the streamwise velocity component obtained from PIV measurements at the cross stream center plane ($p_i/p_e = 1.34$) are shown in Figures 4.3a-d for the base flow, and in the presence of actuation at $C_q \cdot 10^3 = 1.7$, 2.8, and 4, respectively. The data shown in Figure 4.3 are ensemble averages of each entire PIV data set (2,700 realizations). It is noted that the same data were also conditionally-averaged using a subset of realizations based on histograms (similar to Figure 2.8c) with negligible changes in shock position and shape.

The data in Figure 4.3 enable assessment of the primary features of the shock and of the flow separation. While the (instantaneous) Schlieren images integrate flow features that are associated with density gradients across the entire width of the test section, the time-averaged PIV flow fields are captured within a single vertical plane and are affected by

the natural unsteadiness of the flow field. As shown in the Schlieren visualization, the shock-induced separation in the base flow (Figure 4.3a) results in a nearly-horizontal shear layer that opens up into a significant domain of the separated flow downstream of the curved insert (as noted in Chapter 3, owing to reflections, the velocity field within a band of nominally 0.3H near the surface cannot be resolved). As actuation is applied, the separation shifts downstream with increasing C_q, and the separated domain diminishes. These data also indicate that the shock strength (as measured by the velocity decrease across it) intensifies with increasing C_q. It is interesting to note that the appearance of the lambda shock at higher actuation flow rate ($C_q \cdot 10^3 = 4$, Figure 4.3, also cf. Figure 4.1c), appears to displace the shear layer away from the surface past the downstream leg of the lambda shock, which causes the apparent 'buckling' in the shear layer ($x/H = 2.2$, $y/H = -0.25$) due to the interaction of the downstream leg of the lambda shock with the separating shear layer, which causes a sudden change in pressure, leading to its deflection away from the surface.

The cross stream shock profile (x/H and y/H) and cross stream distributions of the 'strength' of the shock (based on the velocity ratio U_u/U_d) are shown in Figures 4.4 a and b, respectively. The shock position is computed by finding the maximum slope of the streamwise component of velocity within $0.2 < y/H < 1.7$ for each of the 2,700 instantaneous PIV images. The shock position points are averaged over all realizations to form the time-averaged shock position. As shown in Figures 4.1 and 4.3, the shock translates in the streamwise direction with increasing actuation level as measured by C_q. Concomitantly, the shock becomes tilted in the streamwise direction as indicated by the increased slope of the cross stream profiles (compare, for example, Figures 4.1a $C_q \cdot 10^3 = 0$ and 4), where the shock is beginning to transition to more of an oblique shock. It is noted that at $C_q \cdot 10^3 = 0.6$ the shock moves relatively little (0.1x/H), and the largest motion with increase in C_q occurs for $1.7 < C_q \cdot 10^3 < 2.8$. The change in both shock position and slope are associated with changes in the strength of the shock (Figure

4.4b),as measured by the magnitude of the ratio of the streamwise component of velocity upstream and downstream of the shock U_u and U_d, respectively, that are computed using a streamwise trace at each elevation. The U_u and U_d, are the velocities, and the ratio indicates the strength of the shock. In the absence of actuation, the shock is stronger near the surface and its strength decreases with elevation (indicative of a transonic shock). As the C_q is increased, the general cross stream variation of shock strength is nominally preserved but with a larger increase for $0.4 < y/H < 0.8$ and smaller increase near the surface $y/H < 0.3$. As shown in Figure 4.4a, the largest changes are measured for $1.7 < C_q \cdot 10^3 < 2.8$, with an increase of almost of almost 10% across the entire elevation range of the present measurements. The lambda shock that forms at the highest C_q ($4 \cdot 10^{-3}$) (cf. Figure 4.1c) results in a decrease in the strength of the leading leg of the shock, as indicated by the decrease in shock strength for $y/H < 0.6$. This decrease in strength indicates that the leading leg of the shock is a weak oblique shock and that the velocity downstream from this leading leg is most likely supersonic.

4.2 Dependence on the Tunnel's Pressure Ratio p_i/p_e

This section focuses on the effects of the tunnel pressure ratio p_i/p_e on the effectiveness of the actuation with specific emphasis on the differences between the pre-choked and choked flows. The streamwise variation of the static pressure along the curved surface ($-2 < x/H < 2$, where x is measured relative to the apex of the contraction) is shown in Figure 4.5 for two pressure ratios for which the base flow is pre-choked ($p_i/p_e = 1.32$, Figures 4.5a) and choked ($p_i/p_e = 1.39$, Figures 4.5b). The actuation jets are operated over a range of flow rates $C_q \cdot 10^{-3} = 1.7$, 2.3, 3.4, and 4.5. The pressure distribution in the absence of jet actuation ($C_q = 0$, Figure 4.5a) is also shown for reference. The pressure distributions for both flow regimes exhibit some similar features. As shown in Figure 4.2, as flow accelerates over the converging segment of the curved insert (cf. Figure 2.2), the pressure decreases monotonically. The formation of the shock is

accompanied by a sharp rise in pressure ($0.25 < x/H < 0.8$ for the base flow at $p_i/p_e = 1.32$, Figure 4.5a and $0.5 < x/H < 1$ for the base flow at $p_i/p_e = 1.39$) that is followed by leveling of the pressure at $x/H > 1$ ($C_p = -1.6$ for $p_i/p_e = 1.34$, and $C_p = -1.75$ for $p_i/p_e = 1.39$) due to flow separation. As noted in connection with Figure 4.2, in the presence of actuation, there appears to be virtually no effect on the global flow upstream of the apex, and, as C_q increases, there is a clear *streamwise shift* in the position of the shock (as measured by the sharp pressure rise) and consequently in the location of separation (as measured by the leveling of the static pressure). For $p_i/p_e = 1.32$, the shock and separation position move from $x/H = 0.9$ to 1.5 as the flow rate to the jet increases from $C_q = 0$ to $4.5 \cdot 10^{-3}$. These effects are somewhat diminished for $p_i/p_e = 1.39$, and the shock and separation location move from $x/H = 1.1$ to 1.75 as the jet strength increases from $C_q = 0$ to $4.5 \cdot 10^{-3}$. For both pressure ratios shown in Figure 4.5, the pressure upstream from the shock position in the baseline flow ($x/H = 0.25$ for $p_i/p_e = 1.32$, and $x/H = 0.5$ for $p_i/p_e = 1.39$) is constant as the flow is sonic upstream of the shock.

The effects of the actuation over a range of pressure ratios ($1.25 < p_i/p_e < 1.39$) and three actuation levels ($C_q \cdot 10^{-3} = 0$, 2.3 and 4.5) are investigated using Schlieren visualization (Figure 4.6). The evolution of the flow in the presence of the inactive jet array ($C_q = 0$) changes significantly with increasing pressure ratio as shown in Figures 4.6a, d, g, and j ($p_i/p_e = 1.25$, 1.29, 1.34, and 1.39, respectively). For example, the separation location at $p_i/p_e = 1.25$ is coincident with the actuator overhang at $x/H = 1$, but moves upstream for both $p_i/p_e = 1.29$ and 1.34. However, at $p_i/p_e = 1.39$, the shock translates downstream and both the root of the shock and the separation point are nearly coincident with the orifice of the actuator array. In the presence of actuation, the shock translates downstream for all pressure ratios when $C_q \cdot 10^{-3} = 2.3$ (Figure 4.6b, d, h and k), and the trend continues at the higher C_q ($C_q \cdot 10^{-3} = 4.5$, Figure 4.6c, f, i, and l). The lambda shock appears at the higher actuation levels at higher pressure ratios ($p_i/p_e = 1.34$ and 1.39 for $C_q \cdot 10^{-3} = 4.5$)

where the actuation translates the shock downstream of the jet array (x/H = 1). Although the deflection of the separating shear layer appears to be more apparent at lower pressure ratios (4.6b and c), for all pressure ratios at $C_q \cdot 10^{-3} = 4.5$, (Figure 4.6c, f, i, and l) the separated shear layer exhibits a marked increase in cross stream spreading and mixing compared to the flow in the absence of actuation (Figure 4.6a, d, g and j). The variation of the magnitude of the motion with p_i/p_e and C_q is shown in Figure 4.8b below.

Measurements of the time-dependent static pressure were obtained along the flat surface downstream of the curved insert ($x/H > 2.6$) using high-frequency sensors (p_{d2}, p_{d3}, p_{d4}, cf. Chapter 2). The variations of the time-averaged pressure and its variance with C_q = 0, 0.6, 1.7, 2.8, and $4 \cdot 10^{-3}$ are shown over a range of pressure ratios $1.21 < p_i/p_e < 1.39$ in Figure 4.7. As for the static pressure distributions upstream of the apex (Figure 4.5a and b, $x/H<0$), the actuation does not alter the time-averaged pressure at the upstream transducer p_{d1} (x/H = -2.8, Figure 4.7a), which is invariant with C_q. However, the sensor p_{d2} (x/H = 3.13) shows that downstream of the curved insert the static pressure decreases monotonically with increasing p_i/p_e in the absence and presence of actuation. For a given pressure ratio, there is an decrease in the magnitude of the suction with C_q, which indicates pressure recovery as a result of enhanced attachment to the surface in the diverging section of the duct. The actuation-induced changes in attachment (and pressure increase as marked by reduced suction) relative to the base flow diminish with increasing pressure ratio (for a given C_q). The data in Figure 4.7b show that in the absence of actuation, the variance of the static pressure (and therefore the pressure oscillations that are associated with the separated flow domain) increases with p_i/p_e as the flow speed increases. While this indicates that the fluctuations associated with the separating shear layer are more intense at higher pressure ratios, it does not necessarily indicate that shock stability is worsened since the stronger shocks (at higher pressure ratios) tend to be more stable. In the presence of actuation, the pressure fluctuations downstream of the curved insert increase significantly with the magnitude of the actuation compared to the base

flow (e.g., 0.15 to 0.42 at $p_i/p_e = 1.3$, for $0 < C_q \cdot 10^{-3} < 4$). However, while at low actuation levels ($C_q \cdot 10^{-3} = 0.6$ and 1.7), the pressure fluctuations appear to be nearly invariant with p_i/p_e, they increase with p_i/p_e for $C_q \cdot 10^{-3} = 2.8$ and 4, indicating that at low pressure ratios ($p_i/p_e = 1.22$) the fluctuations in the shear layer are affected similarly for different actuation levels ($C_q \cdot 10^{-3} = 0.6$ to 4).

To quantify the effect of the actuation on the position and cross stream profile of the shock, the averaged shock position is extracted at each elevation from instantaneous PIV images using the procedure discussed in connection with Figure 4.4. Figure 4.8a shows the variation of the shock displacement with C_q for $p_i/p_e = 1.34$. As shown in Figure 4.6, these data demonstrate that the shock is advected downstream with increasing C_q and the streamwise tilt of the shock increases (cf. Figure 4.4). The shock streamwise position x at $y/H = 1$ is selected as a reference for the measure of the streamwise displacement of the shock (as indicated schematically in Figure 4.8a), and the variation of x with pressure ratio is shown in Figure 4.8b for a range of actuation levels. In these experiments, the tunnel's pressure ratio was set in the absence of actuation, and then the magnitude of the actuation was increased while the tunnel's pressure ratio was monitored and recorded. Each of the colored traces in Figure 4.8b shows the variation of shock position x (as measured at $y/H = 1$) with pressure ratio for five settings of the actuation level ($C_q \cdot 10^3 = 0$, 0.6, 1.7, 2.8, and 4). The variation of x with pressure ratio in the absence of actuation is marked by a dashed line (the shock x-position at $y/H = 1$, for $C_q = 0$ is extracted from the data of Figure 4.3b). These data show that as the pressure ratio increases, the shock moves (nearly linearly) from about $x/H = 0.7$ to just above $x/H = 1.4$. Therefore, in the presence of actuation, there is nearly a two-fold increase in shock displacement regardless of the initial set pressure ratio (at $C_q = 0$) for each control case. It is also remarkable that as the set pressure ratio increases, the adjustment in attachment of the separating shear layer and shock position alters the losses in the test section and

leads to a decrease in the set pressure ratio. During each incremental increase in C_q, the blower fan motor (which is used to set the pressure ratio at $C_q = 0$) is kept constant. The dominant trend in the flow dynamics is the movement of the shock with increasing C_q rather than the change in shock position due to the increase in pressure ratio across the test section. The significant motion of the shock that is induced by actuation over a rather narrow range of p_i/p_e, compared to the smaller range of motion that is attained by significantly larger variations in the tunnel's pressure ratio in the absence of actuation, indicates the sensitivity to the actuation and to local changes in boundary conditions (as opposed to the global flow conditions).

The streamwise (x/H) and cross-stream (y/H) variations in shock strength (as measured by the velocity ratio across the shock), with C_q ($C_q \cdot 10^3 = 0$, 0.6, 1.7, 2.8, and 4) are shown in Figures 4.9a-c and d-f at three pressure ratios. At the low pressure ratio ($p_i/p_e = 1.30$, Figure 4.9a and d), the shock strength intensifies significantly with actuation (e.g., at $y/H = 1$, $1.17 < U_u/U_d < 1.4$), and there is a clear local maximum that appears to migrate closer to the surface with increasing C_q, followed by a nearly linear decrease in strength (cf. Figure 4.6). The corresponding streamwise distributions of U_u/U_d show that the shock is nearly normal past the local maximum in its strength. As the pressure ratio is increased ($p_i/p_e = 1.39$, Figures 4.9b and e), the cross stream decrease in shock strength is significantly reduced for $C_q \cdot 10^3 < 1.7$ and the streamwise tilt increases as the shock transitions from a transonic toward an oblique shock (cf. Figure 4.6). However, for higher actuation levels($C_q \cdot 10^3 = 2.8$ and 4), the diminution in cross stream shock strength is still pronounced. When $p_i/p_e = 1.39$, the shock structures for $C_q \cdot 10^3 < 2.8$ are displaced, but are similar (in terms of the cross stream and streamwise projection of their strength distribution), while at $C_q \cdot 10^3 = 4$ the shock strength is affected by the lambda shock (cf. Figure 4.6), as the formation of the lambda shock causes a decrease in the strength of the leading leg of the shock.

4.3 Correlation Between the Actuation and the Pressure Downstream of the Curved Insert

Given the relation between the time-averaged pressure measured by p_{d2} downstream of the curved insert, the time average shock displacement and the magnitude of the actuation as measured by the flow rate coefficient of the control jets (Figure 4.4a and 4.8b), it is expected that there is a strong correlation between the instantaneous pressure $p_d(t)$ and the instantaneous shock position x(t) (cf. Figure 3.12). Further insight into the shock dynamics with and without actuation is gained by analysis of the shock oscillations about its time average position. Figures 4.10a and c show the cross stream distributions of the standard deviation of the shock oscillations about its time average position in the absence of actuation, p_i/p_e = 1.32 and 1.36 respectively, and with actuation at varying C_q. In addition, the corresponding shock oscillations are characterized in the absence of the actuation jet module (i.e., over a smooth surface). Regardless of the pressure ratio, the results indicate that just the presence of the (inactive) actuator jet array significantly reduces the shock oscillations. However, once the actuation is applied there appears to be a difference with respect to the shock oscillation in the pre-choked flow and after the flow is choked. While the controlled flow generally experiences reduced levels of the shock oscillations under any C_q when the flow is pre-choked (Figure 4.10a), there is an increase in the level of the oscillations near the surface at lower C_q and decrease away from the surface; while the trend appears to be reversed at the highest C_q, once the flow becomes choked (Figure 4.10c). Interestingly, the cross-correlations between the pressure signal $p_{d2}(t)$ and the instantaneous shock position x(t) also shows different trends for the pre-choked and choked flows, as shown in Figures 4.10b and d, respectively. The base pre-choked flow shows the lowest correlation (Figure 4.10b), which remains virtually unchanged near the surface in the absence of actuation and at the two lowest C_q. However, the correlation significantly increases with increasing distance from the

surface. As C_q is further increased, there is a corresponding increase in correlation near the surface as well, which results in a more uniform correlation between the pressure fluctuations and the shock oscillation along its height. There is high correlation between the shock oscillations and pressure fluctuations even in the choked base flow (Figure 4.10d), which becomes slightly more pronounced with the inactive actuator array in the surface. Contrary to the pre-choked flow, once the control jets are activated, the correlation decreases with C_q, particularly closer to the surface.

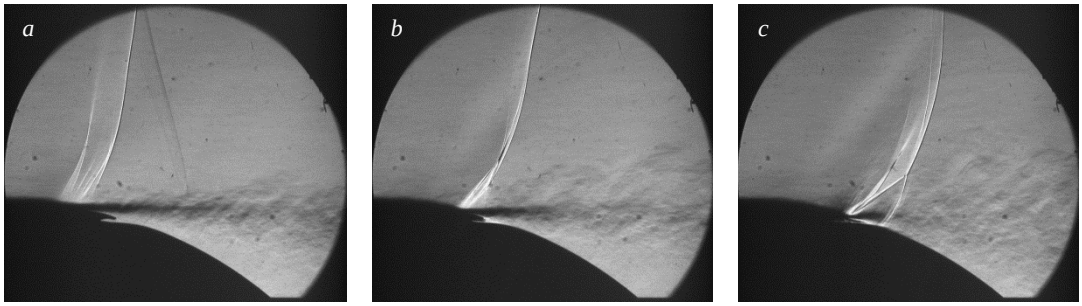

Figure 4.1 *Schlieren visualization at p_i/p_e = 1.34 and $C_q \cdot 10^3$ = 0 (a), 2.3 (b) and 4.5 (c).*

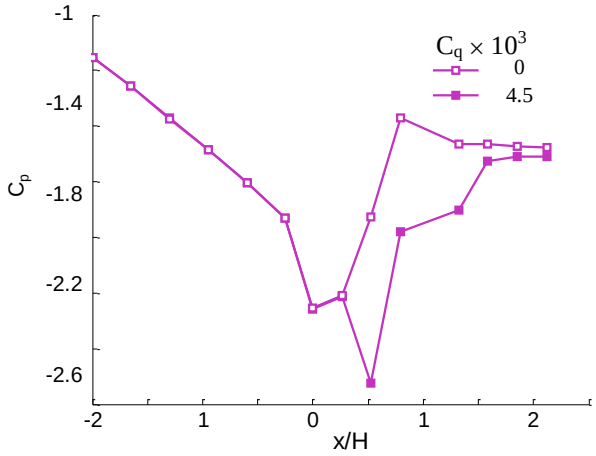

Figure 4.2 *Static pressure distributions over the curved surface insert in the absence and presence of actuation ($C_q \cdot 10^3$ = 0 and 4.5) at p_i/p_e = 1.34.*

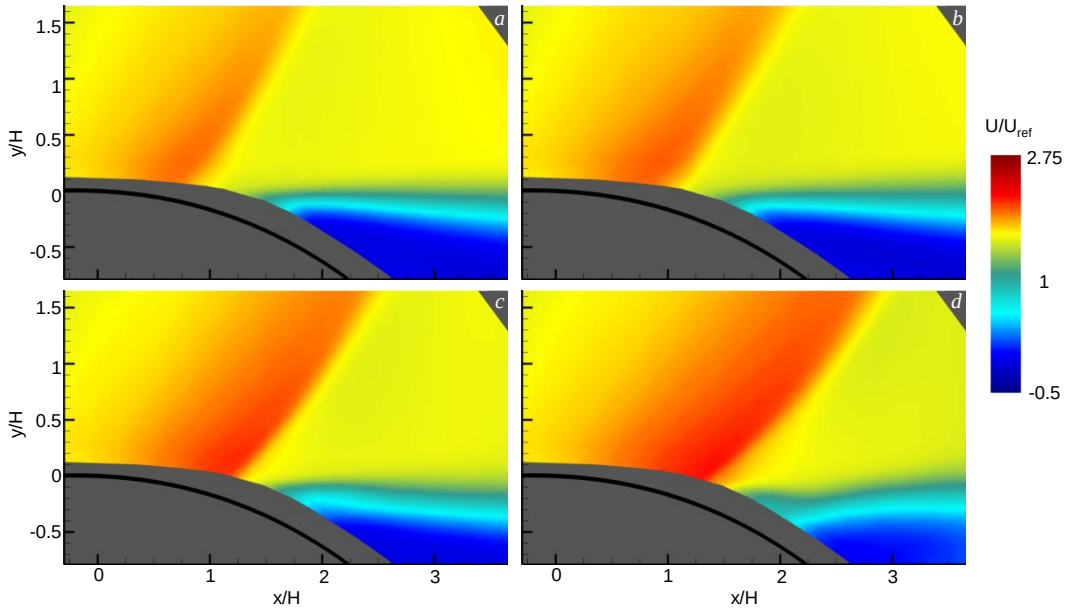

Figure 4.3*Color raster plot of the time-averaged streamwise velocity component (p_i/p_e = 1.34) in the absence of actuation (a) and with actuation at $C_q \cdot 10^3$ = 1.7 (b), 2.8 (c), and 4 (d).*

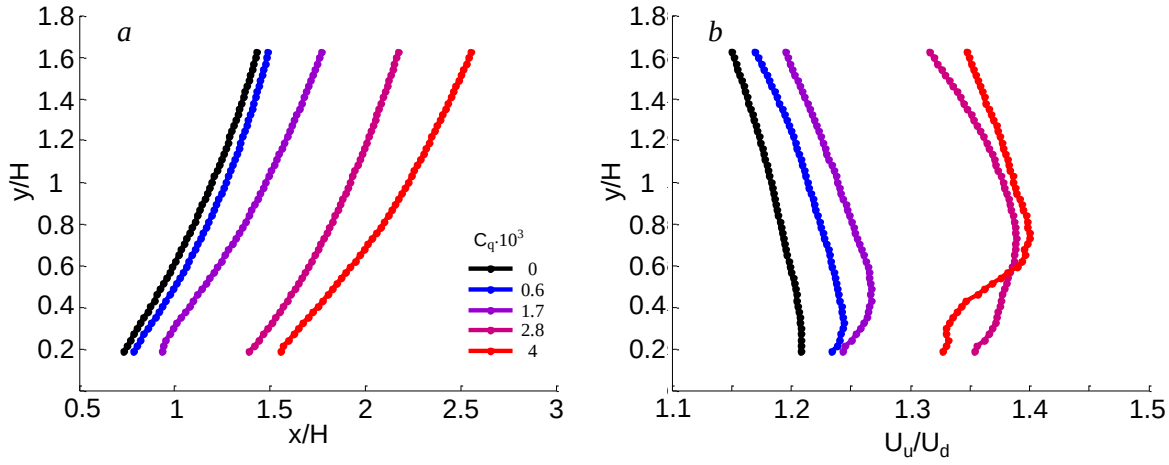

Figure 4.4 *Time-averaged (p_i/p_e = 1.34) cross stream shock profiles (a), and cross stream distributions of the velocity ratio (upstream, U_u, and downstream, U_d) across the shock).*

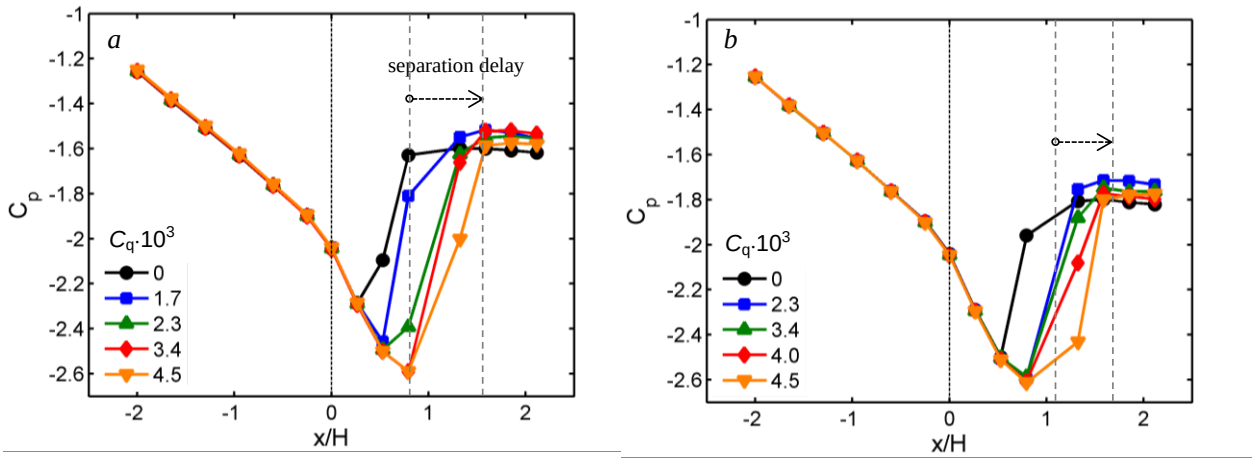

Figure 4.5 *Static pressure distributions along the curved insert for the base flow (•) and at varying actuation levels C_q at p_i/p_e = 1.32 (a) and 1.39 (b).*

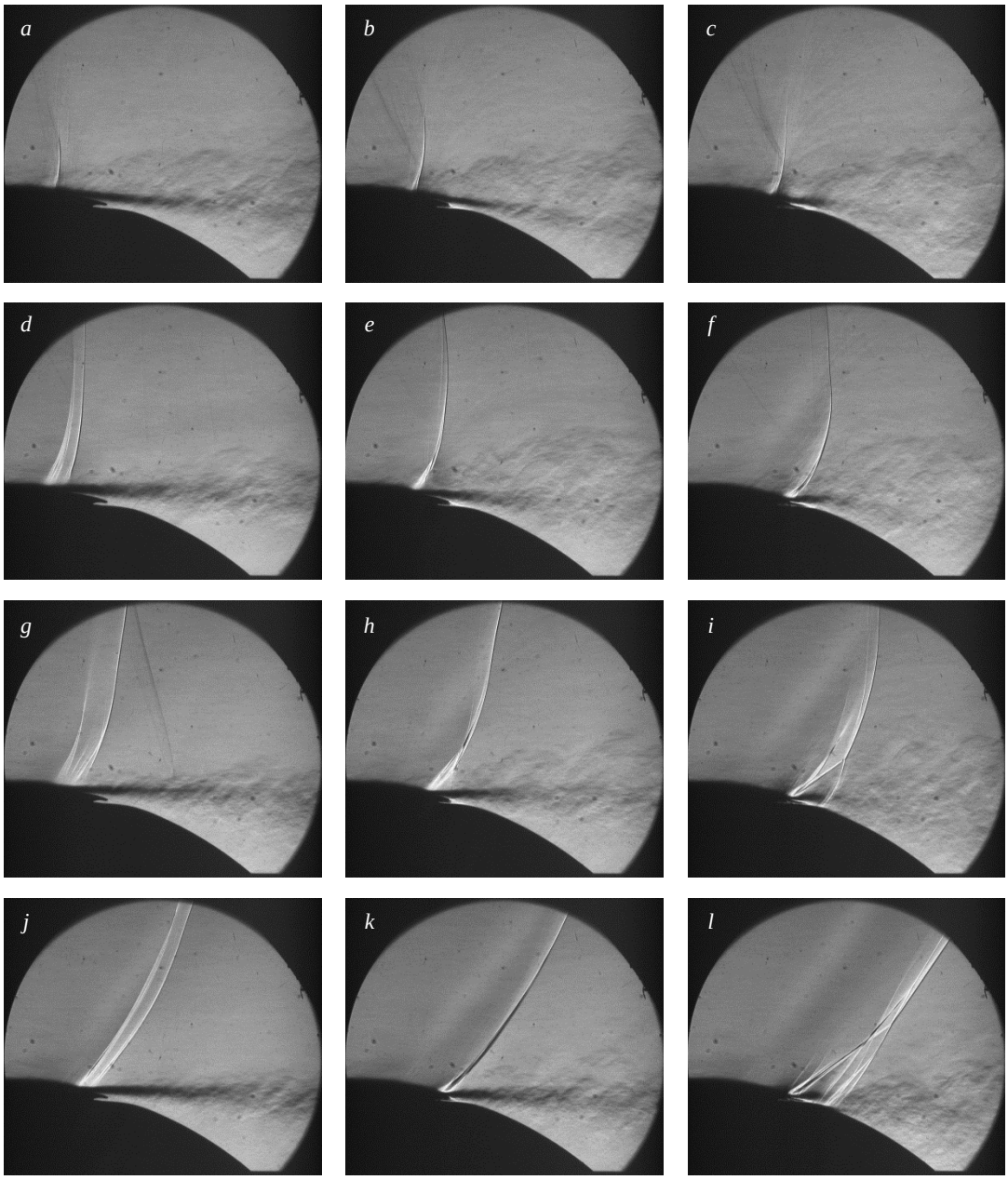

Figure 4.6 *Schlieren visualization at p_i/p_e = 1.25 (a-c), 1.29 (d-f), 1.34(g-i), and 1.39 (j-l), for $C_q \cdot 10^{-3}$ = 0 (a, d, g, j), 2.3 (b, e, h , k), and 4.5 (c, f, i, l).*

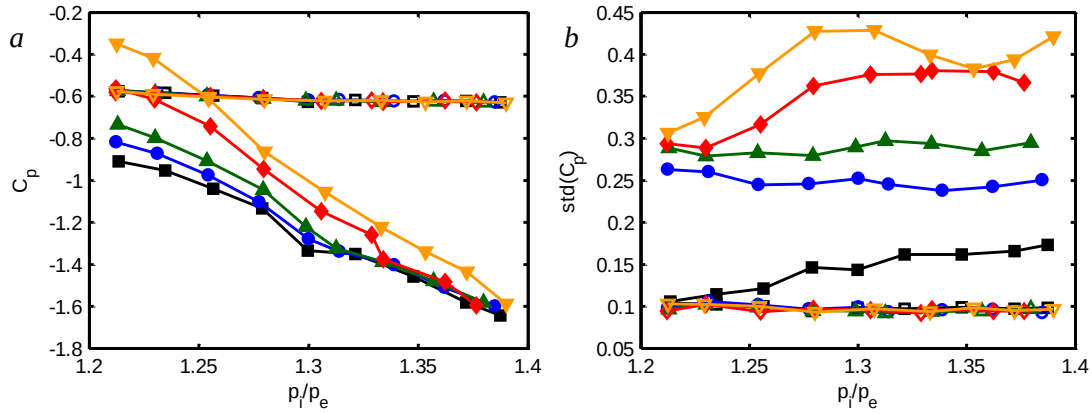

Figure 4.7 *Variation with p_i/p_e of the time-averaged (a) and standard deviation (b) of the dynamic pressure sensors p_{d1} (open symbols) and p_{d2} (solid symbols) for $C_q \cdot 10^3$ = 0(■), 0.6 (●), 1.7 (▲), 2.8 (♦), and 4 (▼).*

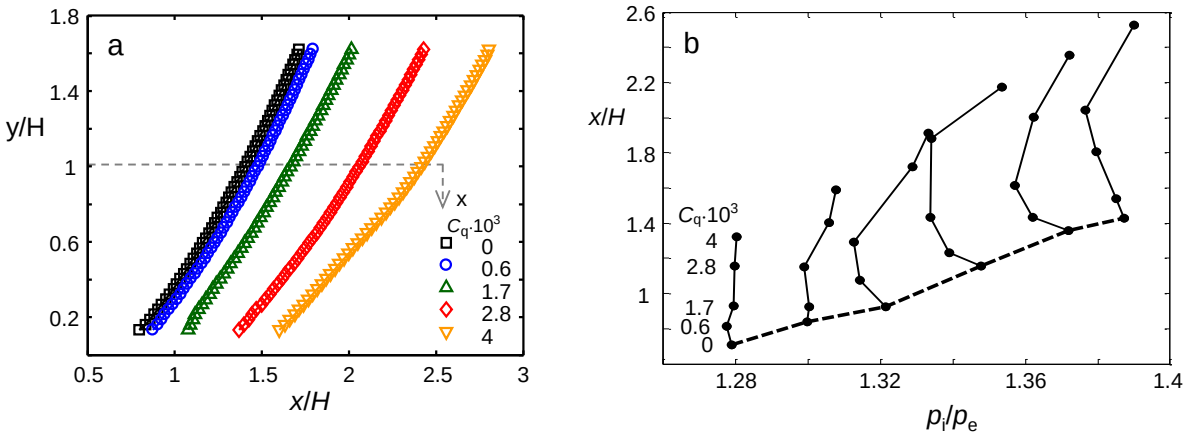

Figure 4.8 *a) Time-averaged cross stream shock profiles at p_i/p_e = 1.36, and b) Variation of the shock position x/H with p_i/p_e for $C_q \cdot 10^3$ = 0, 0.6, 1.7, 2.8, and 4. The setting of p_i/p_e for the base flow (C_q = 0) is marked with a dashed line.*

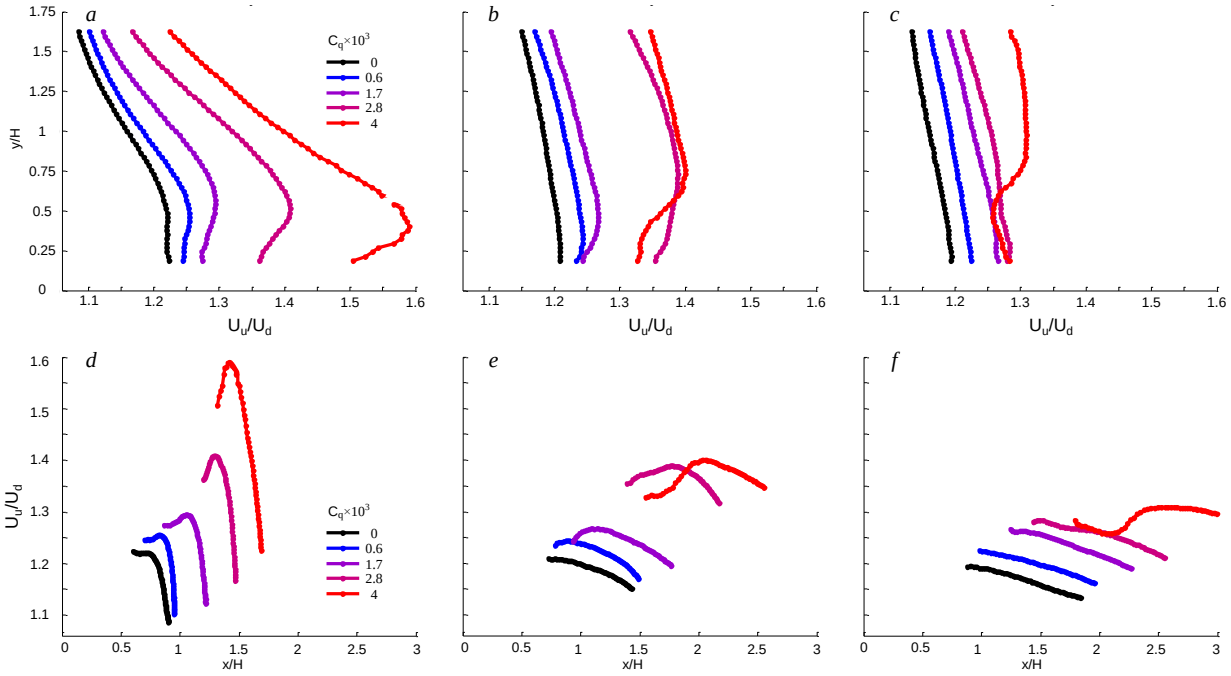

Figure 4.9 *Time-averaged cross stream (a-c) and (streamwise) variations of the velocity ratio across the shock at p_i/p_e = 1.30 (a, d), 1.34(b, e) and 1.39 (c, f).*

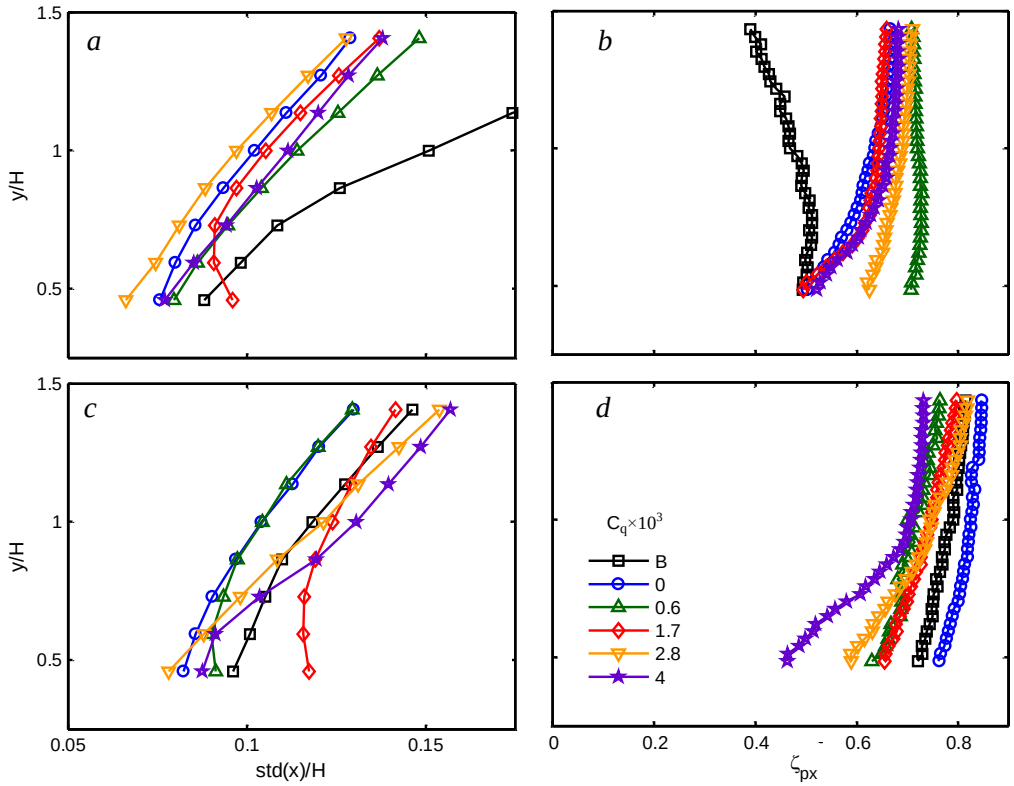

Figure 4.10*Cross stream distributions of the standard deviation of the shock position (a, c) and of the cross-correlation between the shock position and the pressure p_{d2} (b, d) for the base flow 'B' and in the presence of actuation at different levels C_q for p_i/p_e = 1.32 (a, b) and 1.36 (c, d).*

CHAPTER 5

THE DYNAMICS OF ONSET AND TERMINATION OF FLOW CONTROL

5.1 Introduction

This chapter focuses on the characteristic time scales associated with the onset and termination of the quasi-steady jet actuation that affects the evolution of the shear layer that is formed by induced separation downstream of the shock. These time scales are investigated using transient actuation that is effected by pulsed jets having rapid rise and fall time, and thereby provides a clear phase reference, unlike the quasi-steady actuation using fluidically-oscillating jets as described in Chapter 4. As described in Chapter 2, the spanwise pulsed jet actuator array includes seven equally-spaced jets (each orifice measuring 1.5 × 1.5 mm, 7.5 mm apart), is interchangeable with the fluidic oscillator jets and is integrated into the tunnel's test section so that the flow interface is virtually identical (the same air supply is used). The jets have a frequency response of up to 900 Hz and are operated using a square-wave actuation waveform at 50% duty cycle. Furthermore, since the pulsed jet operation is controllable externally (unlike fluidically oscillating jets), the jets offer an opportunity for feedback control of the shock system for a number of applications in external and internal flows, including aero-optics.

5.2 Continuous Actuation

The effect of the actuation is first assessed by characterization of the effects of continuous jet flow on the base flow using measurements of the static pressure along the surface downstream from the elliptic profile of the duct ($3.5 < x/H < 6.5$, cf. Chapter 2). Streamwise distributions of the static pressure over a range of pressure ratios $1.17 < p_i/p_e < 1.42$ in increments of $p_i/p_e = 0.024$are shown in Figures 5.1a and b in the presence and absence of the jets; the jets are operated at a flow rate equivalent of $C_q = 4.5$

x 10^{-3}. The ratio of the mass flow rate of the jets to the mass flow rate through the test section (C_q) is used to match that examined in Chapter 3 with the fluidic oscillating jets. As the facility chokes at a $p_i/p_e = 1.3$, the C_q is considered to be nominally constant for all pressure ratios presented in this chapter. The static pressure in the base flow (cf., Figure 3.7) increases with streamwise distance over all pressure ratios as a result of flow divergence within the duct (the flow cross section increases past $x/H > 0$; the pressures shown here start at $x/H > 3.5$). As the pressure ratio across the duct increases, the static pressure (for a given p_i/p_e) decreases (i.e., becomes more negative) with increasing flow speed. At low speeds ($1.17 < p_i/p_e < 1.23$), the flow appears to form a closed bubble along the centerline, downstream of the ramp ($2.5 < x/H < 4.5$), thereby leading to a local favorable streamwise pressure gradient, that is followed by an expansion at the downstream edge of the measurement domain. In the presence of actuation, the streamwise distributions of the static pressure are significantly altered over the entire range of p_i/p_e. Above $p_i/p_e > 1.28$, the magnitude of the gradient decreases with increasing p_i/p_e, indicating local attachment of the separating shear layer as the pressure taps measure values downstream from the attachment point. The initial pressure increase is an indication of the flow attachment. However, the competing effects of the outer flow deceleration (which should generate an adverse pressure gradient) and local flow acceleration past the reattachment zone result in the pressure gradient becoming nearly zero up to $x/H \approx 6$ and more adverse thereafter. As the speed of the cross flow is increased, the pressure gradient becomes slightly adverse in the presence of actuation when compared to the pressure gradient without actuation (e.g. $p_i/p_e = 1.17$).

The primary features of the base flow that are inferred from surface oil visualization are discussed in Figure 3.3. The effects of actuation on the flows past the ramp are visualized downstream of the actuator within the domain $1 < x/H < 7$ (Figure 5.2b, d, f and h) for four pressure ratios $p_i/p_e = 1.17$ (subsonic), 1.3 (pre-choked), 1.35, and 1.4

(choked) transonic (the corresponding images for the base flow are also shown for reference).

Due to the physical dimensions of the pulse jet actuator modules, it was only possible to install jets within a certain distance of the wall of the test section. The location of the jets is indicated by the arrows shown in Figure 5.2. Examination of the baseline flow is repeated here for reference. Please see the discussion of Figure 3.5 for a detailed discussion of the baseline flow. While the flow separates across the entire span of the duct, the flow over the elliptic surface of the sidewalls is heavily influenced by a corner vortex. The recirculation of these corner vorticies traps the oil in these regions. The schlieren images (Figure 4.1) and the PIV data (Figure 4.3) show the shock at the same location and shape for the same conditions (p_i/p_e and C_q). Since the schlieren images are effectively is integrated across the span of the facility and the PIV is measured within the center plane, the fact that these two independent measurement techniques show similar shock structure indicates that the corner flows have a minimal effect on the shock structure. The imprint of the oil on the flat downstream surface in this region indicates that the flow is moving outboard away from the centerline of the duct. The oil-flow visualization of the controlled flows (Figures 5.2b, d, f, and h) points to virtually full attachment of the flow over the aft section of the ramp. At subsonic speeds (Figure 5.2 a and b), the jets force the oil off of the surface in the center region of the elliptic surface. With increasing pressure ratio (Figure 5.2d), the flow control devices are less effective at vectoring the high speed flow all the way down to the elliptic surface. This results in a lowered shear force along the surface which, in turn, results in less oil being forced off of the surface. This trend continues as the jets (which are run at the same C_q) become increasingly less effective at vectoring the main flow through the duct down to the surface. At the highest pressure ratios tested (Figure 5.2 h), there are significant quantities of oil left on the surface. It should be noted that the 'streaks' of oil left on the surface are coincident with the areas between jet orifices and therefore are exposed to less

flow. The presence of oil on the surface does not indicate that the flow is still separated. Rather, the presence of oil indicates that the velocity near the surface is decreased (for increased pressure ratio). The oil, which is trapped on the surface due to the rotating corner flows, does not appear to be significantly changed either due to increased pressure ratio or due to the presence of actuation. This indicates that the corner flow is nominally invariant with either parameter. The author recommends that these three dimensional effects be included in future studies which aim to control this nominally two dimensional separation over these types of elliptic surfaces.

It is instructive to examine the similarities between the effects of the fluidic oscillating jets (Chapter 4) and the pulse jets in the fully open configuration (steady jets). Figure 5.3 compares the time-averaged values of the first downstream dynamic pressure sensor as a function of pressure ratio (p_i/p_e), for the case where the fluidic oscillators (FOs) and the pulse jets are running at the same C_q (cf. Figure 4.7a). As with Figure 4.7a, the pressure in the absence of flow control ($C_q = 0$) downstream from the apex of the contraction decreases with increasing pressure ratio. This is due to the fact that, in this pull-down facility, the suction provided by the blower fan is applied to the downstream end of the test section. There is an offset between the curve shown in Figure 5.3 that represents the base flow ($C_q = 0$) for the pulse jet and the equivalent curve for the FOs. In order to compare these plots the C_p have been offset and normalized by the ($p_i/p_e = 1.21$). This offset is most likely due to a slight error in the measured atmospheric pressure as indicated by an offset over the entire range of pressure ratios measured. The difference between the trends in these two base flows ($C_q = 0$) is due a common plenum for all of the fluidic oscillators. Due to this common plenum, spanwise non-uniformities in the flow over the elliptic surface cause flow to enter the jets in some areas and exit in others. It is thought that this effect causes the FOs to have a similar effect when both active and inactive at high pressure ratio. When the flow control is active, both curves are shifted vertically to higher pressures. While this shift is observed for both the fluidic oscillating

jets and the pulse jets, in the case of the fluidic oscillating jets, the pressure measured at the p_{d2}sensor linearly approaches the $C_q = 0$ curve until, at $p_i/p_e = 1.38$, the value becomes the same. However, despite this, the curves that represent $C_q = 4.5 \times 10^{-3}$ are nominally the same for both fluidic oscillators and pulse jets in the steady on configuration.

Two pressure ratios are examined in Figure 5.4 to elucidate the structure of the shock and separated shear layer and to compare the effects of the pulse jets in the steady on configuration and the fluidic oscillators at the same C_q. For both flow control strategies, a lambda structure, having the leading leg coincident with the array of flow control devices, is formed by the step change in surface boundary conditions. Additionally, in both cases, downstream translation of the trailing leg of the lambda shock and an increase in forward tilt of the main shock as the shock transitions toward an oblique shock are observed for increasing pressure ratio (Figure 5.4a and c vs. Figure 5.4b and d). The major, and most relevant, differences relate to how the shear layer is influenced differently for the two flow control devices. In Figures 5.4 c and d, the steady state pulsed jets are seen to reattach the separated shear layer. This is indicated by the expansion waves which are conformal to the surface downstream from the trailing leg of the lambda shock, and the absence of a separated shear layer. In contrast, the fluidic oscillators generate a large increase in the thickness over which the shear layer is spread. This is caused by the introduction of small scale structures which greatly enhance mixing. Although the shear layer is vectored toward the wall, the increased thickness of the shear layer (as can be seen in Figure 5.4a compared to Figure 4.6i) reduces the change in downstream cross sectional area when compared to the attached shear layer observed in Figure 5.4c. Furthermore, it is observed that the upper boundary of the influence of the fluidic oscillating jets at higher pressure ratios (Figure 5.4b) is nominally horizontal in nature. As this causes a similar downstream gradient in effective cross sectional area, compared to the baseline flow which has a nominally horizontal separated shear layer, the

pressure in the separated region is also nominally the same for the case where the fluidic oscillators are active and inactive, and explains the trends shown in Figure 5.3 vs. Figure 4.7a.

5.3 Step Jet Actuation

The transitory flow dynamics associated with the onset and termination of step jet actuation from and to an inactive state are investigated when the jet actuator is driven at the same upstream pressure as in the experiments described in Figure 5.1. These transitions of the jet actuators are first characterized in quiescent air (Figure 5.5) using hot wire anemometry to assess the performance of the actuator (which is clearly controlled by the internal electromechanical hardware). The hot wire sensor is placed 2mm downstream from and along the centerline of the jet orifice. The output of the anemometer is sampled phase-locked to the actuation command that is provided by the laboratory computer (Figure 5.5a). All times are non-dimensionalized by the reference time (T_r = 0.151ms). The reference time is computed using the distance from the apex of the contraction (x/H = 0) to the end of the elliptic surface at x/H = 2.46), and the velocity is the speed at x/H = 0, y/H = 1, at p_i/p_e > 1.29. The mass flow rate (jet strength) is non-dimensionalized by $\rho_o U_o$, which corresponds to the steady state values measured after the jets have been open for two seconds. The rise time between 0.1 $\rho_m U_m$(the maximum value measured) and 0.9 $\rho_m U_m$is $2T_r$. Following the step command at t/T_r = 0, there is a delay of about 5.3 T_r(owing to the inductive circuit of the actuator) before there is a rapid increase in the jet speed. The response of the jet speed resembles the response of an over damped second-order system with an overshoot to $\rho_m U_m$and the jet's strength reaches 0.9 $\rho_m U_m$approximately 2.6 T_r following the peak and reaches a nominally constant

level of 0.8 $\rho_m U_m$, 17.9 T_r following the peak. The decrease in jet strength following the termination of the actuation is shown in Figure 5.3b (time is measured relative to the termination of the actuation). There is a notable difference between the decay and rise times. The characteristic relaxation time between 0.9 $\rho_m U_m$ and 0.1 $\rho_m U_m$ is 178 T_r. The longer timescale is attributed to the internal structure of the valve and the direction of the pressure in the line relative to the required motion of the actuator valve. Furthermore, the jet speed exhibits spikes at $t/T_r = 10$ and 16.5 which are associated with the actual motion of the actuator valve. This disparity in times may have some effect on the dynamics of the actuation by the valve.

The response of the flow to the onset and termination of the top-hat jet actuation wave form is characterized first by schlieren visualization, which is captured using a high-speed video camera at a frame rate of 8 kHz. The response of the flow when $p_i/p_e = 1.17$(i.e., subsonic flow through the channel) and $C_q = 5.5 \times 10^{-3}$ following the onset of actuation at $t/T_r = 4.6$, 7.9, 14.6 and 25.2 ($t = 0$ corresponds to the trigger signal sent to the jets, $T_r = 0.15$ms, speed measured at $y/H = 1$, $x/H = 0$ for $p_i/p_e \geq 1.29$, over the elliptic surface which extends from $x/H = 0$ to $x/H = 2.65$) is shown in Figures 5.6a-d, respectively. At this low pressure ratio, the flow is attached through the location of the (nearly tangential) injection slot of the control jets ($x/H = 1$) but separates at the edge of the orifice overhang. The separated shear layer is clearly visible in Figure 5.6a. As the jet speed increases, the shear layer thickens downstream of the jet overhang and deflects towards the surface indicating increased entrainment by the actuation as shown in Figure 5.6b. As the jet speed continues to increase (Figure 5.6c), the shear layer becomes significantly thinner as the jet becomes a wall jet along the curved surface. At $t/T_r = 25.2$ (Figure 5.6d), the jet reaches its full speed (cf. Figure 5.3) and appears to be attached through the downstream extent of the elliptic surface ($x/H = 2.65$).

As the pressure ratio is increased to $p_i/p_e = 1.3$, a shock forms downstream of the surface apex at $x/H = 0.6$, as shown in Figure 5.7a at $t/T_r = 4.6$ (cf. Figure 4.6d). The presence of the shock leads to flow separation downstream of the shock, as is evidenced by the formation of a shear layer. It appears that the separation begins where the shock coincides with the surface boundary layer. As the jet speed increases with the opening of the valve at $t/T_r = 7.9$ (Figure 5.7b), the shock moves rapidly downstream due to the changes in the downstream boundary conditions. It is estimated that the shock is moving at a significant fraction of the speed of sound in this region. The motion reduces the shock's strength, as indicated by the reduction in the intensity of schlerie which are proportional to the density gradient, resulting in a shock that appears less distinct. The cross-stream extent of the shock is reduced during this downstream translation. This is due to the downstream boundary conditions changing rapidly enough to prohibit the formation of a shock in that region. The disappearance of the shock in this area is an indicator that the location that the boundary condition would cause to form a shock is moving downstream faster than the local speed of sound. A compression wave, which can be seen coming down from the opposite surface of the wall, is thought to be generated by slight non-uniformities in the corners on the opposite surface and are henceforth ignored as they should have minimal impact on the shock of interest. At $t/T_r = 14.6$ (Figure 5.7c) the shock reaches its most downstream location. The presence of jets which occur at the overhang edge leads to a step change in surface boundary conditions and the formation of a lambda shock. As the jet speed decreases to its steady level (cf. Figure 5.5a), the shock retreats upstream and the root of the shock becomes almost coincident with the location of the flow control at $x/H = 1$.

Figure 5.8 shows the corresponding transient evolution of the flow with increasing jet speed at $p_i/p_e = 1.35$. When the jet is relatively weak ($t/T_r = 3.3$, Figure 5.8a), the shock is very similar to that observed when the flow control is inactive (cf. Figure 3.2d). The multiple "shock lines" in the image are a result of span-wise non-uniformities in the base

flow. As the jet speed increases (at $t/T_r = 7.9$, Figure 5.8b), the shock motion downstream is faster than at the lower pressure ratio (Figure 5.7). This results in a weakening of the typical transonic shock structure as is evidenced in Figure 5.8b. This is attributed to a decrease in the flow speed relative to the shock (as the shock moves downstream), which results in a decrease in the shock strength, and therefore diminishes its contrast in the schlieren image. As discussed in Chapter 3 (cf. Figure 4.8 and 4.9), the interaction of the actuation jets with the cross flow leads to attachment and to global changes in the cross flow that result in profound effects on the shock position and structure. When the jet has reached its maximum speed, the flow upstream and downstream of the overhang appears to be completely attached (Figure 5.8c, $t/T_r = 2.2$), and the shock migrates downstream and develops a lambda-like structure such that the upstream leg of the lambda shock coincides with the edge of the actuator's overhang ($x/H = 1$), and the downstream normal segment of the shock coincides with the surface boundary further downstream. Once the upstream leg of the lambda shock anchors to the orifice and the flow, under the jet actuation, continues to be vectored further downward, the main shock, including the downstream leg of the lambda shock, becomes slanted in the streamwise direction as it translates downstream. The leading leg of the lambda shock is weaker compared to the corresponding shock segment at this elevation in Figure 5.8a ($t/T_r = 3.3$), as evidenced by the formation of the trailing leg the lambda shock. Between the upstream and downstream legs of the lambda shock, the jets attach the flow on the curved surface, causing the flow to diverge in that region. As this flow is still supersonic, it continues to accelerate in this diverging section. The flow continues to speed up and turn and undergoes normal shock segment of the lambda shock as seen in Figure 5.8c. Past the peak jet speed (cf. the overshoot of velocity in Figure 5.5a), as the jet reaches a nominally constant speed, the shock moves slightly upstream (Figure 5.8d).

As shown in Chapter 3 (Figure 3.2e), at the highest pressure ratio of the present experiments ($p_i/p_e = 1.4$, Figure 5.9), in the absence of actuation, the shock is nearly

oblique (unlike the curved shocks at lower p_i/p_e which is indicative of transonic shocks), and its streamwise position at the root of the shock is closer to the edge of the actuator's overhang ($x/H = 1$). Furthermore, the separated flow appears to spread farther into the cross flow at this higher flow speed. Similar to the flow shown in Figure 5.8, the motion of the shock with the increase in jet speed is accompanied by its weakening ($t/T_r = 6.6$, Figure 5.9b). The change in shock speed can be inferred from Figure 5.12. Similar to the lower pressure ratios, the shock has a lambda structure at the farthest streamwise position with an apex that is outside the shlieren field of view, and the flow is attached within the supersonic domain downstream of the upstream shock segment ($t/T_r = 11.3$, Figure 5.9c). Downstream of the normal segment of the shock, the flow appears to be attached as indicated by the lack of a separated shear layer. As the shock moves upstream when the jet speed diminishes to its quasi-steady level, the lambda shock structure becomes smaller, as the downstream leg of the shock, and the main shock translate upstream and the apex is within the field of view ($t/T_r = 79.4$, Figure 5.9d). Note that the expansion waves of the supersonic jet are visible downstream from the trailing leg of the shock along the surface. It is unclear as to why these waves are not visible in Figure 5.9c when the jet speed is higher.

The flow dynamics associated with termination of the actuation were investigated in a similar fashion to the onset dynamics. Figure 5.10 shows the evolution of the flow when the jet flow is turned off at $p_i/p_e = 1.35$ (Figure 5.8). As is illustrated in Figure 5.5, the time scale of relaxation to the base flow following the termination of the actuation is considerably longer than the onset time. During this time, the shock position retracts upstream with the decrease in jet speed. For these measurements, the actuation jet is activated for two seconds prior to the termination of the actuation to ensure the jet velocity and facility conditions have fully stabilized and, consequently, Figures 5.6d and 5.8a are nominally the same. As the jet speed diminishes, the induced low pressure near the surface downstream of the shock increases and the adverse pressure gradient leads to

flow separation over the curved surface. During the slowdown of the actuation jet, the lambda shock structures collapse and the shock moves upstream ($t/T_r = 1.2$, Figure 5.10b). The shock position is shown in Figure 5.12b. As the jet speed continues to diminish ($t/T_r = 2.2$, Figure 5.10c), the separation point continues its motion upstream and, as a result, the separated shear layer downstream from the shock continues to become more horizontal. Finally, after the jet vanishes ($t/T_r = 4.2$, Figure 5.10d), the shock moves to its unactuated upstream location (cf. Figure 3.2e).

The shock's position and shape during the actuation are extracted from the schlieren images using digital processing as depicted in Figure 5.11. First, a background image is subtracted from the raw schlieren images in order to increase the contrast between the shock and the rest of the field, resulting in the image seen in Figure 5.11a. Following the subtraction, the contrast between the shock and the background is enhanced by applying a threshold to the image, which sets any pixel values below a specific threshold to zero. Additionally, any values above that threshold are set to one. Next, the enhanced images are sorted by their delay relative to trigger of the actuation onset and then the images are summed. This results in a map where the magnitude corresponds to the number of times a shock has been in that particular location. This map is plotted in Figure 5.11b. This is followed by the shock positions being 'binned' at each of the elevations through the generation of histograms at each elevation. As an example, the histogram of the shock position at a given elevation (marked by a dashed white line in Figure 5.11b) is shown in Figure 5.11c. This histogram is used to determine the most probable shock position by fitting a Gaussian curve to the histogram and taking the peak of the curve fit. The process is repeated for all elevations, and the distributions and the shock position are shown Figure 5.11d.

The statistical image analysis method described above is used to analyze the time-varying position of the shock following the onset and termination of the actuation. As an illustration, Figures 5.12a and b show waterfall plots of the time-dependent shock

displacement at different elevations along the shock following the onset and termination of the actuation, respectively (p_i/p_e = 1.35). Each trace represents a specific y-elevation along the shock (cf. Figure 5.11d) as denoted by the color bar. In this manner, the shape of the shock can be determined by the distribution of these traces at any point in time; for example, at t/T_r = 64 the shock is nearly vertical as indicated by the fact that at each measured y-elevation the streamwise position of the shock is the same. In Figure 5.12a and b, time is measured relative to the change in the (top-hat) actuation wave form so that Figure 5.12a $t/T_r < 0$ represents the shock position in the base flow, while in Figure 5.12b the shock position at $t/T_r < 0$ is the "asymptotic" position in the presence of steady jet actuation. The vertical spread in x/H is an indicator of the degree of the streamwise inclination of the shock along its height. The data in Figure 5.12a, show the delay of t/T_r in shock displacement following the onset of actuation before the shock begins to move in the streamwise direction. Figure 5.12a, indicates that the shock motion begins at elevations close to the surface and propagates to higher elevations with time. The shock angle (as measured by the vertical spread in the traces of Figure 5.12a) becomes noticeably more vertical during the rapid downstream motion. The time rate of change of the shape of the shock (~4.25[(x/H)/s])is a reflection of the rate at which the evolution of the separated flow varies downstream of the actuators. As a result of this motion, the shock becomes more of a normal shock as represented by a clustering of the lines. The rise time of the shock at y/H = 1 is estimated to be $\Delta t/T_r$ = 8.6, which is much longer than the time associated with the rise time of the jet velocity. As the shock reaches its farthest streamwise position and its downstream translation ceases, the spread in the traces indicates significant streamwise tilt. Following the shock reaching its most downstream position (t/T_r = 20), the shock position relaxes back upstream toward its steady state location, which once again results in a nominally vertical shock shape as indicated by the coincident curves in $t/T_r > 45$. It should be pointed out that the shock stabilizes (reaches its nominally steady state position) after a period of about t/T_r = 43 (cf. Figure 5.8d). The

cross stream shape of the shock in the presence of actuation is reflected in distribution of the curves in Figure 5.12b at $t/T_r < 0$.

Figure 5.10b shows the corresponding time traces of the shock streamwise position following the termination of the actuation (at $t/T_r = 0$). The motion of the shock follows the temporal variation of the jet speed (cf. Figure 5.5b); the slower shock motion corresponds with a much longer fall time of the jet speed. It is noted that the two peaks in the speed of the actuation jet (cf. Figure 5.5b) are also reflected in the shock motion at $t/T_r = 15$ and 18. As a reminder to the reader, there are electromechanically actuated valves which control the flow to the flow control array. The two peaks in the motion of the shock (cf. Figure 5.12b) are thought to be caused by the valves bouncing during rapid closure. The retreating shock (upstream motion of the shock as indicated by the traces moving to lower x/H locations on the graph in Figure 5.12b) does not significantly change shape during the retreat back to the 'off' position, which is reflected in similarly spaced curves in Figure 5.12b (the spacing between the lines, and therefore the shock shape, is similar for $t/T_r = 40$ and $t/T_r = 70$). Hence, unlike the rapid motion of the shock seen at $t/T_r = 13$ in Figure 5.12a during the rapid onset of the actuation, (the motion of the shock is examined in more detail in Figure 5.18) during the termination of the pulse jets, the shock shape remains nominally the same. This indicates that the speed at which the shock travels back upstream during termination of the flow control is not rapid enough to change the relative oncoming velocity of the shock, indicating that this motion (ignoring the two spikes due to valve bounce) can be considered close to quasi-steady motion. In contrast, and as was discussed previously, the downstream motion of the shock during onset of actuation has a significant impact on the shock strength and shape and therefore is considered non-equilibrium motion of the shock. These two observations of the shock motion, during onset and termination of the flow control, provide what the author considers upper and lower limits on the rate at which flow control can affect the motion of the shock. The upper limit in shock motion is defined by the rapid downstream motion

observed during the onset of actuation (cf. Figure 5.12a). While it is observed that during the onset of actuation the shock motion is a non-equilibrium process, the upstream motion of the shock during termination of the actuation is considered quasi-steady. For this reason, the motion and the timescale implied by the motion of the shock during the termination of actuation (cf. Figure 5.12b), define a lower limit. This lower limit implies that the shock can be forced to change position faster than the motion indicated in Figure 5.12b. The flow conditions in the downstream separated region (cf. Figure 5.3, for more details on the downstream separated region) that are affected by control of the separated shear layer are further examined using pressure sensors placed in the separated region.

The pressures measured by the downstream dynamic pressure sensors (p_{d2}, p_{d3}, p_{d4}), are smoothed before being plotted. This is due to electrical noise which appears in the data at ~ 7kHz. This noise is indicated in the power spectra shown in Figure 5.13 and a smoothing function is applied to the data to reduce the amplitude of this noise. The smoothing function is a built in Matlab smoothing function referred to as 'rlowess' which is a local regression that uses a weighted linear least square fit and a first degree polynomial where a lower weight is assigned to outliers in the regression. A standard filter is not used in this case as the digital filters affect the rate of change of the signal more than desired by the author.

The flow field response to the transient onset and termination of the actuation was also characterized using three dynamic pressure sensors downstream of the ramp at x/H = 3, 4, 5 (cf. Chapter 2) that are sampled phase-locked to the actuation waveform. The pressures are plotted on the same scale as Figure 5.12. Figures 5.14a and b show the pressure traces during the onset and termination of the actuation, respectively, for a pressure ratio of p_i/p_e = 1.35. Similar to the data for the shock position (Figure 5.12a), there is a delay between the actuation trigger (at t/T_r = 0) and measurable changes in the pressure traces. This delay is due to the delay time between the trigger signal sent to the flow control and the time when the valves supply flow to the flow control array. This delay can clearly be

seen in Figure 5.5a. Additionally, the delay is caused by the convective delay. The changes in pressure are first sensed by the upstream sensor (t/T_r = 5.27, x/H = 3, p_{d2}), followed by the middle sensor (t/T_r = 5.68, x/H = 4, p_{d3}), and then the most downstream sensor (t/T_r = 6.5, x/H = 5, p_{d4}). This time delay is related to the position of the sensor and the convective flow speed. The sensors which are further downstream are affected after a longer time period than the sensor immediately downstream from the curved surface. Consequently, the most downstream sensor (p_{d4}) is the last to register the change. For reference, the shock (the root of the shock) begins to move downstream at t/T_r = 5.57 (cf. Figure 5.12a) and the velocity of the jets begins to increase at t/T_r = 5.29 at p_i/p_e = 1.35 (for more details on the timing associated with the convective speed see Figure 5.15). Immediately preceding a rapid rise in pressure (associated with rapid motion of the shock (cf. Figure 5.14a t/T_r = 13.3), there is a drop in pressure for all three sensors most likely associated with the initial 'burst' of the jets disrupting the shear layer**.** Following this event, all three sensors measure a rapid increase in pressure. The rate of the increase is a function of pressure ratio, sensor location, and relative position of the sensor to the reattachment point. The rise in pressure is associated with the reduction in free stream speed over all three sensors due to the forced expansion of the flow as the flow control reattaches the shear layer. The rate at which these pressures rise indicate the rate at which the shear layer reattaches, for p_i/p_e = 1.35. After the overshoot at about t/T_r = 16.5, p_{d3} and p_{d4}begin to level off, while p_{d2} has a peak at about t/T_r = 66.3. It is thought that this peak is due to low frequency fluctuations in the jet speed which would not be detected by the other sensors simply due to their proximity to the jet. The time trace of sensor p_{d2}, Figure 5.11a, shows that, as the shear layer reattaches, the reattachment region moves (cf. Figure 5.2e and f) and causes a rise in pressure over this sensor. Due to the location of the sensors with respect to the reattachment region, p_{d2} and p_{d3} are very similar in magnitude preceding actuation ($t/T_r < 0$). For the same reason, the change in pressure measured byp_{d3} is larger than that of the other two sensors. It is

important to note that the characteristic times associated with these rapid changes in pressure are a strong function of pressure ratio (p_i/p_e) which will be examined in subsequent figures.

Figure 5.14b shows the time-resolved pressure responses after the flow with the pulse jets active is fully established and the pulse jets are suddenly terminated at $t = 0$. The flow field and, therefore, the pressures asymptotically reach a quasi-steady state with the flow control active. This process, the timescale of which is on the order of $t/T_r = 300$, is due to the time it takes for the wind tunnel facility to respond as well as the pressure in the air supply line to the flow control to stabilize. In order to overcome these issues, the jets are activated for 1.5 seconds prior to the termination of the flow control ($t/T_r = 0$). For this reason, the magnitudes of the pressures measured at $t/T_r = 0$, Figure 5.11b are different than those observed in Figure 5.14a at $t/T_r = 78$. It is interesting to note that all three sensors respond in a similar manner as both the jet velocity (Figure 5.5b) and the shock displacement (Figure 5.12b). Similar to the jet onset, p_{d2} still leads in response, and p_{d4} still trails in response. Therefore, there is a reduction in the delay between the jet pulse, shock displacement, and the flow/shear layer response. As the shock begins to retreat, the previously attached flow begins to separate, and the pressure within the growing separation bubble increases. It is interesting that the same ripples seen in the jet velocity and the shock displacement are also observed in all the pressure traces. Through observations of the rate at which the flow responds to these ripples, it is possible to estimate the timescales over which the flow can change. These changes point to the flow being sensitive to small perturbations on a time scale of about 0.4 ms, which corresponds to 2.5 kHz. The observed pressures slowly decrease until, similar to that which is observed at $t/T_r = 0$, the first two sensors reach similar magnitudes. The fact that there appears to be an offset in these pressures is due to the longer timescales mentioned at the beginning of this discussion. There are several conclusions that can be made from Figure 5.14. First, the rate at which the pressures respond to the flow control is very similar to

the changes observed in the shock position in that there is a much faster response of the sensors during onset of actuation then during termination. Additionally, many of the details of the shock motion are mirrored in the changes in downstream pressure (e.g. rapid motion, overshoot, etc). The time at which the downstream pressure rapidly changes due to the actuation of the flow control is a function of pressure ratio, as will be explored by comparing the same data presented in Figure 5.14 for a range of pressure ratios. These data are presented in Figure 5.15.

Time traces of the dynamic pressure measured by the three streamwise sensors (cf. Figure 5.14) were also recorded for $1.18 < p_i/p_e < 1.41$ for the onset and termination of the actuation and are shown using color raster plots for the onset and termination of the actuation in Figures 5.12 and 5.13, respectively. The pressure magnitudes in each of these traces are computed relative to the nominally-steady pressure at the specific p_i/p_e prior to the change in the actuation waveform (i.e., $t/T_r < 0$). All the trace maps demonstrate some delay in the onset of the actuation due to the delay time associated with the onset in the jet velocity (cf. Figure 5.5) and convective delays. All three contour plots in Figure 5.12 exhibit a momentary reduction in pressure following the onset of actuation at $t/T_r > 0$ which is represented in the color raster plots as a dark blue nearly vertical line. The duration of this reduction in pressure increases with distance from the actuator (the thickness of the dark blue line increases from p_{d2}, p_{d3} to p_{d4})due to a decrease in convective speed with streamwise distance and decreases slightly with increasing p_i/p_e, due to an increase in convective speed with p_i/p_e. The slope of this dark blue line is caused by a decrease in the delay time between the actuation trigger and the time at which the sensors detect this drop in pressure for increasing pressure ratio (p_i/p_e). This trend is attributed to the increasing convective speed as the disturbances generated by the flow control effects propagate downstream at higher speeds for the higher pressure ratios. The low pressure region (the dark blue band) is stretched over a longer time period for p_{d4}(compared to p_{d3} and p_{d2}) due to the expansion of the flow in this region.

The first sensor (p_{d2}), shown in Figure 12a, indicates that the delay timing is not as strong a function of pressure ratio as for $p_{d3}$and p_{d4}. This is concluded from the fact that the dark blue band, which indicates the time at which the sensors detect the changes imparted by the flow control, is a nearly vertical line at (t/T_r = 6.7), indicating that the timing is almost unaffected by the pressure ratio. This indicates that the dynamics measured by $p_{d2}$is dominated by the jet dynamics and depends weakly on the local speed of the cross flow. After the rapid increase in pressure measured by all three sensors, there are some interesting trends which are a function of pressure ratio. For example, both p_{d2} and p_{d3} measure higher pressures after the flow control has been switched on at pressure ratios greater than 1.32. It should be pointed out that, since the plots in Figure 5.12 are all differential plots (relative to the pressure prior to the jet trigger), these trends indicate a larger change in pressure imparted by the jets. While this seems contrary to what would traditionally be expected with most flow control applications (higher speed with the same actuation generally leads to diminished effects), it should be remembered that there are several important changes in the structure of the flow for pressure ratios greater than 1.3. At higher pressure ratios, the facility begins to choke (cf. Figure 2.6). The separation point moves further downstream (cf. Figure 3.2 and 3.3), and the reattachment region moves further downstream (cf. Figure 5.2). Of all of these changes, the changes in the location of the reattachment region are thought to contribute most to these trends. This is due to the fact at lower pressure ratios these two downstream sensors reside downstream from the reattachment point whereas, at higher pressure ratios, they are within the separated region.

Figure 5.16 presents the color raster plots of the dynamic pressures measured during termination of actuation (similar to Figure 5.15). First, there is progressively increasing delay for the pressure response after t/T_r = 0 with the downstream distance of the sensor for all of the pressure ratios. It is also interesting to note that the jumps in pressure observed in Figure 5.16b during the termination of the actuation(cf. Figures 5.12b and

5.14b) persist over a ***longer time*** with increased transducer distance from the apex (as observed and commented on above). The most notable feature is a marked decrease in the pressure difference at pressure ratios higher than $p_i/p_e = 1.34$ for p_{d2} and, inversely, an increase in the pressure difference for the other two sensors (p_{d3} and p_{d4}). The pressure ratio at which this is observed ($p_i/p_e = 1.34$) is close to the point at which the facility chokes.

The shock streamwise position at $y/H = 1$, following the onset and termination of actuation for $p_i/p_e = 1.3$, 1.35 and 1.41, is shown in Figures 5.16a and b. The position of the shock prior to the change in the top-hat actuation waveform is subtracted. Due to the long time scales associated with the shock reaching its nominally asymptotic position following the termination or onset of actuation, the position of the shock at $t/T_r = 0$ is different for onset and termination. This is because the actuation off shock positions are subtracted from these traces and, due to the fact that in the case of the actuation termination tests the flow control is pre-triggered at $t/T_r = -6622$. The time at which the shock begins its rapid downstream motion(Figure 5.14a), suggests that the position increments are the same for the three pressure ratios. The motion of the shock following the onset of the actuation is similar over the three pressure ratios. However, the shock begins its rapid downstream motion inversely proportional to the pressure ratio, where the shock begins to move sooner at the highest pressure ratio. This can be seen at around the $t/T_r = 6.6$ by the rapid motion of the shock occurring slightly earlier for higher pressure ratios. The magnitude of the increment in shock position is very similar for the three pressure ratios and suggests that the effects of reduced actuation momentum ratio, as the downstream velocity increases at higher pressure ratios, is offset by the downstream motion of the shock with increasing pressure ratio (cf. Figure 3.7), which causes the shock root to be in closer proximity to the actuation orifice as the pressure ratio increases. Another interesting feature is that, although the magnitude of the overshoot in the shock position ($16.5 < t/T_r < 26.4$) is nearly independent of the pressure

ratio, the relaxation following the overshoot is similar for $p_i/p_e = 1.3$ and 1.35 but is significantly longer for $p_i/p_e = 1.41$. This is thought to be due to the formation of a larger lambda shock when the flow control array is activated at higher pressure ratios as can be seen in Figure 5.9c and d.

The case where the jets are switched off is examined in Figure 5.17b. Although the change in shock position associated with the rapid downstream motion is similar for all three pressure ratios, the steady state position with the jets on, $t/T_r < 4.6$ in Figure 5.17b, indicates that the highest pressure ratio for the same jet power results in the shock moving further downstream with respect to its steady state position (larger $\Delta x/H$), an indication that, over a long period of time ($t/T_r > 80$), the flow control imparts a larger change in shock position for higher pressure ratios. At higher pressure ratios, the shock begins to move in response to changes in the jets at earlier time points due to the higher convective speeds. The jumps seen in the shock retreating motion are due to the corresponding jumps in the jet velocity (Figure 5.4). It is interesting to note that, at higher pressure ratios, these two spikes in shock location occur closer together, in a similar fashion to the two jumps measured in the downstream pressure (Figure 5.14b).

In order to compare the shock motion and the downstream pressures, the phase locked pressures from $t/T_r = 2$ to 16 and shock motion over the same time period are superimposed for three pressure ratios ($p_i/p_e = 1.3$, 1.35 and 1.4) are shown in Figure 5.18. Examining these two signals indicates some interesting trends. First, it is apparent that the rapid downstream motion of the shock begins at higher t/T_r for lower pressure ratios ($t/T_r = 11.2$, 10 and 8.6 for $p_i/p_e = 1.3$, 1.35 and 1.4 respectively). In addition, the slope of the rapid change in shock position decreases with increasing pressure ratio. It is thought that these two trends are due to the combined effects of changes in convective speed and changes in the rate at which the downstream boundary conditions are changed (i.e., the dynamics associated with the shear layer). In order to investigate these changes in downstream boundary conditions, the downstream pressure sensors are plotted on top

of the shock position in Figure 5.18. Starting with p_{d2}, both the time at which the pressure begins its rapid rise (t/T_r = 2.5) and the slope of the rapid increase in pressure are invariant over the range of pressure ratios shown in Figure 5.18 (p_i/p_e = 1.3 to 1.4), which is consistent with the trends seen in Figure 5.15a. Similar trends are observed upon examination of p_{d4}, where the slope is relatively consistent over the range of pressure ratios examined. However, the time at which the pressure begins to rapidly increase is slightly higher (t/T_r = 2.56) for p_i/p_e = 1.3 as compared to t/T_r = 2.47 for p_i/p_e = 1.35 and 1.4. Examination of p_{d3} shows a decrease in the time at which the sensor measures a rapid increase in pressure (t/T_r = 7.1, 6.6 and 6.0 for p_i/p_e = 1.3, 1.35 and 1.4 respectively) and the slope of the rapid change in pressure increases with increasing pressure ratio. The increase in the slope, with increasing pressure ratio of the rapid rise in pressure measured by p_{d3}, is the opposite trend to that which is observed in shock position, where the slope decreases with increasing pressure ratio. There are competing effects which change the shock and pressure rates of change. Increases in pressure ratio should increase the rate of change measured by the pressure sensors, both as the shear layer should reattach more rapidly (which is what causes the pressures to change) and because any increases in convective speed will cause the flow to convect over the sensors more rapidly. While these trends are measured by p_{d3}, as discussed above, the same trend in slope is not observed in the shock motion. This is due to the fact that, although the downstream boundary condition is changing more rapidly, the increased speed of the flow within which the shock is embedded results in a shock that responds less rapidly to changes. This is due to the fact that the changes in boundary condition need to propagate upstream through fluid that is moving at higher velocity. These changes are most apparent in these types of transonic flow where the rate of propagation of changes in pressure (speed of sound) is very close to the speed of the flow through which these changes need to propagate. It is instructive to examine the trends in rate of change of the pressure sensors as a function of pressure ratio. These trends are plotted in Figure 5.19.

The above discussion, along with the changes in the separated shear layer observed both in the schlieren images in this chapter and in the PIV in Chapter 3 (Figure 3.10), indicates that the downstream pressure sensors are measuring changes in pressure that correspond to changes in the shear layer position. By extension, the rapid rate of change of the separated shear layer position (and the changes in downstream boundary layer which drive the shock motion), as measured by the dynamic pressure sensors, is investigated by computing the first derivative of the pressure measured by each of the sensors (p_{d2}, p_{d3}, p_{d4}) during the onset of actuation. This derivative is computed over a timescale of $t/T_r = 1.08$ and is plotted for each sensor, p_{d2}, p_{d3}, and p_{d4} in Figure 5.19a, b and c, respectively, in a similar layout to that shown in Figure 5.12 for the onset of actuation. The derivatives are plotted from $t/T_r = 0$ to 13.3 and, on this scale, the convective delay discussed in conjunction with Figure 5.12 is more apparent. It is also interesting to note that the derivatives plotted in Figure 5.19 become weaker for each successive downstream sensor. There are a number of trends that are interesting as they relate to shock formation. At low pressure ratios ($p_i/p_e = 1.17$ - 1.23), the magnitude of the derivatives for all three sensors decrease for increasing pressure ratio. This is due to the increase in convective speed over the sensors, which 'stretches' the structures that are convected over the sensors resulting in a decrease in the rate of change measured by these sensors. At pressure ratios higher than 1.23, a shock begins to form, with a weak transonic shock fully formed by $p_i/p_e = 1.26$. As the transonic shock begins to form ($1.26 < p_i/p_e < 1.34$), there are several changes which occur. There is a shift in the timing of the first sensor (p_{d2}, Figure 5.19a) such that the rapid rise in pressure occurs later, most likely due to the change in angle of the separated shear layer during shock formation. However, p_{d3} and p_{d4} measure a local minimum in the derivative at $p_i/p_e = 1.29$. At $p_i/p_e > 1.29$, the shock moves the separation point further downstream, which results in the flow control array becoming closer to the separation point. It is thought that this contributes to a more rapid motion of the shear layer, resulting in the higher derivatives

measured by p_{d3} and p_{d4} for $p_i/p_e > 1.29$. At $p_i/p_e > 1.29$, the facility begins to choke (cf. Figure 2.6). While the derivative measured by p_{d3} continues to increase past $p_i/p_e > 1.29$, the derivatives measured by p_{d2} continue to decrease with increased pressure ratio. This is due to the fact that p_{d2} is responding to changes in the rate of the shock position (which moves at a reduced rate as the pressure signal now has to propagate around the supersonic bubble), whereas both p_{d3} and p_{d4} are responding to changes in the rate at which the shear layer is moving. This indicates that the shear layer is moving faster than the shock can respond, resulting in the non-equilibrium shock motion that is observed during the onset of actuation.

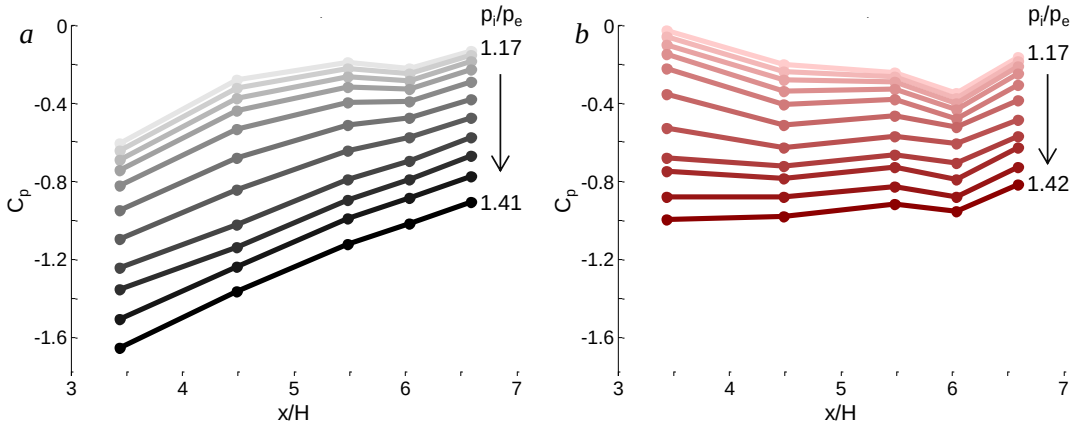

Figure 5.1 *Streamwise distributions of static pressure along the surface of the duct in the base flow (a) and with the presence of continuous jet actuation (C_q = 4.5 x 10-3) (b) at increments of p_i/p_e = 0.024 of the pressure ratios within the range 1.17 < p_i/p_e < 1.42.*

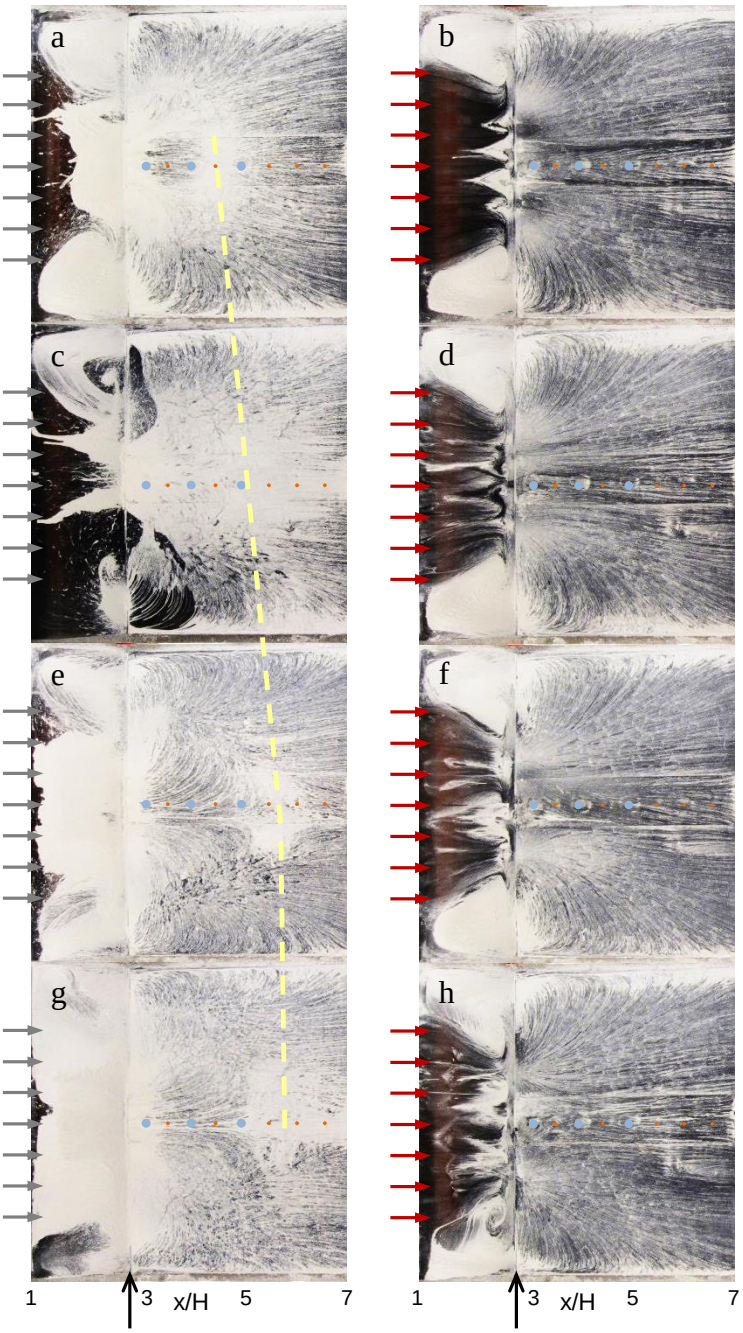

Figure 5.2 *Surface oil-flow visualization within the domain 1<x/H<7 across the entire span of the test section; the base flow (a,c,e,g) and in the presence of the continuous actuation jets (b,d,f,h) at p_i/p_e = 1.17 (a,b), 1.3 (c,d), 1.35 (e,f), and 1.4 (g,h). The spanwise positions of the actuation jets are marked by arrows on the left of each image. The arrow at the bottom of the figure indicates the end of the elliptic surface and the beginning of the planar section. The yellow dashed line indicates the approximate location of the reattachment region.*

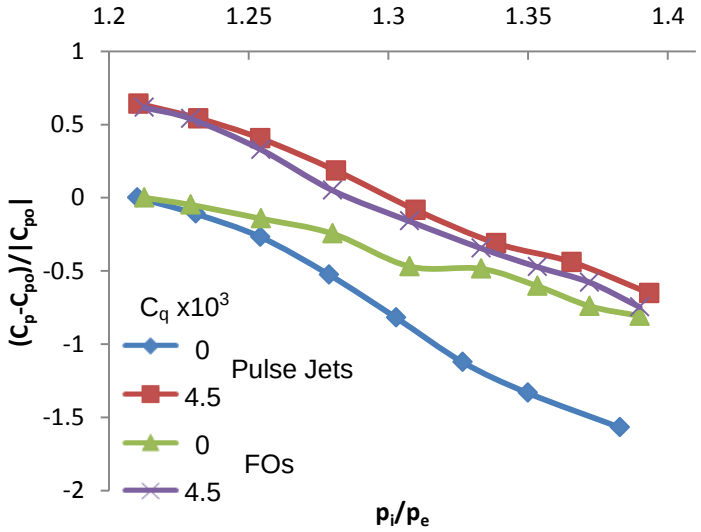

Figure 5.3 *Time averaged pressure measured at the first downstream dynamic pressure sensor (p_{d2}), comparing the effects of the fluidic oscillators (FOs) to the effect of the pulse jets operating fully open.*

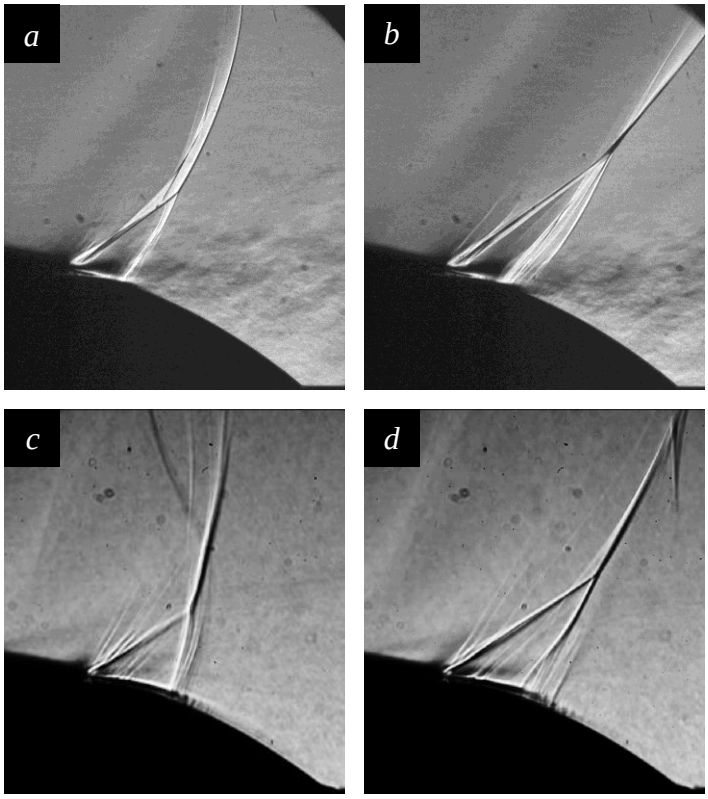

Figure 5.4*Schlieren images for the fluidic oscillators (a,b) at $C_q \times 10^3 = 4.5$, for $p_i/p_e = 1.35$ (a,c), and $p_i/p_e = 1.4$ (b,d), and the pulsed jets in the fully open configuration (c,d).*

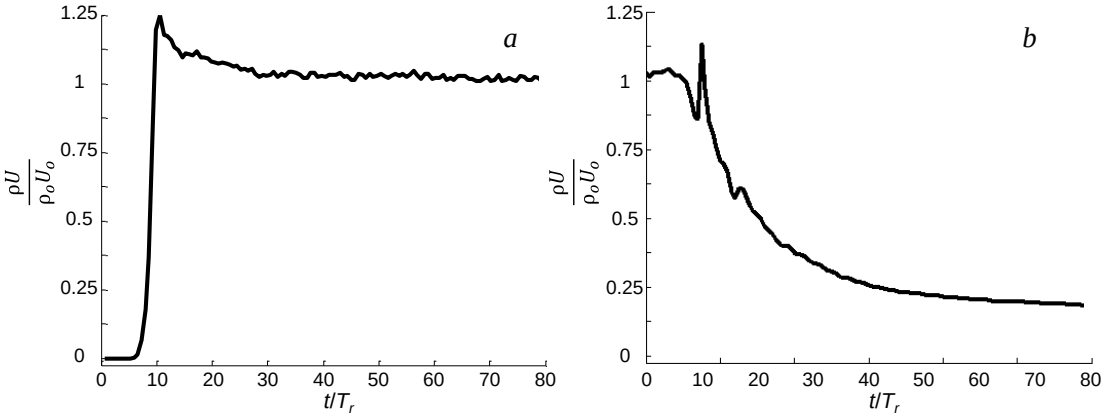

Figure 5.5 *Normalized jet speed following the onset (a) and termination (b) of the actuation at t = 0, where $T_r = 0.151$ms.*

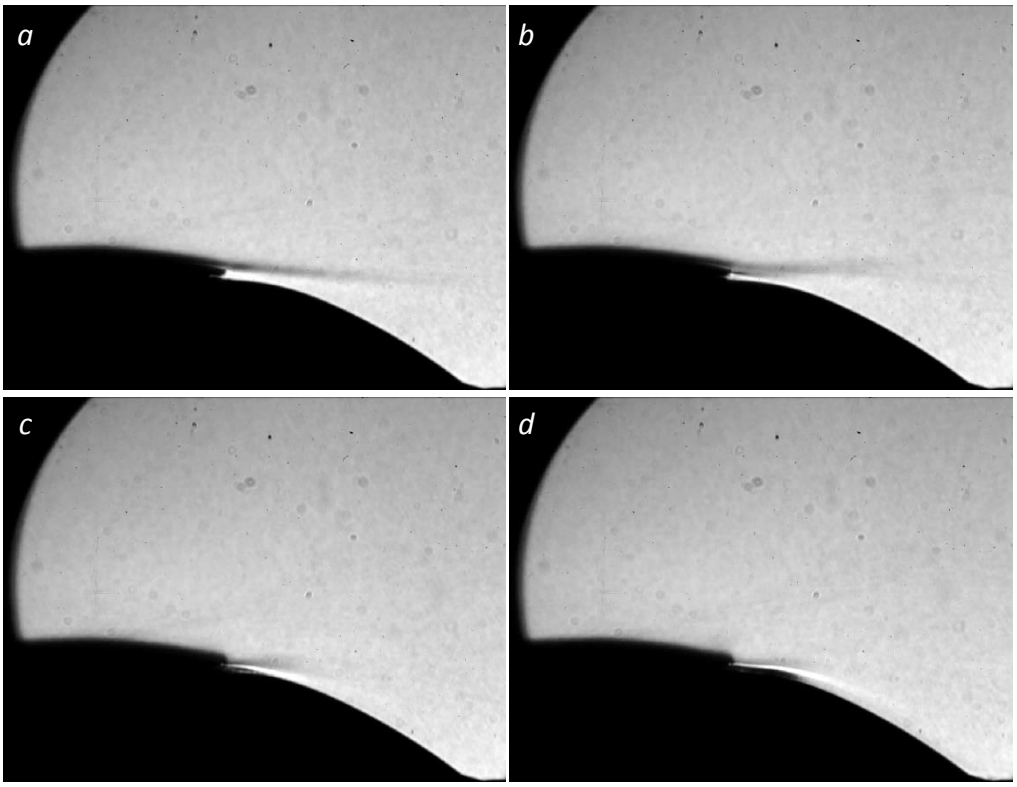

Figure 5.6 *Instantaneous schlieren visualizations of shock positions for t/T_r = 4.6(a), 7.9(b), 10.6(c), 17.2(d), following the jet trigger, for p_i/p_e = 1.17.*

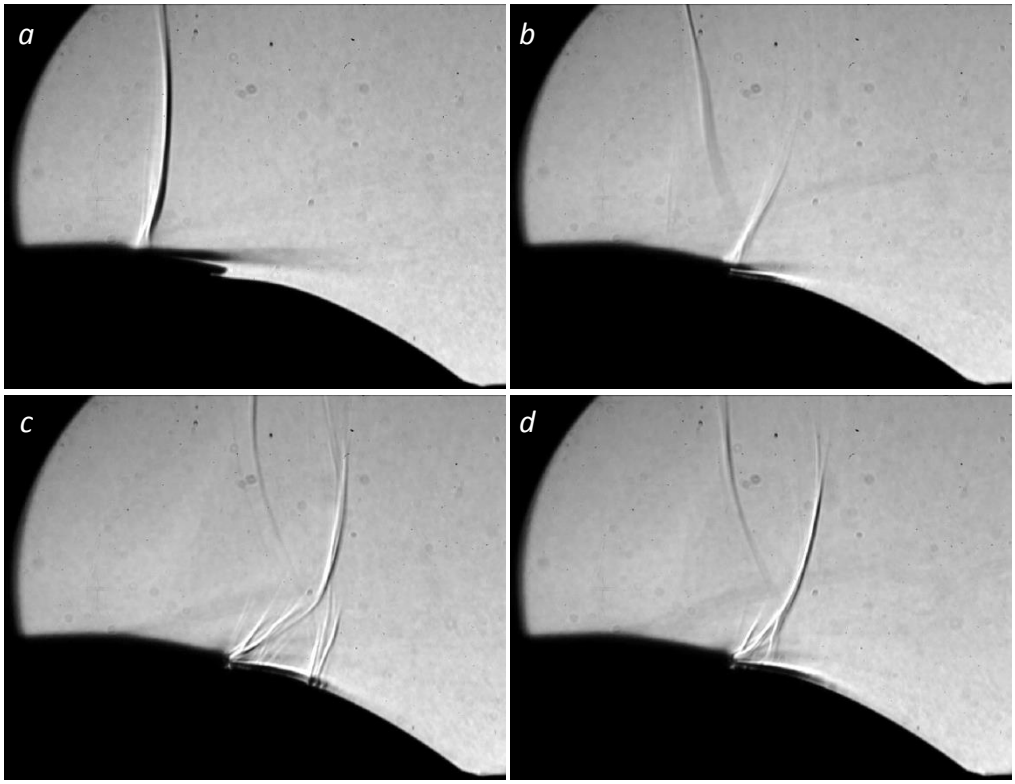

Figure 5.7 *Instantaneous schlieren visualizations of shock positions for t/T_r = 4.6(a), 7.9(b), 14.6(c), 25.2(d) after the jet is triggered, for p_i/p_e = 1.3.*

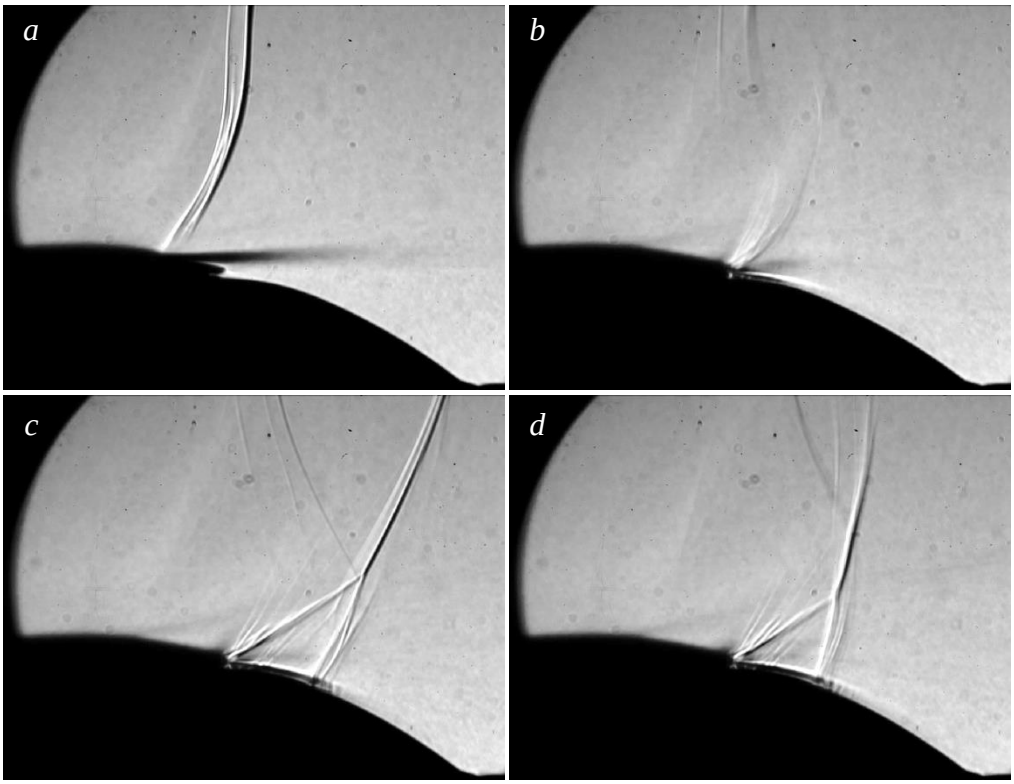

Figure 5.8 *Instantaneous schlieren visualizations of shock response to the onset of actuation for t/T_r = 3.3 (a), 7.9 (b), 14.6 (c), and 27.8 (d), for p_t/p_e = 1.35.*

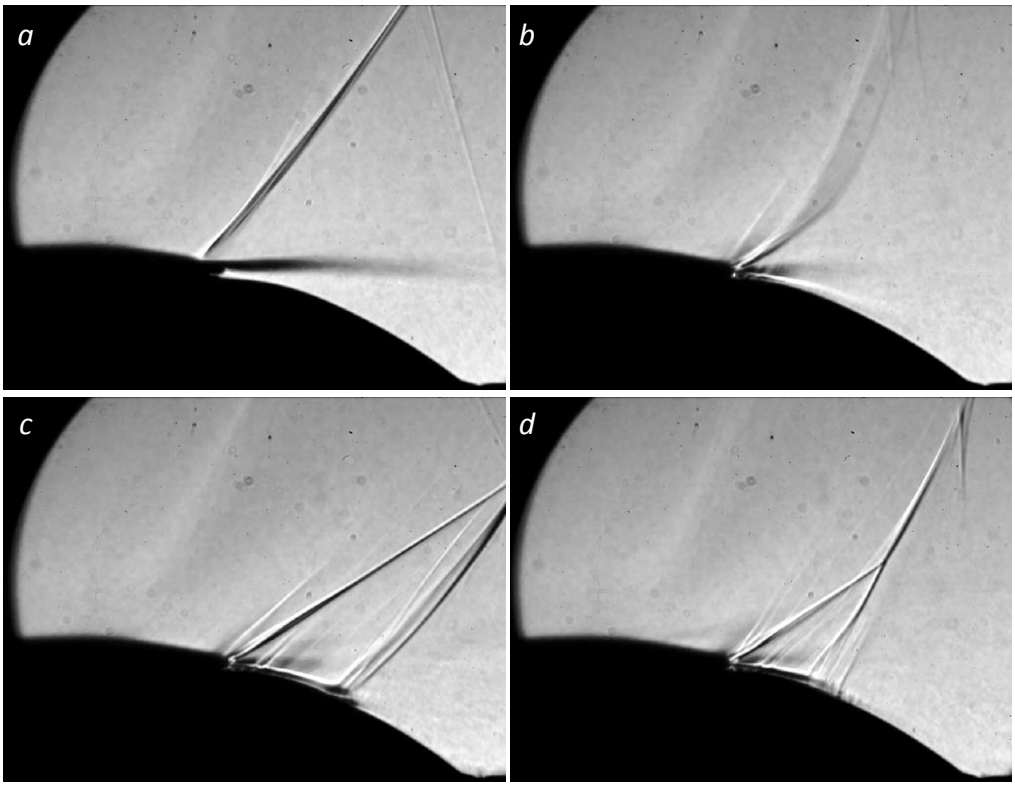

Figure 5.9 *Instantaneous schlieren visualizations of shock positions for t/T_r = 3.3(a), 6.6(b), 11.3(c), and 27.8(d) after the jet is triggered, for p_i/p_e = 1.4.*

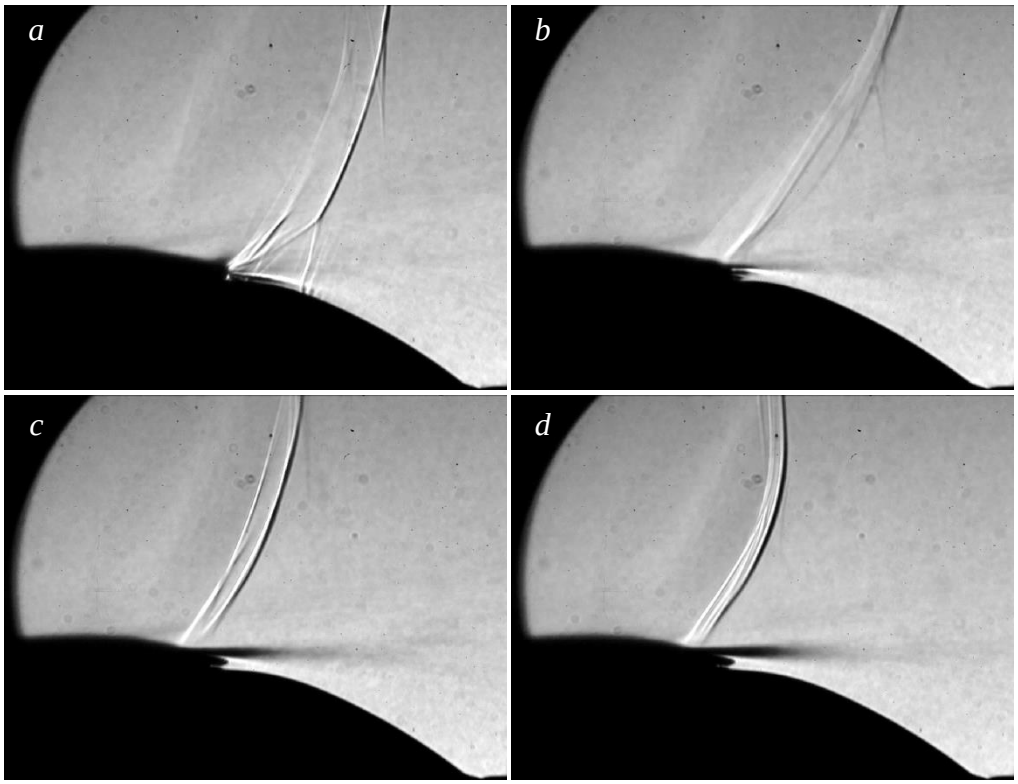

Figure 5.10 *Instantaneous schlieren visualizations of shock response to the termination of actuation, for t/T_r = 3.3(a), 7.9(b), 14.6(c), and 27.8(d) after the jet is commanded to switch to the off state, for p_i/p_e = 1.35.*

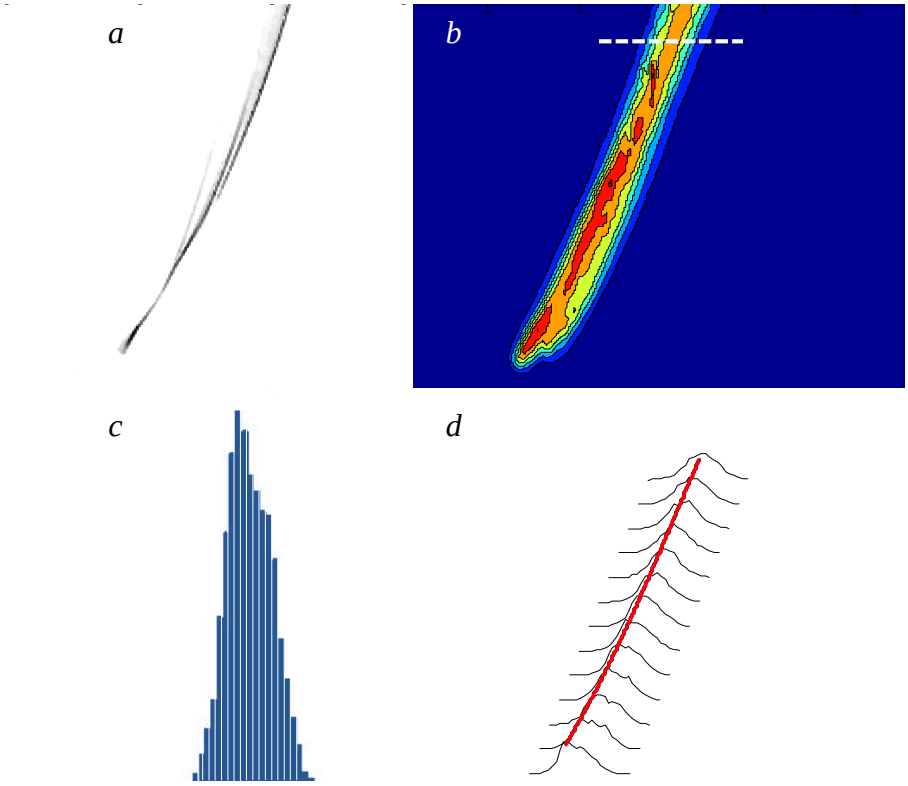

Figure 5.11*Summary of the analysis of the shock shape: (a) background subtraction for individual shock isolation, (b) superposition of all the shock positions at a given t/T_r (c) histogram of the shock positions at a given elevation marked and the maximum of each histogram marked by the solid red line in (d).*

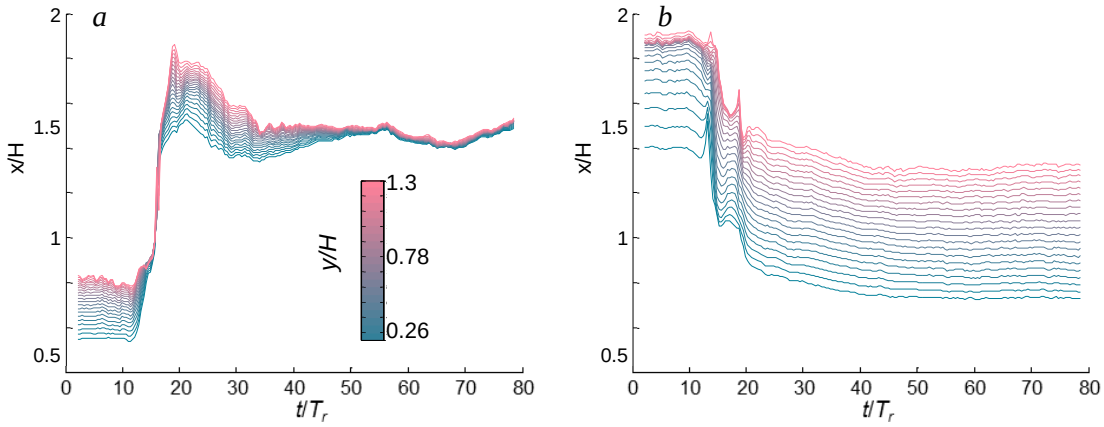

Figure 5.12 *Phase-averaged streamwise shock positions after the onset (a) and termination (b) of actuation at $t/T_r = 0$, for $p_i/p_e = 1.35$.*

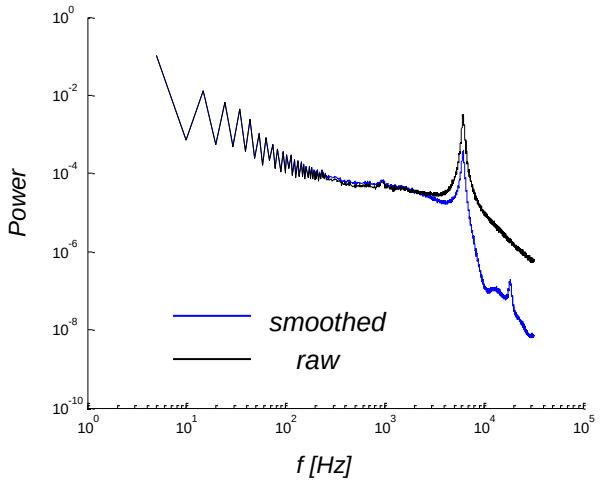

Figure 5.13 *Comparison of the power spectra for the raw vs. smoothed data for p_{d3} for p_i/p_e = 1.35.*

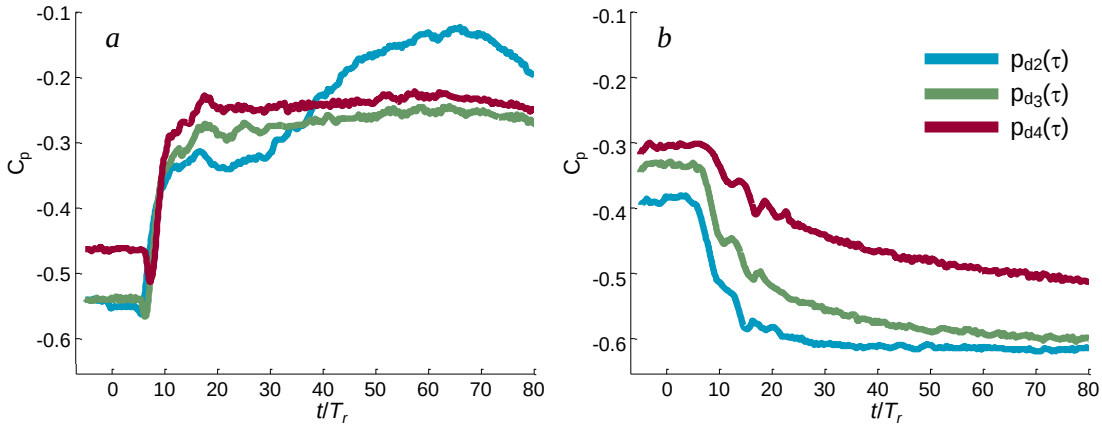

Figure 5.14 *Phase-averaged dynamic pressure evolution after the onset (a) and termination (b) of actuation at t = 0, for a p_i/p_e = 1.35.*

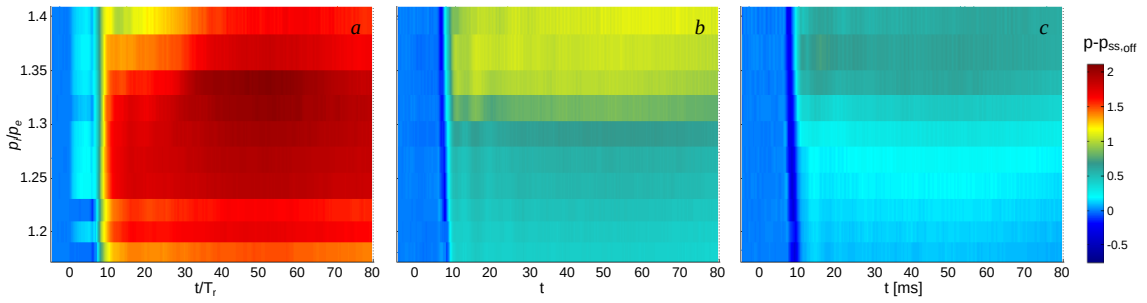

Figure 5.15 *Color raster plots of the phase-averaged dynamic pressures $p_{d2}(t)$ (a), $p_{d3}(t)$ (b) and $p_{d4}(t)$ (c) measured at x/H = 3, 4 and 5 respectively, evolution after the onset of actuation at t = 0, over a range of the pressure ratios p_i/p_e.*

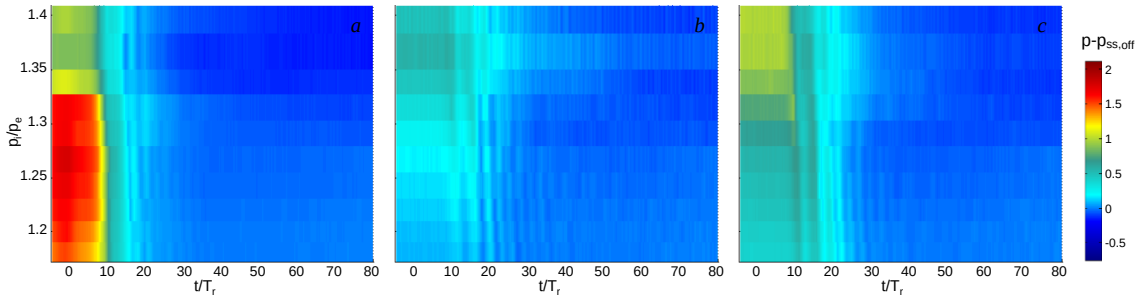

Figure 5.16 *Contour plots of the phase-averaged dynamic pressures $p_{d2}(t)$ (a), $p_{d3}(t)$ (b), and $p_{d4}(t)$ (c) evolution after the termination of actuation at t = 0, over a range of the pressure ratios p_i/p_e.*

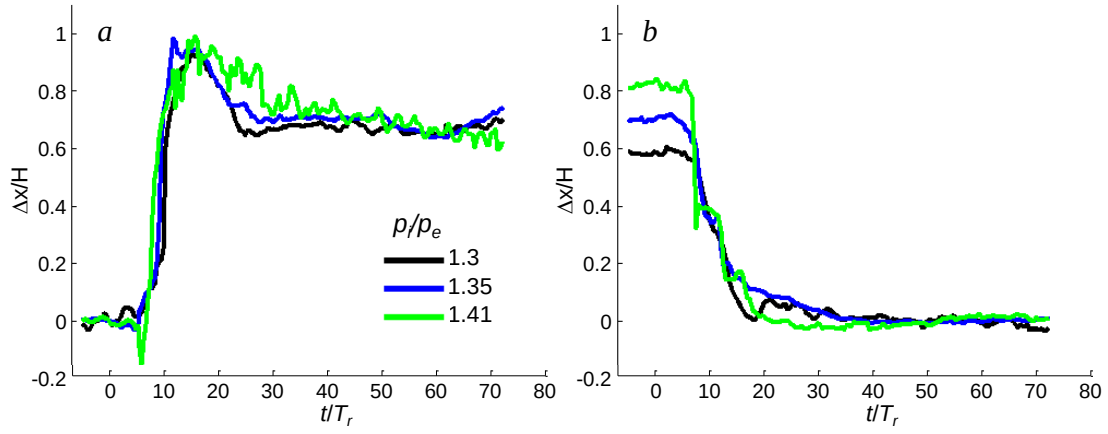

Figure 5.17 *Phase-averaged streamwise shock position at y/H = 1 after the onset (a) and termination (b) of actuation at t = 0, for the pressure ratios p_i/p_e = 1.3, 1.35, and 1.41.*

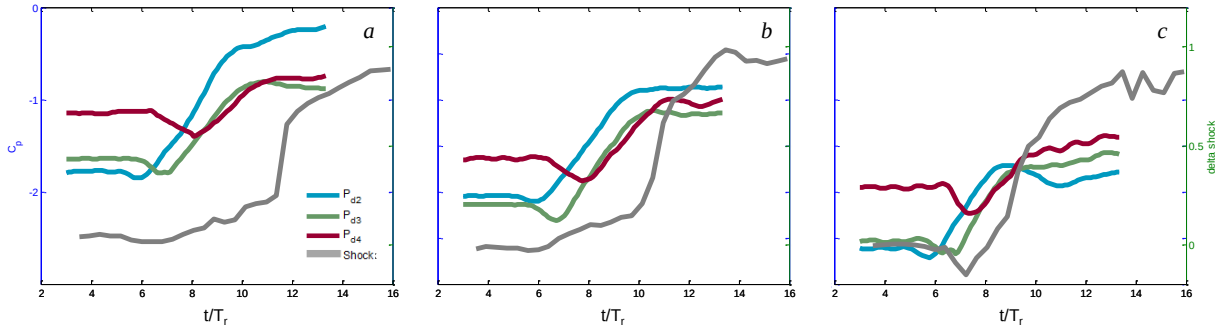

Figure 5.18 *Phase-averaged streamwise shock position at y/H = 1 and the three downstream pressures after the onset of actuation at t = 0, for the pressure ratios p_i/p_e = 1.3 (a), 1.35 (b), and 1.41 (c), respectively.*

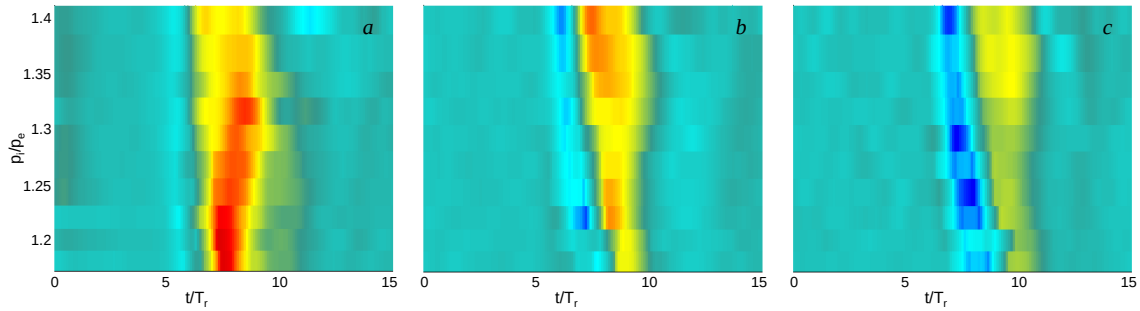

Figure 5.19 *Contour plots of the first derivative of the dynamic pressures $p_{d2}(t)$ (a), $p_{d3}(t)$ (b), and $p_{d4}(t)$ (c) after the termination of actuation at t = 0, over a range of pressure ratios p_i/p_e.*

CHAPTER 6

DYNAMIC EFFECTS OF REPETITIVE PULSED ACTUATION IN TRANSONIC FLOW CONTROL

6.1 Introduction

Following the investigation of the flow response to the onset and termination of single pulse actuation in Chapter 5, the present chapter focuses on the effects of repetitive (time-periodic) actuation using the pulsed jets with specific emphasis on the effects the actuation frequency on the coupled dynamics of the shock and the separating shear layer. In addition, this chapter investigates how these dynamics are affected by the pressure ratio across the test section, thereby elucidating the control authority of the actuation as the shock structure evolves with tunnel speed. Finally, the flow response, in terms of delay and hysteresis that are associated with pulsed actuation, is examined by comparison of the shock position to the speed of the flow control jets.

6.2 Pulse Jets

The pulsed jet actuator hardware and their characterization are described in Chapters 2 and 5. The operation of the jets in repetitive actuation was characterized over a range of frequencies ($100 < f < 900$ Hz) in the tunnel's test section in the absence of a cross flow. The jets were operated with a plenum pressure (50psi) such that $C_q \times 10^3 = 4.5$ for $p_i/p_e = 1.35$ when the jets are in the open configuration (cf. Figure 6.4).The jets are operated at a duty cycle of 50% and the jet speed was measured using a miniature hot wire sensor placed at the center of one of the jets in the array. Figure 6.1a shows the phase averaged (relative to the actuation waveform) jet speed for several operating frequencies over the normalized actuation period. The jet speed is normalized by the speed the jet reaches when it is fully open (U_{jo}). As shown in Chapter 5, the characteristic rise and fall time of the onset and termination of the actuation at the

operating pressure of the jets are 0.325ms and 26.9ms, respectively. Therefore, it is expected that the jet cannot attain its maximum speed as the actuation frequency increases above 400Hz. As shown in Chapter 5, when the jet is operating at a low repetition frequency, $f < 100$ Hz, there is a delay of approximately $t/T = 0.05$ before the jet flow commences, and the jet continues to increase towards its average speed followed by a slight overshoot, at about $t/T = 0.15$. The termination of the actuation lags the control signal and the jet speed begins to diminish at about $t/T = 0.54$. The time trace for $f = 200$Hz in (Figure 6.1) shows that the jet speed does not vanish at the end of the actuation cycle and reaches a level of $U/U_{jo} = 0.4$. As the repetition frequency is increased, the jet is not turned off, and the actuation is comprised of an offset continuous jet that is modulated at the actuation frequency. Figure 6.1a shows the amplitude and offset of the measured jet performance as a function of frequency. The offset is determined for each jet operating frequency by taking the minimum of the signal (cf. Figure 6.1a) and the maximum of the signal. Then, the offset can be computed by offset = min+(max-min)/2. The amplitude of the signal is simply max-min of the signal. There is an almost linear decrease in the amplitude of the jet strength with increasing frequency up to 400Hz with the amplitude of the jet strength dropping slowly as the frequency increases up to 900Hz. The offset, or the value about which the jet changes in velocity, asymptotically approaches 0.85 at 600Hz, with a slight decrease up to 900Hz. Based on these data, a jet operating frequency $f = 280$ Hz is selected as the nominal frequency at which the effects of the actuation are assessed in the remainder of the present chapter. The mass flow rate through the jet array is measured using an inline flow meter, and the mass flow coefficient is $C_q = 4.5 \times 10^{-3}$.

6.3 The Controlled Flow

The present active control approach builds on the previous work by Gissen et al. (2013), in which a transonic shock was indirectly manipulated by controlling the shock-induced

separated flow using fluidic oscillating jets. Such a control approach relies on the coupling between the shock, the incipient boundary layer separation, and the large-scale unsteadiness of the separated flow. Flow control can affect the separated flow and modify its dynamic and static (time average) properties, the altered pressure field couples to the shock to affect its static and dynamic characteristics. The present investigation utilizes this active flow control approach by implementing the pulsed jet actuators.

First, the overall global effect of this active flow control is assessed by analysis of the changes in the time-averaged flow field. This flow field was measured using PIV, recorded at 3,133Hz for 1 second, and represents the time average of these data. For more details on the PIV methods, see Chapter 2. Figure 6.2 shows the color raster plots of the time-averaged streamwise component of velocity at $p_i/p_e = 1.34$ for the base flow and in the presence of pulsed jet actuation at $f = 280$ Hz ($C_q = 2.8 \times 10^{-3}$). Although the unsteady shock structure becomes inevitably diffused in time-averaged flow field, it is still informative to assess the impact of the time-averaged shock on separation. The shock-induced separation in the base flow (Figure 6.2a) results in a nearly-horizontal shear layer that bounds a significant domain of separated flow downstream from the ramp. The recirculating flow is emphasized by the white contour of zero velocity. For more details on the base flow, see Chapter 3. In the presence of actuation, the separation point shifts downstream such that the root of the shock resides, on average, at $x/H = 1.6$, and the separated domain becomes suppressed as indicated by the reduction in area encircled by the zero contour level (highlighted in white). The shock (as indicated by the sharp gradients in streamwise velocity) responds to actuation-induced changes in the local pressure field and is displaced in the streamwise direction. It should be also noted that the shock slants in the downstream direction, similar to the effects seen in Figure 3.7.

To further quantify the changes in the shock that are effected by the actuation, the time-averaged shock and the RMS variations about this time average for $p_i/p_e = 1.34$ are shown in Figures 11a and b in the absence and presence of actuation ($f = 280$Hz, $C_q \times$

$10^3 = 0.0028$), respectively. These shock positions are extracted from the PIV using a method described in the Chapter 2. The shock structure, using continuous actuation at $C_q \times 10^{-3} = 1.7, 2.8$ for which the displacements are nearly the same as for actuation at $f = 280$ Hz, is also shown for reference in Figure 6.3b.

The traces of the RMS fluctuations in the shock position (Figure 6.3b) show that the steady jets affect the shock motion, increasing fluctuations predominantly at its root, i.e., close to the surface (up to $y/H = 0.8$) approaching the uncontrolled oscillations for elevations $y/H > 0.8$. Contrary to this, the pulsed jet increases shock RMS over the entire height measured. This points to significant flow control authority of the shock displacement by raising the RMS fluctuations. It should be emphasized that such large RMS values of the shock oscillation are the result of both the 'coherent', i.e., locked to the jet cycle, and 'incoherent', i.e., random, motions during the shock time-dependent displacement. It is, therefore, important to examine the flow response and the shock coupling phase-locked to the jet oscillation cycle.

The flow field, including the shock dynamics, is measured using PIV at forty equally-spaced phases during the actuation period of the pulsed jet. An illustration of the phase-resolved shock dynamics is shown using color raster plots of the streamwise velocity magnitude at six characteristic phases (Figures 6.4a-f). Just after the actuation signal is enabled (Figure 6.4a, $t/T = 0.02$), the flow is separated far upstream at the root of the shock at approximately $x/H = 1.25$, and the recirculation domain is captured within the field of view ($1.75 < x/H < 3$, $-0.5 < y/H < -0.1$). The shock root resides at $x/H = 1$, $y/H = 0.25$ and extends up to the edge of the field of view at $x/H = 2.25$, $y/H = 2$. Shortly afterwards (Figure 6.4b, $t/T = 0.17$), the shock still moves upstream, recovering from the previous cycle due to the inherent delay in the jet expulsion along with the flow separation (as the shock induces the separation). The jet velocity (Figure 6.1a) has a measureable delay following the jet trigger at $t/T = 0$, causing the shock to continue to move upstream at times following $t/T = 0$. Once the jet begins its rapid (step-response)

expulsion at $t/T \approx 0.15$, the flow attaches, which causes the shock to displace in the streamwise direction, as depicted in Figures 6.4c and d ($t/T = 0.29$, 0.39 respectively). It should be noted that the recirculating flow domain diminishes within the field of view of Figure 6.4d. This occurs because the shear layer is deflected downward when the cross flow becomes fully attached to the surface. The shock is slanted in the streamwise direction (compared to the jet off case) and accompanied by local reacceleration of the flow past the shock, as indicated by the region of higher speed flow near the shock root often referred to as the 'supersonic tongue' (which can be seen in Figure 6.4d, e and f). The flow stays in this configuration (similar shock position and shear layer location), as shown in Figure 6.4e ($t/T = 0.49$), due to a nominally constant jet speed during this period of the cycle. Finally, as the jet speed diminishes during the inactive part of the cycle (cf. Figure 6.1a), the flow attachment moves upstream and, as shown in Figure 6.4f ($t/T = 0.99$), the flow can be seen to separate from the surface (at $x/H \approx 2$), and the separation point and the shock move upstream concomitantly and continue their upstream motion into the next actuation cycle (e.g., Figures 6.4a and b).

The phase-averaged cross-stream distributions of the shock position and its RMS fluctuations are extracted from the realization ensembles at each of the 40 time increments during the oscillation cycle ($p_i/p_e = 1.34$) and are shown in Figure 6.5 (cf. Figure 6.3). The cross stream distributions of the base flow and when the actuations jets are continuously active (at $C_q = 0.0028$) are also shown for reference. The control authority of the pulsed jets is manifested by the variation of shock position during the actuation cycle where the total range of the shock motions (locked to the actuation cycle) is $\Delta x/H \approx 0.5$ (Figure 6.5a). As the actuation cycle begins, the shock is moving upstream as a result of the phase delay that is associated with the receptivity of the flow (marked by the arrow). But, at $t/T = 0.25$, the shock motion is reversed and it begins to move downstream beyond the average displacements effected by the equivalent continuous jet. As the shock reaches its farthest streamwise excursion ($t/T = 0.6$), it oscillates (with low

amplitude) about that position, until it begins to retreat towards the beginning of the next actuation cycle, as is seen in the cluster of shock realizations shown in grey at positions with *x/H* values greater than the shock position with an equivalent continuous jet (filled dots).Figure 6.5b shows a change in the RMS fluctuations about the phase-averaged positions which suggest that the level of RMS fluctuations is related to the direction of shock motion. The RMS fluctuations (as measured by x_{RMS}) are lower following the onset of the actuation, indicating that within each phase the flow control is placing the shock in a consistent location, 'overcoming' the turbulent fluctuations. The converse is true as the jets diminish in strength. This indicates that shock unsteadiness decreases during its streamwise displacement, which may be exploited for controlling the shock stability.

Phase-averaged time traces of the shock position (measured at $y/H = 1$), actuation jet speed, and pressure traces of the transducers downstream of the convex surface (p_{d_1}, p_{d_2}, and p_{d_3}) during the actuation cycle (f = 280 Hz, p_i/p_e = 1.34) are shown in Figure 6.6 (several instances during the actuation cycle are marked A–H). The time traces show that the shock position (or displacement) closely follows the evolution of the jet but with a pronounced phase delay that is affected by the timing of flow attachment and separation. It is noteworthy that the phase delay is shorter as the speed of the jet decreases following the decrease in jet speed at the termination of the actuation (t/T = 0.8). This change in phase delay may be attributed to the latency that is associated with the separation of the flow. It is instructive to consider the variation of the pressure downstream of the convex surface. The pressure measured by the upstream sensor, p_{d1},*is* invariant during the actuation cycle as the pressure sensor is upstream from the supersonic flow at the throat of the duct. The sensors p_{d2} and p_{d3}follow the variation in shock position (with increasing phase delays) where streamwise motion of the shock is normally associated with an increase in the pressure. As flow separation over the convex surface is diminished by the actuation, the flow accelerates over the surface and the pressure the downstream surface

increases. Conversely, when the flow separates, the pressure decreases and the shock is displaced upstream. Therefore, these data indicate that the shock dynamics can be inferred from the instantaneous pressure measurements, which may be used for closed-loop control of the shock position.

A sequence of schlieren images of the shock are captured during the instances A - H in Figure 6.6 during the actuation cycle and are shown in Figures 6.7a–h. As shown in Figure 6.5, the RMS variation in shock position during the actuation cycle is reflected in the instantaneous images of Figure 6.7. There are several features of the separating shear layer and associated shock dynamics that can be elucidated from these images and the corresponding dynamic pressure traces in Figure 6.7. The image at $t/T = 0$ (Figure 6.7a) does not correspond to the unactuated flow in Figure 6.2a. At the beginning of the actuation cycle (Figures 6.7a-c, t/T = 0, 0.125 and 0.25, respectively), the flow is separating from the surface and the shock is moving upstream, while the separating shear layer spreads in the cross stream direction and is diffused. At the next phase $t/T = 0.25$ (Figure 6.7c), the pulsed jet begins to form and, as the jet speed rises ($t/T = 0.375$, Figure 6.7d), the separated shear layer becomes attached (past the location of separation at the beginning of the cycle). This, in turn, decreases the pressure on the surface downstream of the shock and displaces the shock downstream as the surface curvature downstream from the shock allows expansion and acceleration of the flow (and thereby supersonic flow) further downstream, resulting in downstream displacement of the shock. The rapid shock displacement results in an uneven cross stream response as the shock segment closer to the surface responds faster to the changes in the pressure field, while its upper segment ($y/H > 0.8$) lags and develops an inflection point. At $t/T = 0.5$ (Figure 6.7e), the separation is further reduced and the shock is displaced farther downstream (nearly to the orifice of the actuator). It appears that, at this instance in the cycle, the shock root becomes locked to the actuator's orifice. However, as the attaching flow continues to deflect towards the curved surface, the shock begins to slant (or become oblique) and,

therefore, weakens and the flow becomes supersonic downstream of the shock. As this flow above the vectored shear layer speeds up, a normal shock is formed and induces lambda shock near the surface as shown in Figure 6.7e. The actuation jet is visible along the surface, but it appears that it does not fully attach the flow. The following two instances (Figures 6.7f and g, t/T = 0.625 and 0.75) depict the full effects of the actuation (the pulsed jet reaches it full speed while the separated flow reaches its maximum streamwise attachment). It is noteworthy that the jet is visible along the surface between the two legs of the lambda shock, indicating that the supersonic flow between the leading and the trailing shocks is fully attached. Finally, as the pulsed jet begins to weaken following the termination of the actuation, the flow begins to separate again (Figure 6.7h). This, in turn, weakens the lambda structure, and the shock begins to retreat to its initial state, before the beginning of the next actuation cycle.

The effects of increased frequency are examined through examination of the jet performance (Figure 6.2), as compared to the signal from the downstream dynamic sensor (p_{d2}). The maximums of both signals are found and the non-dimensional time (t/T) of those maximums are plotted for both signals and is shown in Figure 6.8. Examination of the two curves shown in Figure 6.8 indicates that there is a significant phase shift for increased frequency where, at higher frequencies (f > 700Hz), the phase lag is such that the peak occurs at times greater than the period of actuation (i.e. t/T> 1). This phase offset is contributed to the dynamics of the jet (as is seen by the increase in the curve associated with the jet strength), however, the divergence of these curves (with increased frequency) indicates that the frequency of actuation is approaching the maximum frequency at which the shock is able to change position.

The variation of the shock position with time during the actuation cycle is computed from the phase-locked PIV measurements of the flow field. The time-averaged shock over the entire actuation cycle is shown for reference in Figure 6.9a and is used to display colored elevation markers that are used with the phase-averaged information. Figure 6.9b is a

"waterfall" plot of the shock streamwise position during the actuation cycle such that each trace corresponds to a specific elevation relative to the surface (for an oblique shock, the streamwise spacing between the traces would be constant). The time traces correspond to 48 equally-spaced ($\delta y/H = 0.05$) cross stream elevations starting at $y/H = 0.5$. The colored traces in Figure 6.9b correspond to the color-marked elevations in Figure 6.9a, and the vertical dashed green and red lines mark the onset and termination of jet actuation, respectively. The phase-averaged variation of the shock streamwise position, with C_q at several elevations (y/H) during the actuation cycle, is shown in Figure 6.9c (time progresses in the counter-clockwise direction, and the shock position at each elevation is computed relative to its position at $t = 0$). C_q is derived from the jet strength which is measured via hot wire probe as shown in Figure 6.1a. The green and red dots correspond to the onset and termination of the actuation (cf., the dashed vertical lines in Figure 6.9b). As shown by the traces in Figure 6.9b, the response of the shock to the actuation is progressively delayed with increasing elevation. The same trend is shown more clearly in Figure 6.9c, where the traces are shifted upstream following the onset of actuation. As the jets' momentum increases, the shock moves rapidly downstream ($\Delta x/H = 0.6$, from $t/T = 0.2$ to 0.4), as is evident from the sharp rise in Figure 6.9b, starting at $t/T = 0.2$. The rate of change in the shock displacement varies across its height, as can be seen in Figure 6.9b, immediately following the vertical dashed line indicating the jet trigger, and in the non-overlapping lines in Figure 6.9c following the green dot in a counter-clockwise direction. The shock base ($y/H = 0.5$) begins to translate downstream before the rest of the shock. This is most clearly seen in Figure 6.9c where the base of the shock ($y/H = 0.75$) begins to move downstream (increasing x/H) while the jets are only at a strength of 0.5, whereas the rest of the shock ($y/H > 0.5$) does not begin to travel upstream until the jet strength has reached almost 0.6, in the case of the shock elevation $y/H = 1.8$. This is attributed to the changes in flow field along the surface imparted by the jets as they reattach the separated shear layer (cf. Figure 6.9d).

Following the rapid streamwise motion (the rate of which is a function of elevation and is the slope of the lines in Figure 6.9b from t/T = 0.2 to 0.4) of the shock as the actuation jet reaches its maximum speed (t/T = 0.35), the shock position remains virtually unchanged for $0.4 < t/T < 0.75$, and is also shown in Figure 6.9c by the clustering of points in the upper right hand region of the plot (C_q (t)/C_q = 0.9, $\Delta x/H$ = 0.6). During the relaxation of jet speed following termination of the actuation (vertical dashed red line in Figure 6.9b and red dot in Figure 6.9c), the shock moves back to its upstream position. The fact that the traces in Figure 6.9c are nominally linear back to the 'start' position (green dot) indicates that the shock is returning to its upstream position in a quasi-equilibrium manner. As previously discussed in Chapter 5, the rate of change of the strength of the jets following termination of the flow control is less than during onset. The trends indicated in Figure 6.9c indicate that this decreased rate of change of the strength of the flow control is not faster than the shock can respond.

The variation of shock position is examined at three pressure ratios (Figure 6.10) and is plotted in the same fashion as Figure 6.9b. These data exhibit two primary features with increasing pressure ratio. First, the cycle-averaged displacement of the shock for a given elevation increases (e.g., at y/H = 1, the cycle averaged displacement increases from 1.25 to 1.8 to 2.5). Second, for a given instance during the cycle, the displacement increases with elevation, as is evident by the spreading of the distance between the traces. (These changes indicate a significant change in the cross stream shape of the shock, as is also evident in Figure 3.7 that show that as the pressure ratio increases the shock translates farther downstream (higher x/H) and tilts in the streamwise direction (i.e., increase spacing between the traces in Figure 6.10).

Figure 6.10 also demonstrates that the delay between the motion of the shock relative to the onset of the actuation decreases with increasing pressure ratio. There are two reasons for this. First, as it moves downstream with increasing pressure ratio, the shock becomes

closer to the actuator jets, and, second, the speed of the cross flow increases, and with it the streamwise propagation of the effects of the actuation. Conversely, once the shock begins to travel downstream in response to the downstream boundary conditions (which are changed by the reattachment of the separated shear layer), there is a decrease in the rate at which the shock travels at higher pressure ratio, as indicated by the slope of the lines in Figures 6.10 a, b and c following triggering of the jets (vertical dashed green line). This is due to the fact that the changes in the downstream boundary condition must propagate upstream around the shock through air with increasing speed (for increasing pressure ratio across the test section). This results in a less rapid response, in terms of rate of change of the shock position, as can be seen in the slope of the lines in Figure 6.10a compared to the slope in Figure 6.10c.

Similar to Figure 6.9c, the corresponding variation of the shock position with $C_q(t)$ for the three pressure ratios of Figure 6.10a-c are shown in Figures 6.11a-c, respectively. These data accentuate the delay in shock motion between the onset of the actuation and beginning of the shock streamwise motion. These data show that the shock begins to move first closer to the surface (e.g., $0 < V/V_{max} < 0.5$) with a longer delay (e.g., $V/V_{max} = 0.75$ for 5.11a and $V/V_{max} = 0.6$ for 5.11b) and a slower response rate at elevations farther above the surface. As the jet reaches its maximum speed for all pressure ratios ($V/V_{max} = 0.9$), the shock continues to travel downstream, as indicated by the near vertical portion of the plot. The jet speed decreases following the termination of the actuation at $t/T = 0.81$, as indicated by the motion of the lines in the negative direction along the x-axis. At the lowest pressure ratio tested (Figure 6.10a), the shock moves further downstream after the jets reach their maximum velocity (cf. Figure 6.10a $\Delta x/H = 0$, $V/V_{max} = 0.9$ to $\Delta x/H = 0.75$, $V/V_{max} = 0.8$), compared to higher pressure ratios where the change in shock motion is only approximately half the distance for the same V/V_{max} range. This is due to the lag time, as the lag seen in Figure 6.10a, between the jet trigger and the downstream motion of the shock, allowing the jet to reach higher strength

before the shock begins to move. As the jets reach their nominally steady portion of the cycle (i.e., small variation in the x-axis), the shock stays in a fairly constant location in the upper right hand portion of the plot ($V/V_{max} = 0.8$, and $\Delta x/H = 0.5$-0.75). It is interesting to note that, similar to the response of the shock to step actuation in Chapter 5, the overall change in shock position is similar for the pressure ratios tested. For example, both the delay before downstream motion of the shock and the decreased rate of motion of the shock for increased pressure ratio can be clearly seen in Figure 6.18. After the decrease in the speed of the jets following the termination of the actuation (indicated by the red dots in Figures 6.11a-c), the shock translates back to its upstream position at $t/T = 0$. As the decrease in jet speed is less rapid (cf. Figure 6.1), compared to the increase in jet speed following the onset of the actuation, the shock is able to 'track' the velocity of the jet so that during the termination of the actuation the shock position does not lag compared to the time variation of the jet speed as indicated for all pressure ratios of the nominally monotonic and linear motion of the shock motion between the termination of the shock (red dot) and the start of the next cycle (green dot). This lack of hysteretic motion indicates that the rate at which the jets decrease in strength is less than the rate at which the shock could respond. This compares favorably to the finding in Chapter 5 for the step change actuation. However, the beginning of the cycle, where the jet strength increases, is much faster than that same timescale, indicating significant temporal and spatial control authority over the shock position. These results indicate that these flow control methods are able to change the downstream boundary conditions (shear layer shape) more rapidly than the shock moves for the onset of actuation but not for the termination of actuation (as was concluded in Chapter 5). The combined hysteretic effects of such a mismatch between onset and actuation, during repetitive actuation cycles, demonstrates that the fast response jets can respond to rapid changes in flow conditions *and* that the shock can be held at a downstream position with actuation

frequencies that have a period that is significantly less than the convective speed of the flow.

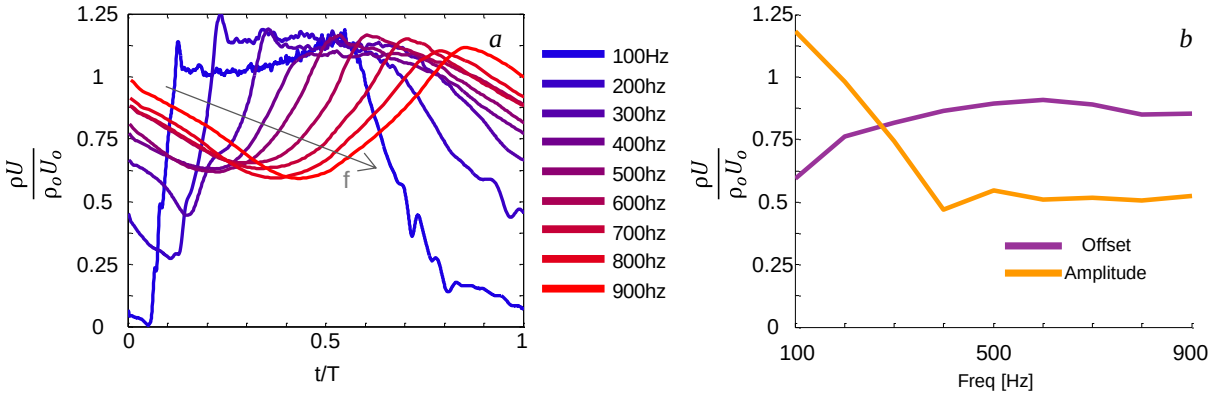

Figure 6.1.*Pulsed jet velocity distributions during the operation cycle at f = 100 – 900 Hz (a),(T is the period of the actuation trigger signal) the amplitude of the actuation and the offset about which the pulse jets operate as a function of frequency (b).*

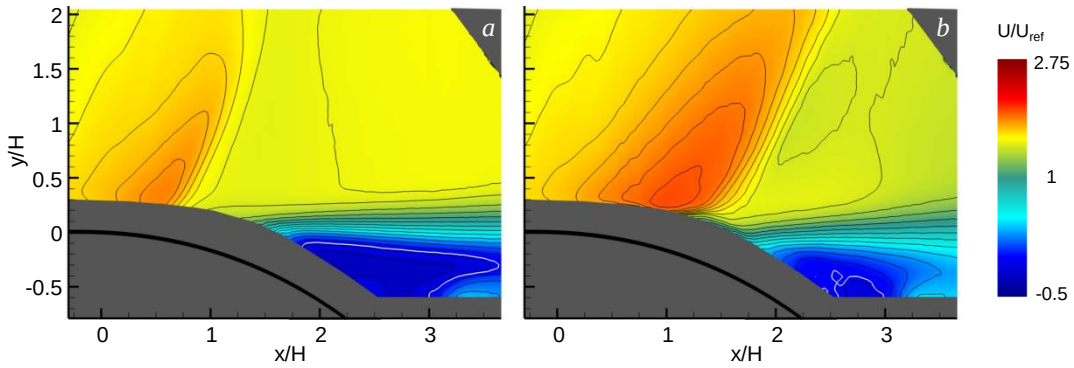

Figure 6.2 *Raster plot of the time average streamwise velocity component for the baseline flow (a, p_i/p_e = 1.34), and the flow controlled by the pulsed jets at f = 280 Hz and C_q = 0.0028 (b).*

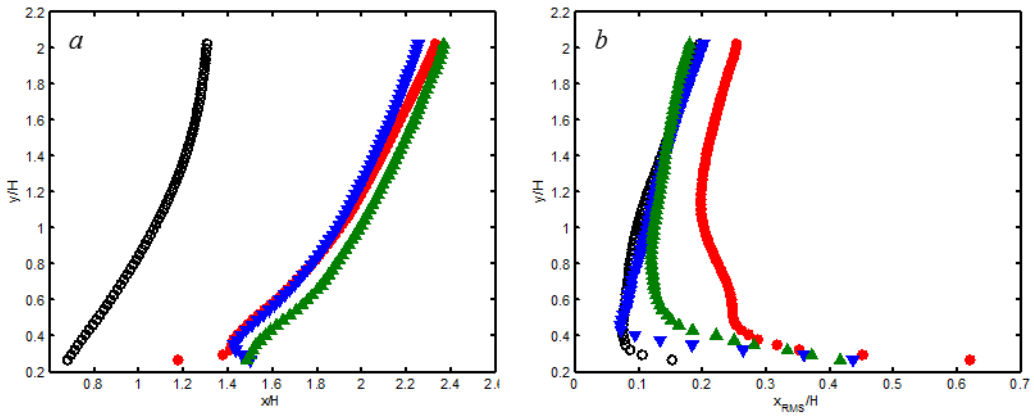

Figure 6.3 *Time average shock position (a) and the RMS of the shock position fluctuations (b) for the baseline flow (○, p_i/p_e = 1.34), and the flow controlled by steady jets at $C_q \times 10^3$ = 1.7 (▼), and 2.8 (▲), and by the pulsed jets at f = 280 Hz and C_q = 0.0028 (●).*

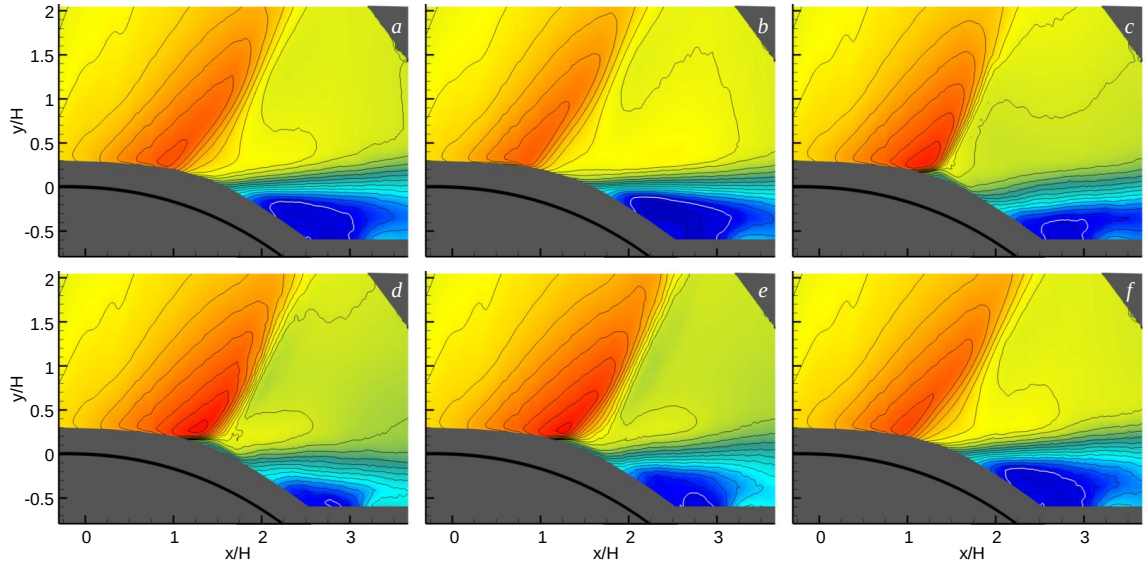

Figure 6.4 *Contour plots of the streamwise velocity component for the conditionally-sampled flow field at t/T = 0.02 (a), 0.17 (b), 0.29 (c), 0.39 (d), 0.49 (e), and 0.99 (f) during a single actuation cycle (f = 280 Hz and C_q = 0.0028). Contour levels are the same as Figure 5.2.*

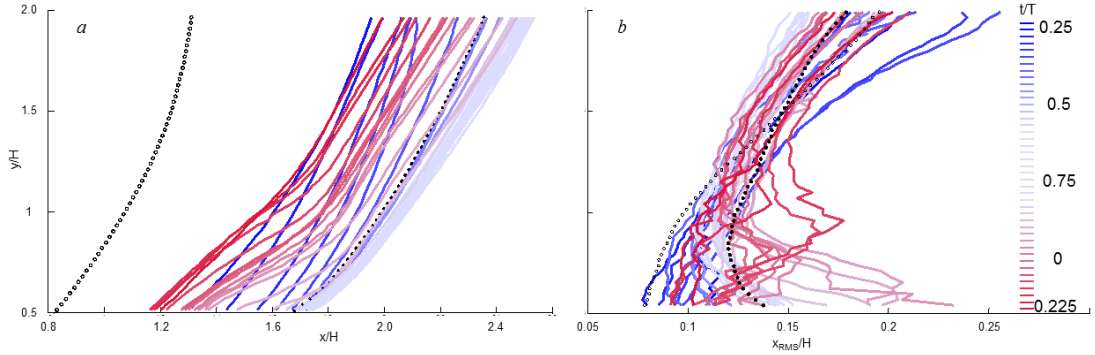

Figure 6.5 *Phase-averaged shock position (a) and the RMS of the shock position fluctuations (b) for the forty equidistant phases during the pulsed jet actuation cycle (f = 280 Hz, C_q = 0.0028). The corresponding mean and RMS profiles for the baseline flow (○, p_i/p_e = 1.34), and the flow controlled by continuous jets at C_q = 0.0028 (●)are shown for reference.*

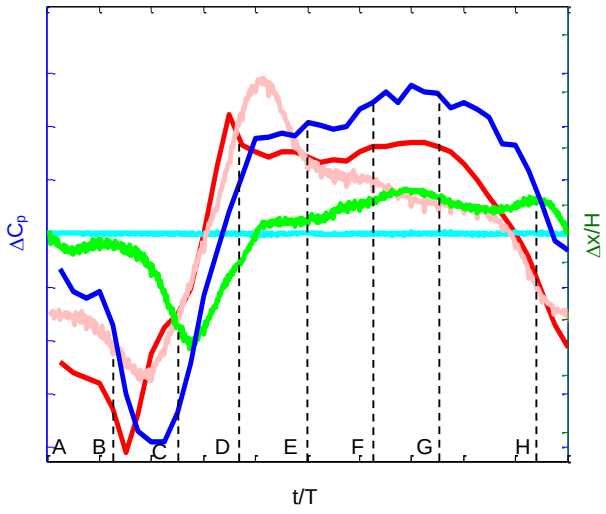

Figure 6.6 *Time traces of the pulsed jet velocity ( ), shock position ( ), and p_{d1} ( ), p_{d2} ( ), and p_{d3} ( ) pressure transducers during a single actuation cycle (f = 280 Hz, p_i/p_e = 1.34).*

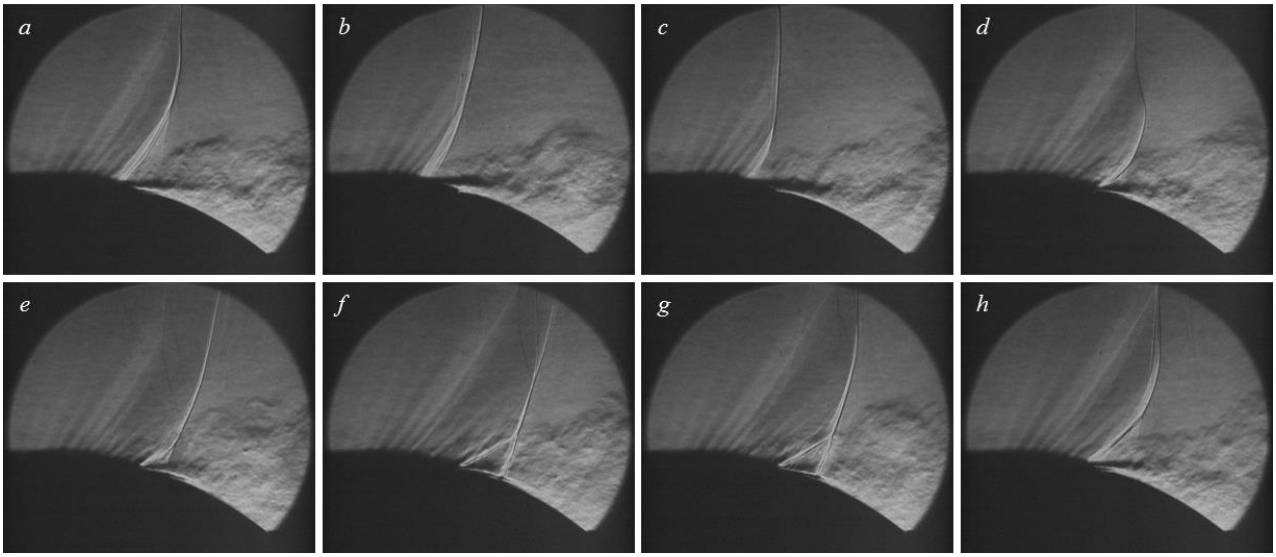

Figure 6.7 *Schlieren visualization of the transonic shock at p_i/p_e = 1.34 controlled by the pulsed jets at t/T = 0 (a), 0.125 (b), 0.25 (c), 0.375 (d), 0.5 (e), 0.625 (f), 0.75 (g), and 0.936 (h), phase of the actuation cycle (f = 280 Hz, C_q = 0.0028).*

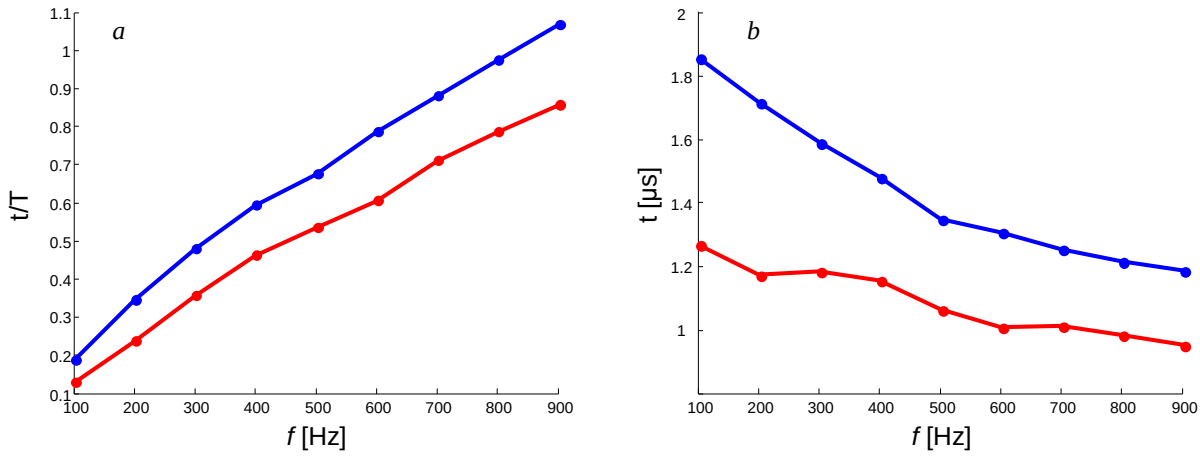

Figure 6.8 *The time at which the maximum value of the pressure sensor, p_{d2}, and the jet velocity, occur during the cycle as a function of frequency, both in terms of the non-dimensional time (a) and the dimensional time (b).*

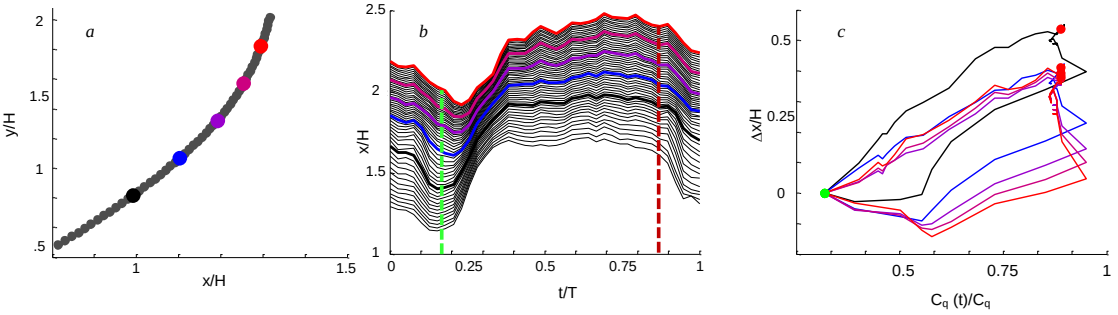

Figure 6.9 *The time average baseline shock profile at p_i/p_e = 1.34 (a), the 'waterfall' representation of phase-averaged shock displacement across its height, at C_q = 0.0028(b), and the shock relative displacement with the jet relative C_q (c). The onset and termination of the jet are shown in green and red dashed lines, respectively.*

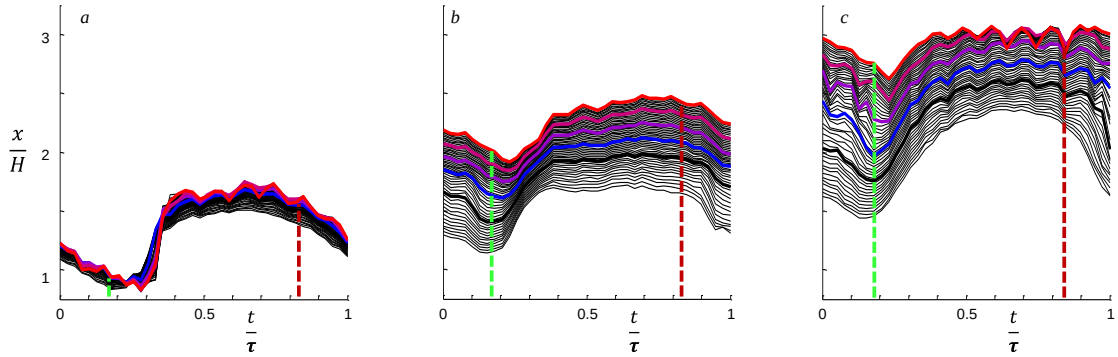

Figure 6.10 *The 'waterfall' representation of phase-averaged shock displacement across its height for p_i/p_e = 1.30 (a), p_i/p_e = 1.35 (b) and p_i/p_e = 1.39 (c), The onset and termination of the jet are shown in green and red dashed lines, respectively.*

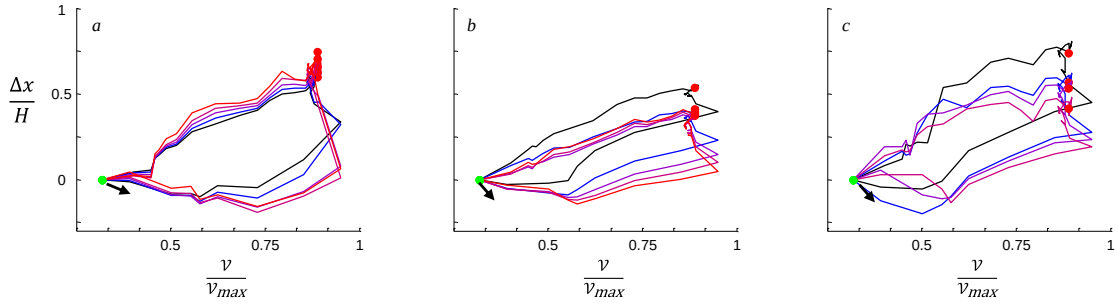

Figure 6.11 *The shock relative displacement with the jet relative C_q for p_i/p_e = 1.30 (a), p_i/p_e = 1.35 (b) and p_i/p_e = 1.39 (c). The onset and termination of the jet are shown in green and red dots, respectively.*

CHAPTER 7

FLOW CONTROL IN A CASCADE THRUST REVERSER

7.1 Background

Thrust reversers are integrated in aircraft jet engines with the objective of exploiting engine thrust to rapidly decelerate the aircraft for controlled, stable landings, especially in bad weather conditions when the runway can be wet or icy, and reducing reliance and wear on wheel brakes (Yetter 1995). Thrust reversers operate by directing part or all of the engine thrust forward using mechanical deflectors that are inserted in the stream of the exhaust jet. While there are a number of designs for thrust reversers, this chapter focuses on cascade type thrust reversers. For the aerodynamics associated with other designs please see a detailed study by Poland (1967).

A schematic of a typical cascade type thrust reverser in the deployed configuration is shown in Figure 7.1 (Butterfield 2006). Air entering the diffuser (A) is split such that a percentage of the air is ingested into the engine and is used for combustion and the rest bypasses the engine and is accelerated by a large fan (not shown). This bypass air then exits through a nozzle (B) and generates a significant portion of the overall thrust in turbofan engines under normal operating conditions. During deployment of a thrust reverser, this bypass air is caused to exit (C) at a vector that generates thrust in the reverse direction generated by the engine under normal operation. In order to efficiently direct air to the exit as shown (C), a series of operations take place. To begin with, a portion of the cowl (D) moves aft. This causes a blocker door to be deployed (E) which is designed to prevent the flow from exiting through the exit nozzle (B). In cascade type thrust reversers, the aft motion of the cowl (D) also exposes an array, or cascade of turning vanes, which the flow is forced to exit through. These turning vanes can be adjusted to generate various exit airflow vectors. A cascade type thrust reverser installed

on a turbojet powered fighter plane in a study by Kohl and Algranti (1957) demonstrated decreased stopping distances and reduced weight compared to the, then, standard design which did not include a cascade of turning vanes.

The design of a cascade type thrust reverser often deployed on Boeing commercial aircraft can be found in Wood and McCoy (1969), where the design for the 747 cascade type reverser is described in detail. Wood and McCoy describe the deployment, stowage and nacelle movement typical in a Boeing-designed reverser and, briefly, describe some of the advantages of this design. The interaction of the reversing flow with the wing, ground and body of the aircraft can often generate unexpected and dangerous situations, such as unpredictable variations in thrust magnitude and vector. A study addressing the issues of the interaction of the flow exiting the reversers with other aircraft components and the ground by Hegen and Kooi (2005) presents a very thorough investigation of two different types of thrust reversers integrated into a scaled model airframe. Other dangerous situations can arise when the vector of the thrust reverser exhaust can be such that re-ingestion of the exhaust flow is possible. This situation can result in severe engine surge and stall. A study performed by Dietrich and Gutierrez (1976) investigated the performance effects of airframe thrust reverser interaction with special focus on re-ingestion. A more modern example of re-ingestion was found on the C-17 where redesign of the thrust reverser assembly was necessary following several severe engine stall events (Johns2000).

Flow control efforts to improve the performance of thrust reversers have been the subject of a number of studies. A NASA contractor report by Arbiter examines the effects of rounding and rotating the surface over which the flow is turned (the bullnose, G in Figure 7.1). The flow through the duct was improved, but at the expense of very high rotation speeds. A patent by Smith (1977) details how a coanda jet installation in a cascadeless thrust reverser where the coanda jet is applied to the outside of the bullnose and, thereby, might be used to improve the performance of the duct. More recently a study by Hall et

al. demonstrated how flow control in the form of steady coanda jets applied to several locations within a natural blockage cascadeless thrust reverser can be used to improve the flow turning and overall generated thrust.

The large forces imparted on thrust reverser assemblies dictate the use of heavy components. One strategy for reducing the weight penalty associated with the installation of a thrust reverser involves the reduction in the overall length of the thrust reverser assembly. This strategy has two primary advantages. First, a reduction in the length of the thrust reverser would reduce the weight associated with the heavy components which constitute the thrust reverser assembly. Secondly, a reduction in the thrust reverser length would reduce the length of the nacelle. This reduction in length of the nacelle would reduce the wetted area of the nacelle thereby reducing the aircraft drag under cruise conditions.

The reason that such modifications have not been made to thrust reverser designs involves the efficiency with which the flow exits the thrust reverser. A shorter thrust reverser would necessitate a decrease in the radius of curvature over which the flow turns. This component, referred to colloquially as the 'bullnose', is shown in Figure 7.1 (G). Reduction in the bullnose length results in separation over the bullnose surface which generates losses. This, in turn, results in a reduction of the magnitude of the reverse thrust generated through a reduction in the mass flow rate through the duct due to increased drag. In addition, an increase in pressure drop across the thrust reverser assembly would place larger, and potentially damaging, load on the main engine fan.

For these reasons, it is the primary goal of this chapter to present a flow control strategy which reduces the separation over the bullnose generated by a reduction in length. It will be shown that the flow control developed in this chapter, which controls separation, increases the mass flow rate through the thrust reverser assembly. The results presented here demonstrate the feasibility of flow control installations for the mitigation of the adverse effects associated with reductions in thrust reverser assemblies.

7.2 Experimental Setup

A thrust reverser configuration that was developed for the purpose of the present experiments is shown schematically in Figures 7.2a and b. In this configuration, the blocker door of the thrust reverser (on the right hand side in Figure 7.2a) is fully deployed and the jet flow (from left to right) is forced to turn at a nominal angle of $45^{o}$and exit through the cascade vanes (at the bottom) that further vector the flow. The upstream jet flow turns around a "bullnose" corner at the bottom wall. The bullnose is of nominal height *H*, a parameter which will be used to scale the geometry where relevant. Owing to the strong turn, the flow typically separates at this surface thus significantly diminishing the effectiveness of the cascade vanes immediately downstream. It is also noteworthy that the thrust reverser section has an annular geometry, as shown in Figure 7.2b. The radial height of the test section at the apex of the bullnose ($x = 0$) is 4.2 *y/H*. The cascades span an axial distance of 5.1*H*.The facility is driven by a 66.3bhp blower that can deliver 3,907m^3/hr flow rate at 26.3kpa. The thrust reverser section is mounted in a high-speed open-return axisymmetric duct facility with a diameter of 11.5*H*. The thrust reverser duct is attached to this circular outlet section of the duct facility using an adapter section, filled with honeycomb and a mesh screen, in an effort to provide uniform flow to the thrust reverser section.

Particle image velocimetry (PIV) is made possible through a window installed in the upper surface, the area opposite the bullnose which corresponds to the inner nacelle, in order to provide for laser access. This window allows for a laser sheet to illuminate the flow over the surface of the bullnose. The PIV camera is located such that it has optical access through a plexiglass side panels and is able to prescribe angles to the laser sheet which makes the use of a scheimpflug unnecessary.

The shapes of the bullnoses are described in Figure 7.3. The bullnoses are of decreasing length with respect to the baseline (B) bullnose. Similarity in shape is preserved throughout the majority of the bullnose as demonstrated by the scaling factor of $L^{0.8}$.

This scaling of the shape indicates how quickly the curvature and thereby the pressure gradient scale with the length of the bullnose. The main purpose of this study is to determine how flow control can be used to alleviate the detrimental effects of reduced bullnose length. In order to accommodate these decreases in bullnose length, the blocker door (see Figure 7.2) and the cascades are moved in the axial (-*x*) direction. In this manner, the cascades, and thereby the exit area of the duct, are kept constant for all the bullnoses tested.

The flow control deployed in this study is fluidic oscillating jets. These jets are deployed at a constant x/H across the span of the bullnose in an array of 21 jets. The jets are integrated and faired into the surface in the same manner as the fluidic oscillating jets deployed in Chapter 4. The jets are deployed at an *x/H* location which is determined by a study of the separation (cf. Figure 7.7). For further details about fluidic oscillating jets please see Chapter 2.

Pressure measurements along the surface of the bullnose and on the pitot static probe are performed using the pressure scanner described in Chapter 2. The pitot static probe is located at the entrance of the test section at a distance of 6.5 *x/H*, upstream(-*x* direction) from the apex of the bullnose. The measurements from this upstream station are used to compute the inlet Mach number via the compressible Mach number calculations (Anderson 2003).

The pressure ratio across the test section is defined as the pressure that the facility vents to, atmospheric pressure, over the total pressure measured by the pitot static probe at the upstream station. This pressure ratio is controlled by adjusting the rpm of the blower motor in the wind tunnel facility.

Temperature is controlled in the facility via a sealed Aerofin heat exchanger, connected to the lab chilled water supply. The flow rate to the heat exchanger is controlled via a Johnson controls thermocouple-driven controller attached to a three-way bypass valve in the chiller water supply line. The control thermocouple is placed in the exit plume of the

facility. Thermocouples are also placed on either side of the heat exchanger and at the inlet of the wind tunnel. Temperatures are controlled to a repeatability of 1 degree F, thereby eliminating any corruption of data due to temperature effects.

The "baseline" bullnose geometry represents the current shape of bullnoses used in conventional thrust reversers (Figure 7.1). The variation of the time-averaged mass flow rate ($\dot{m}$) through the thrust reverser duct with the inlet Mach number (measured using a built in pitot static tube) and the pressure ratio (defined as ratio of the total pressure at the upstream end of the test section over the ambient atmospheric) P_o/P_{atm} are shown in Figures 7.4a and b, respectively. The Mach number is computed as described above, using compressible pitot probe formulas. The mass flow rate is measured via a NIST traceable mass flow meter situated at the inlet to the Georgia Institute of Technology's high speed duct facility. The data in Figures 7.4a and b were acquired during multiple entries over a long period of time (nine months) and indicate good repeatability. These data show a nearly linear dependence of $\dot{m}$ on *M* and that $\dot{m} \sim (P_i/P_{atm})^{2/5}$. Mass flow rate through the test section is a function of the pressure ratio across the test section. As the pressure ratio through the duct and the flow speed though the duct increase, the losses increase. The nonlinear aspect of this curve comes from the increased losses at higher speeds as the complex geometry of the duct generates regions of separation. However, unlike the similar curves shown in Chapter 3 (Figure 3.1), the facility does not reach a choking point. The highly curved surfaces do not result in the formation of supersonic flow across the entire test section for the inlet Mach numbers examined in these tests. The uniformity of the inlet flow to the test section was assessed from a cross-stream distribution of the Mach number (P_i/P_{atm} = 1.24) in the y-direction (Figure 7.5) that was measured by traversing a pitot-static tube normal to the surface at the midspan. The cross stream height of the section at this inlet station is 3.8*H*. The present measurements indicate that the thickness of the wall boundary layer is smaller than 3mm which is commensurate with the presence of a contraction upstream of the thrust reverser duct and

its adapter section. The data in Figure 7.5 indicate that the inlet flow is nominally-uniform in the y-ordinate direction at the pressure ratio of 1.24 ($P_i/P_{atm} = 1.24$).

7.3 Characterization of the Flow over the Bullnose Section

As discussed in §7.1, in order to reduce the nacelle length and thereby improve aircraft performance, it is desirable to reduce the length of the bullnose section so that both the length and weight of the thrust reverser can be decreased. However, a more aggressive turning of the flow can lead to stronger flow separation and with it an increase in the thrust reverser pressure drop, along with a reduction in the effectiveness of the cascade vanes (cf. Figure 7.1F). As discussed in §7.1, the goal of the present investigations is to assess the degree to which the bullnose length affects losses in the thrust reverser section, and then determine to what extent active separation control (Chapter 1, Active Flow Control) can be employed to restore flow attachment, and thus allow for the production of the same level of reverse thrust in reduced length thrust reversers. In addition to the base flow (conventional) bullnose (referred to as "B"), four shorter bullnose configurations (labeled A1-A4 where A4 has the most aggressive reduction in length) were constructed and tested. The shorter configurations were created by reducing the radius of the bullnose surface relative to the baseline 'B' geometry as described in Figure 7.3.

Static pressures on the surface of the bullnose, measured along the centerline of the baseline ("B") bullnose for a range of pressure ratios $1.04 < P_i/P_{atm} < 1.25$ are shown in Figure 7.6. The measurements are taken along the surface described in Figure 7.3. Due to the shape of the 'upper' surface of the duct, the flow is accelerating before it reaches the apex of the bullnose ($x = 0$). As the curved surface accelerates the flow, the pressure reaches its minimum value at about $x/H = 0.5$. The adverse pressure gradient associated with the expansion caused by the curved surface causes the fluid to decelerate, as indicated by an increase in the static pressure measured on the surface. This adverse

pressure gradient continues to slow the flow until, at approximately $x = 1.2$, the flow separates. This separation is indicated by a decrease in the pressure gradient measured along the surface, due to the fact that the pressure gradient on the surface is dominated by the free stream pressure in the separated region. As the pressure ratio (P_i/P_{atm}) and the flow speed increase, the minimum pressure decreases, but the location of the minimum pressure stays at nominally the same location. In contrast, the separation point moves further upstream for increasing pressure ratio across the test section, as indicated by the flattening of the pressure gradient observed over the three most downstream pressure ports.

Flow separation on the surface of the bullnose and on the upper surface of the thrust reverser test section in the presence of the base flow are shown in Figures 7.7a-c using surface oil visualization ($P_i/P_{atm} = 1.25$). Over the bullnose section (Figure 7.7b), the visualization shows flow separation as is evident by build-up of oil on the surface (marked by a dashed line). The oil buildup indicates that separation along the centerline occurs at $x/H = 1$. This is slightly upstream from where the change in slope of the pressure trace shown in Figure 7.6 would indicate that separation occurs. The slight curve in the line that indicates that separation is a weak function of the distance from the centerline of the facility owing to the effects of the sidewalls. This is evident by the curve in the oil traces over the bullnose. The curve in these traces increases with distance away from the centerline and is caused by the expansion of the corner vortex, which forms in the corner between the bullnose and the sidewall. The corner vortex brings higher speed flow down onto the bullnose surface, energizing the flow, which results in separation occurring further downstream for locations that are outboard from the centerline of the duct. It is postulated that this three dimensional effect is what causes the separation point to appear to be in different places, as indicated by the surface pressure and the oil flow visualization. Examination of Figure 7.7c indicates the flow pattern along the upper surface of the test section toward the blocker door (cf. Figure 7.1). The

window which allows for particle image velocimetry (PIV) to be performed is marked and has a minimal impact on the flow on the upper surface. There is a large separation region marked in a maroon dashed line near the base of the blocker door. This large separation region in the area where the blocker door and the upper surface intersect generates losses, reducing the mass flow rate and thereby the reverse thrust generated. While it is outside the scope of this thesis, this large separated region, which exists in this nominally ideal 'baseline' geometry, indicates that flow control designed to influence the size of this large region of separated flow has the potential to significantly improve the flow rate through the thrust reverser.

As the streamwise length of the bullnose is reduced, its radius of curvature decreases, causing the adverse streamwise pressure gradient over the surface of the bullnose to increase as shown by the distribution of static pressure along the bullnose centerline ($P_i/P_{atm} = 1.25$, Figure 7.8b). As the radius of curvature near the apex of the bullnose ($x = 0$) decreases, the minimum pressure decreases. This is analogous to the leading edge of an airfoil at increasing angles of attack. For an airfoil, the suction peak increases and moves up-chord for increasing angles of attack due to the effective increase in local radius of curvature with respect to the flow. In the same way, the low pressure region caused by the radius of the bullnose increases in strength and moves upstream for decreased radius of curvature. This is what causes the decrease in pressure upstream from $x = 0$, and why the minimum measured decreases as the bullnose number increases. The decreased radius of curvature also results in a stronger adverse pressure gradient downstream from the suction peak. The increased adverse pressure gradient results in migration of the separation point further upstream for decreased radius bullnoses.

7.4 Control of Flow Separation over the Bullnose

As shown in section 7.3, the reduction in bullnose length leads to an increase in overall losses and, therefore, a decrease in mass flow rate and a loss in reverse thrust. The

objective of the present investigations is to explore the utility of fluidic-based active separation control on the surface of the bullnose in order to improve the overall aerodynamic performance while using an aggressive bullnose configuration. In terms of comparison, it is desirable to maintain the same mass flow rate as in the baseline geometry, at the same pressure ratio. To this end, a spanwise array of fluidic oscillators is integrated in the bullnose so that the actuation jets oscillate in the spanwise direction and issue nominally tangentially to the bullnose's moldline (the actuation technology is described in detail in Chapter 2). A cartoon showing how these jets are embedded in the surface is shown in Figure 7.9a.The overhang shown in Figure 7.9a is used to direct the air exiting the jets along the surface of the bullnose. The streamwise location of the jet array for each bullnose configuration was determined by a separate investigation of the separation pattern using surface oil visualization (Figure 7.7, for example) and static pressure measurements (Figure 7.8b), so that the jets could be placed just downstream from separation, to ensure that in the absence of actuation the presence of the array does not lead to premature separation and increased losses. As was discussed, there was a disparity in the location of separation indicated by the oil flow visualization and the pressure measurements. As it was considered more 'conservative', the separation location was determined by the oil visualization along the centerline of the bullnose. The locations of the actuation jets on the bullnose configurations are shown in Figure 7.9 which indicates the trends in both separation location and in locations selected for the flow control installation. As the bullnose length decreases B-A4, the separation point moves upstream *and* takes up a larger percentage of the bullnose. A4, for example is separated over an estimated 77% of its length, whereas the B bullnose is only separated over 40% of its length. The flow control is placed downstream (in the positive x direction) from the separation point in an effort to have little influence on the flow when the jets are present but inactive. As is shown in Figure 7.9, the flow control is placed downstream from the point of separation. For the shorter bullnoses, physical constraints

dictated that the flow control was placed slightly farther downstream from the separation point. However, every effort was made to place them as close as possible to the separation point shown in Figure 7.9.

Although the integration of the jet array was designed to alter the surface geometry as little as possible, the presence of the array in the absence of actuation leads to some decrease in global mass flow rate. Figure 7.10a shows the variation with pressure ratio of $\dot{m}/\dot{m}_B$ for the bullnoses in the absence of the actuator array and in the presence of the inactive array (dashed and solid lines, respectively). When $\dot{m}/\dot{m}_B < 1$ for a particular pressure ratio, the mass flow rate is below that which would be attained under the same conditions for the baseline geometry without the installed actuator. The decrement in $\dot{m}/\dot{m}_B$ due to the installation of the actuators is the difference between the dashed and solid lines for a given bullnose configuration. For the longest (baseline) bullnose there is a maximum reduction of the flow rate to 96.5% at $P_i/P_{atm} = 1.03$ due to the presence of the actuator that monotonically decreases with increasing pressure ratio and reaches 99% at $P_i/P_{atm} = 1.2$, most likely due to the fact that a separated domain is generated by the presence of the jets at low pressure ratios, which is then overtaken by the natural separation at higher pressure ratios. As the bullnoses become shorter (i.e., more aggressive, bullnoses A1-A4), the losses in $\dot{m}/\dot{m}_B$ diminish with decreasing bullnose length. The outlier in this set of data is the A3 geometry where the location of the actuation array is observed to be non-optimal, as the decrease in mass flow rate does not follow the trend shown in the other four bullnoses investigated. The magnitude of the decrement in mass flow rate as a result of the integration of the flow control into the surface of the bullnose is a function of the difference between the optimal location of the flow control and the actual installed location. However, unlike A3, A4 shows almost no measureable decrease in mass flow rate at the highest pressure ratios in the presence of the actuation jets. This indicates that the actuator configuration for A3 could be

improved (through better actuation placement) beyond what is inferred from the pressure measurements.

The geometric scaling that was performed and described in Figure 7.3, is used as guide to scale the non-dimensionalized mass flow rates plotted in Figure 7.8a. Scaling of the curves results in the mass flow rates being proportional to $L^{-0.1}$, with $m^* = \left(\dot{m}/\dot{m}_B\right)(L_B/L)^{0.1}$. It is interesting to note that the behavior of A1 and A3 appear to be outliers in this trend. Furthermore, when the flow control is installed but not active, the behavior over the range of pressure ratios becomes similar for all bullnose lengths due to the fact that the separation is 'triggered' by the step of the jet installation, uniformly across the bullnose, whereas in the naturally occurring separation the flow separates span wise non-uniformly, setting up additional non-linearities in the losses generated through the duct. It is also notable that the behavior of A1 and A3 are very similar to the behavior of the baseline bullnose at low pressure ratios, as indicated in the nominally flat response at low pressure ratios. In contrast, the other bullnoses tested indicate that there is a slight local maximum in relative performance at a pressure ratio of 1.06. It is unclear to the author what is unique about these two geometries and is recommended for future study. Finally, it is pointed out that the similarity between these curves indicates that, despite the complexity of this duct flow, the dominant factor that drives the reduction in mass flow rate in this study is the reduction in bullnose length.

As an introduction to the behavior of the various geometries with the flow control active, the A2 geometry is selected to represent the ability of the flow control to increase the mass flow rate through the thrust reverser. The changes effected by jet actuation on the A2 configuration are shown in Figure 7.11. The mass flow rate to the fluidic oscillators, unless otherwise specified, is presented as the percentage of mass flow provided to the actuators compared to the flow through the facility at a P_i/P_{atm} = 1.25 with the baseline (B) bullnose installed. This mass flow rate is kept constant and the variation of mass flow

rate through the facility with pressure ratio is measured. Figure 7.9a demonstrates that the actuation leads to a large increase in mass flow rate through the facility over the entire range of pressure ratios tested. At low pressure ratios (P_i/P_{atm} = 1.03), the mass flow rate is increased to 1.015, and, at higher pressure ratios (P_i/P_{atm} = 1.24), the mass flow rate is increased from 0.95 to 0.995. This is a 4.5% improvement with approximately 1.3% mass flow rate supplied to the facility. The plot in Figure 7.11a is flooded to reinforce the fact that values that are larger than unity represent a mass flow rate that is larger than that which would be attained using the baseline bullnose at the same pressure ratio. Furthermore, the entire flooded region is available to the designer simply by changing the mass flow rate to the flow control jets. It is important to note that the mass fraction supplied to jets is not included in the magnitudes plotted in Figure 7.10a, due to the fact that the mass flow rate is measured at the inlet of the facility. However, the mass flow rate supplied to the jets exits the thrust reverser assembly through the vanes and provides additional reverse thrust, over and above the increases shown by the plots in this section. The reduction in recovered flow rate through the facility for a constant flow rate to the flow control jets with increased pressure ratio is due to the fact that the mass flow rate that drives the actuation jets is kept constant, whereas the mass flow rate through the test section increases. It is thought that the reduction of recovery for higher pressure ratios is in part due to a decrease in the mass fraction (jet mass flow rate over flow rate through facility) supplied to the jets. As it was shown that the separation point moves upstream for increasing pressure ratio (cf. Figure 7.6), the relative position of the jet array and the separation point cannot be ideal over all conditions tested and therefore also contributes to the falloff in recovery for higher pressure ratios. In general, the plot of mass flow rate, Figure 7.10a, demonstrates the feasibility of using flow control to improve the performance of a shortened thrust reverser, as it shows that the flow rate (and by extension the reverse thrust) can be recovered back up to (and in some cases above) the levels provided by the baseline geometry. It is this recovery which is what demonstrates

that the use of fluidic oscillating jets is a viable option for reducing the adverse effects of the reduction of the bullnose length.

The flow mechanisms affected by the fluidic actuation may be inferred from the changes in static pressure distributions on the surface of the bullnose. Figure 7.11b shows how the flow control lowers the pressure over the bullnose and moves the separation point further downstream. The fluidic oscillating jets inject a large number of small scale structures into the flow near the separation point. This, in concert with the momentum addition, accelerates the boundary layer and forestalls the onset of separation. The accelerated flow attaches to the Coanda surface, causing a low pressure region over this curved flow control insert (the bullnose). The low pressure region serves to further vector the flow back toward the surface and in a direction more conducive to efficient flow through the turning vanes. The fact that the flow control is able to exploit these effects is the dominant reason why such a small amount of flow applied to the jets (1.5%) is able to enact such large "global" changes throughout the duct, as reflected in the changes in mass flow rate (Figure 7.11a). The static pressure distribution on the upper surface (Figure 7.11c) indicates that even though there is a significant increase in mass flow rate through the duct and associated changes in pressure on the surface of the bullnose, the pressures on the opposite surface is virtually unchanged. As previously discussed, flow control applied to this surface should remain an option for further study, as there appears to be potential for flow control to reduce the losses associated with the flow in this area.

The corresponding data for the higher surface curvature on the A4 bullnose are shown in Figures 7.12a and b. Unlike A2, the small physical dimensions of A4 prevented the co-location of static pressure ports with the fluidic actuators, resulting in a gap in the pressure traces. Despite this, the changes in the slope of the pressure trace downstream from the minimum pressure area($x/H > 0.25$) upon actuation (Figure 7.12a) indicate that the flow is nominally attached when the flow control is activated. Furthermore, the fact

that the slope is monotonically increasing up to the end of the bullnose seems to indicate that the flow is reattached all the way to the end of the bullnose. The flow control is able to reattach the flow in this region despite the larger streamwise pressure gradient associated with the higher curvature of the A4 bullnose.

The effect of the flow control on the flow rate through the facility for the A4 bullnose is shown in Figure 7.12b. With the flow control active, the mass flow rate through the thrust reverser is increased across the pressure range tested. However, while the flow appears fully attached, the mass flow rate is not recovered to the same extent as was seen in Figure 7.11a for the longer A2 bullnose. For example, at higher pressure ratios (P_i/P_{atm} = 1.24), the A2 bullnose was able to recover to 0.995, whereas for the same pressure ratio (and mass flow rate supplied to the jets), the A4 bullnose recovers to 0.965. This is due in part to the larger adverse pressure gradient imposed with the sharper curvature of the A4 bullnose (cf. Figure 7.8a). In addition, it is postulated that the cascade array is not optimized for the flow vector generated by the attachment of the flow over the A4 bullnose. Attachment over the A4 bullnose causes a vectoring of the flow angle that is 'steeper' than what would be generated by attachment over the baseline 'B' bullnose. As there is no change in the cascade array to account for this 'steeper' angle in oncoming flow, this is one potential cause of losses. In addition, preliminary oil visualization experiments indicate that the span-wise non-uniform separation (originally pointed out in Figure 7.7 for the baseline bullnose) is exacerbated by the larger adverse pressure gradient. Acting in concert with both of these effects is the fact that a constant mass flow rate is supplied to the jets while the pressure ratio is changed, resulting in a decreased mass fraction supplied to the jets with increased pressure ratio. The low pressure needed to vector the flow field over the higher curvature of the A4 bullnose should be proportionally lower when compared to the A2 bullnose. Therefore it is thought that it would be possible to attain the same performance as the baseline, even at high pressure ratios, with higher flow rates to the jets. However, as this would impose

larger systems costs during installation (larger supply line tubing, higher parasitic losses to the aircraft etc) it was decided to use the 1.3% mass fraction (of the baseline bullnose at P_i/P_{atm} = 1.24) as an upper limit. The dependence and, therefore, the tradeoff, between mass flow rate to the jets and the recovered mass flow rate through the facility is examined in Figure 7.13.

The performance of flow control installed on the most aggressive geometry, A4, is shown in Figure 7.13 in terms of $\dot{m}/\dot{m}_B$ for a range of pressure ratios (the data in the absence of actuation are plotted using dashed lines). This data is shown for reference and contains the same curves displayed in Figure 7.8. The recovery of the flow through the facility upon activation of the jets at high pressure ratios (P_i/P_{atm} = 1.25) results in an increase in the flow rate through the facility of 2.5%. At low flow rates (P_i/P_{atm} = 1.06), the flow rate through the facility is recovered to levels 3% *higher* than the baseline. Due to the effects discussed in conjunction with Figure 7.12, all the curves corresponding to constant mass flow rate to the jet array exhibit a decrease in recovery of mass flow rate through the facility for increasing pressure ratio. The vertical offset in the curves with increased mass fraction supplied to the flow control array indicates the recovery as a function of mass flow rate to the jets (m_j) and the pressure ratio, this functional dependence is further examined in Figure 7.14b.

The offset of the recovered mass flow rate as a function of increased mass flow rate supplied to the jets is further examined in Figure 7.14b. The mass flow rate to the jets (m_j) is found to be directly proportional to the offset in the curves shown in Figure 7.13a and exponential related the pressure ratio by the function: $m^{\phi} = (\dot{m}/\dot{m}_B) - \kappa m_j (P_i/P_{atm})^{-6}$. The constant, k, is used to non-dimensionalize m_j and to linearly scale the offset parameters. The linear offset with increased actuation strength indicates that the flow control array has yet to 'saturate' and that further increases in mass flow provided to the jet array would generate similar increases in mass

flow rate through the facility. Small increases in flow rate to the jet array continue to further effect the global flow field in a manner that decreases losses through the duct for increasing actuation levels. The recovered mass flow rate was found to be a nonlinear function of pressure ratio for all actuation levels investigated. Some reasons for the exponential decrease in recovered mass flow rate with increased pressure ratio were discussed in reference to Figure 7.9. It should be pointed out that the shape of this curve is a reflection of the fact that the mass flow rate behaves differently than the baseline, as a horizontal line would be indicative of performance similar to the baseline. It is thought that, of the items discussed in relation to Figure 7.9 that contribute to the reduction in performance with increased pressure ratio, it is the reduction in mass fraction provided to the jet array with increasing pressure ratio (as each curve is a constant m_j) which is the dominant factor in the shape of the curves shown in Figure 7.14a.

Details of the flow over the A2 bullnose in the presence of jet actuation were investigated using fog visualization. The investigated domain (Figure 7.14a) extends from the jet actuator array upstream that is visible on the bullnose surface in Figures 6.10b and c. In the absence of actuation (Figure 7.10a), the fog images show a domain of flow separation that is marked by the low concentration of fog particles, since it includes recirculating flow of unseeded air. When the actuation is applied (Figure 7.10c), the flow appears completely attached to the surface of the bullnose, as indicated by the presence of fog near the surface.

The changes in the flow field induced by the actuation jets are measured using particle mage velocimetry (PIV). Figure 7.15a and b show color raster plots of velocity magnitude that are superposed with velocity vectors in the *x*-*y* plane along the centerline of the duct in the domain of $0 < x < 2H$, $-1H < y < 0.37H$. Due to surface reflections, it was not possible to resolve vectors near the surface (covered in blue). Comparison of Figure 7.11a and b indicates that the actuation leads to an increase in the flow speed by as much as 100% within the region in the vicinity of the bullnose. The spreading of the effect of

the jets is due in part to the Coanda effect. The jets are caused to 'stick' to the surface due to their proximity to the curved surface. As the flow that exits the jets moves along the surface, its high speed generates a low pressure region, which serves to vector the flow toward the surface of the bullnose. This, combined with the resulting curvature of the streamlines, results in a region of high speed, which influences a large portion of the flow within the duct. The vectoring of the flow is shown in Figure 7.15c in a sub-domain of the flow measurements. Comparison of the direction of the vectors indicates the flow is significantly vectored toward the cascades, especially in the region near the bullnose. This effect diminishes with distance away from the actuators, but vectors are significantly vectored a distance of H away from the actuators. The changes in direction and magnitude of the velocity in this region have a global effect on the flow, as has been indicated by the large increase in mass flow rate through the facility upon actuation of the jet array.

Up to this point, mass flow rate has been used as a predictor of the reverse thrust. In order to examine how the changes described above relate to the amount of reverse thrust generated, the magnitude and direction of the flow exiting the duct is examined with the A2 geometry. The flow exiting the thrust reverser test section through the cascades is measured using PIV and is shown in Figure 7.16 using color raster plots of the velocity magnitude in the x-y plane superposed with velocity vectors in the absence (a) and presence (b) of actuation. The field of view is directly downstream of the cascades, and the yellow marks indicate the location of the turning vanes within the cascades. The yellow line in the top left-hand corner of the image shows the outer surface of the bullnose in the present model. In the absence of actuation there is a domain of low-speed flow near the outer surface of the bullnose downstream of the cascade (Figure 7.16a) that is the result of the separated flow on the surface of the bullnose upstream of the cascade (cf. Figure 7.14). The separation on the bullnose substantially decreases the flow through the first two vanes (closest to the bullnose). Farther to the right, the flow downstream of

the vanes is characterized by streaks of high-magnitude velocity through the gaps between the vanes, that are interlaced with lower velocity streaks that correspond to the wakes of the vanes. When the actuation is applied (Figure 7.12b), the extent of the separation is significantly diminished, there is significant flow through the first two vanes, and the flow field is turned towards the bullnose. The reduced blockage associated with the collapse of the separated flow leads to an increase in the mass flow rate through the thrust reverser.

Reduction in bullnose length increases the losses through the duct reducing the flow rate though the test section for a given pressure ratio. These reductions in bullnose length also have the effect of increasing the local radius of curvature and thereby increasing the local pressure gradients, as was discussed in Figure 7.3.The effects of the actuation (at 1.3% of the flow rate through the baseline bullnose configuration (B) with a pressure ratio of P_i/P_{atm} = 1.25)on $\dot{m}/\dot{m}_B$ for a range of pressure ratios and bullnose geometries (B-A4) is depicted in Figure 7.17. In the presence of actuation, the performance of B and A1 is nearly identical, indicating that the actuation is sufficient to overcome the change in geometry of A1, and that the baseline geometry location of the jets is not as ideal for the baseline geometry as it might be for the A1 geometry. There is a distinct fall off in jet performance which follows both the pressure ratio increase and the decrease in bullnose length, with B and A1 being exceptions. Furthermore, the A4 geometry performs better at the lowest pressure ratios tested P_i/P_{atm} = 1.04. At these low pressure ratios, the jets are able to impart a larger vectoring of the flow. Due to this effect, the flow over the rest of the cascade is less disturbed by the previously separated flow over the bullnose, improving the flow through the entire facility. Further examination of the trends, both with pressure ratio and with bullnose length, is shown in Figure 7.17b.

As was the case with Figures 7.10 and 7.13, scaling factors are applied in order to examine trends in the data. The active flow control cases for the jets at 1.3% (of the baseline flow at P_i/P_{atm} = 1.25) are scaled by the factors that were determined to be

functions of both pressure ratio (P_i/P_{atm})and bullnose length (L). The scaling parameter also includes the mass flow rate to the jets (m_j) but, as that is the same for all cases shown here, it is a constant across all curves. These two scaling laws, first introduced in the discussion of Figure 7.10 and 7.13, are combined resulting in: $m^{\gamma} = \left((\dot{m}/\dot{m}_B) - \kappa m_j (P_i/P_{atm})^{1.8(L_B/L)^{1.6}}\right)(L_B/L)^{0.1}$. The functional dependence on the pressure ratio (P_i/P_{atm}) is different for each bullnose. The non-linearity in the curves shown in Figure 7.17a becomes more apparent for bullnoses that have higher curvature, due to the fact that the separation domain forms at lower pressure ratios and becomes larger (and generates more losses) at lower pressure ratios. For this reason, the more aggressive bullnose behavior, as a function of pressure ratio, exhibits itself as a non-linearity when scaled by the mass flow rate through the facility. This departure from monotonic linear behavior is a measurement of the ratio between the behavior of these more aggressive geometries with flow control and the baseline geometry (B). The exponential parameter which scales the (P_i/P_{atm}) was found to have a functional dependence on the bullnose length. The scaling constant, k, which is used to non-dimensionalize the mass flow rate and to provide a fit parameter, is the same for all of the curves presented *except* for A1 where it was multiplied by 1/65 to get the curve fit that is presented in Figure 7.17b. The behavior of the A4 geometry bullnose departs from the behavior of the others tested for the range of $1.06 < P_i/P_{atm} < 1.16$. It is thought that this departure is due to the high curvature of the A4 bullnose which, when used to vector the flow, provides non-optimal flow to the first row of cascade array. However, this is in contrast with the higher pressure ratios ($P_i/P_{atm} > 1.18$.), where the B and A1 bullnose provide almost identical performance, and A2, A3 and A4 all scale in a similar fashion. The differences in behavior between B and A1 and the rest of the bullnoses indicate that there is a significant difference in the way which flow control is affecting the flow in these two geometries. It is theorized that these differences are due in part to the ability of

these two geometries (B and A1) to provide almost ideal flow (vector angle) for the cascades nearest to the bullnose, as with more aggressive bullnoses this increased vectoring provides increased losses through the first cascade by 'over vectoring' the flow. This distinction between B and A1 and A2-A4 is further examined in Figure 7.18.

The family of bullnose shapes with active flow control at various levels are examined as a function of mass fraction to the jets ($\dot{m}_j/\dot{m}$).Examination of Figure 7.16 shows that A2, A3 and A4 all collapse down to a single curve, indicating that there is a strong linear dependence between the mass fraction supplied to the jets and the resulting improvement in mass flow rate through the facility. This trend is independent of geometry for the three most aggressive geometries. The fact that the flow rate through the facility is a stronger function of the mass fraction than it is of the geometry is very important to the design of the flow control installation. For example, if the mass flow rate supplied to the jets is a critical design constraint, it is possible to select the geometry which would provide the acceptable level of performance directly from this chart. The exception is the difference between the B and the A1 geometries and the more aggressive geometries (A2-A4). These different trends are due to the fact that the lower pressure gradient (due to the larger radius of curvature) allows for the flow to be reattached at lower supply rates to the flow control jets. As the mass fraction increases, the flow is attached over a greater portion of the bullnose, which is why, at higher mass fractions ($\dot{m}_j/\dot{m} > 0.02$), the geometries behave in a similar fashion whereas, at lower mass fractions, the flow is dominated by the separation inherent to the more aggressive geometries. Bullnose geometries more aggressive than the A1 geometry affect the flow rate throughout the duct in a step-wise, non-linear fashion, which indicates that there is some sort of 'tipping point' reached that merits further investigation. In general, Figure 7.18 illustrates that a particular mass fraction is needed in order to affect the flow through the duct in the same way and that this trend is almost independent of geometry. Furthermore, while the B and A1 geometries 'saturate' at around 1.03, the A4 geometry, for the same mass flow rate

supplied to the active flow control, is able to achieve mass flow ratio of 1.041. This is another indication that, for higher mass fractions to the AFC, the more aggressive geometries with active flow control have the potential to perform better than the baseline geometry.

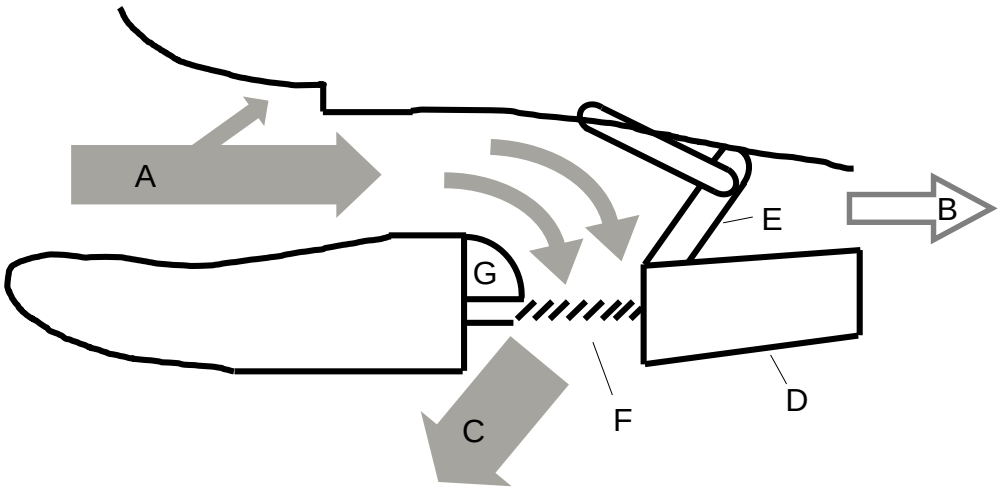

Figure 7.1 *Schematic of a typical cascade type thrust reverser (Butterfield 2006).*

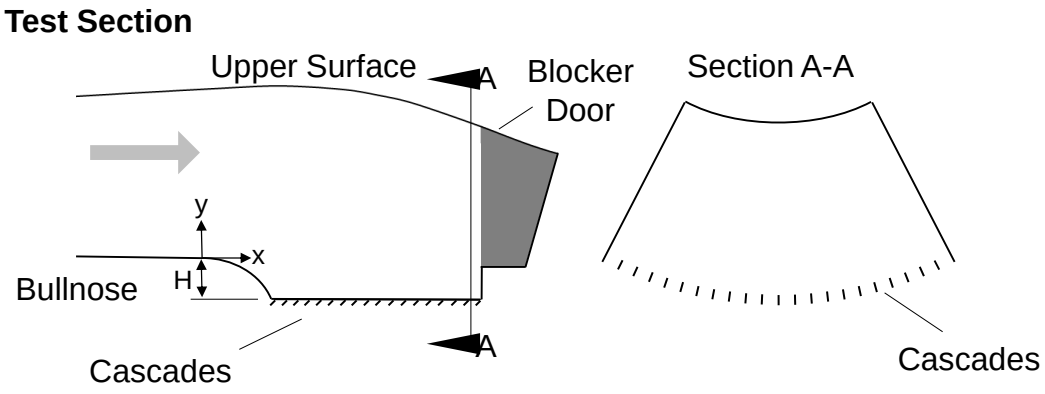

Figure 7.2 *Schematic of the thrust reverser test section; a) side view showing the main elements of the duct, and b) a cross section looking upstream showing the top and bottom curved surfaces of the annular sector.*

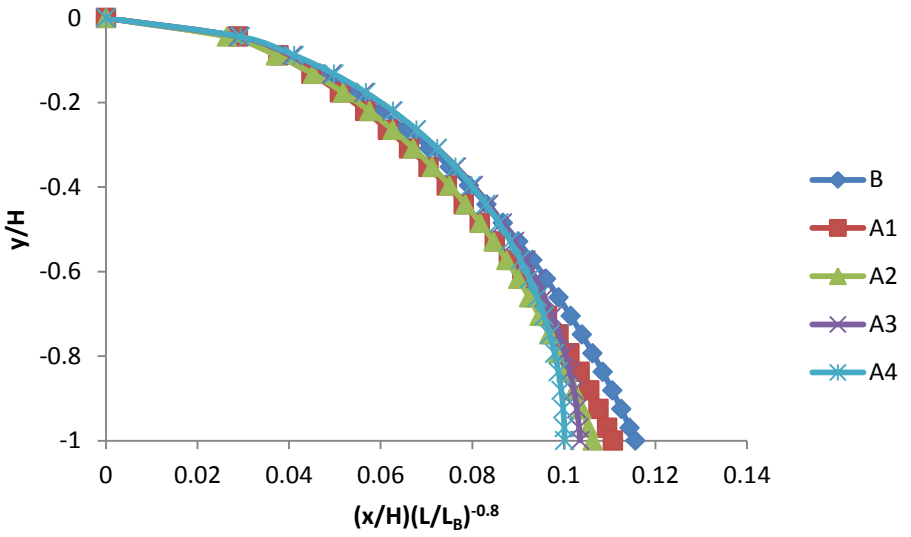

Figure 7.3 *Schematic indicating the self-similarity of the bullnose shapes. The length (L) of the bullnoses are [1.7, 1.4, 1.1, 1.0, 0.8] H for B, A1, A2, A3, A4 respectively. The shape of the bullnoses are plotted here with respect to L raised to the power of 0.8 to show the scaling of the bullnose shapes.*

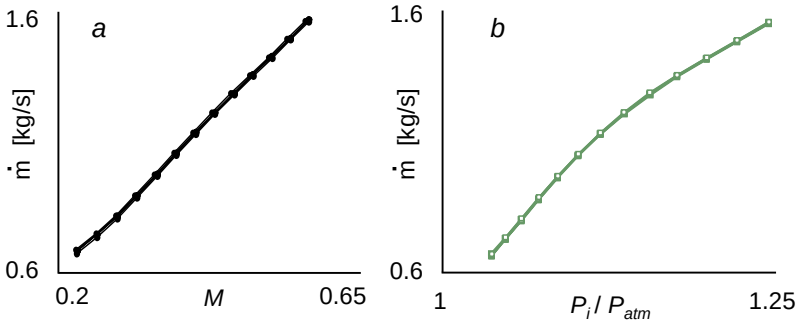

Figure 7.4 *Variation of the mass flow rate through the thrust reverser facility with Mach number (a) and with the pressure ratio (b), for the base flow. Multiple traces represent multiple data sets and indicate good repeatability.*

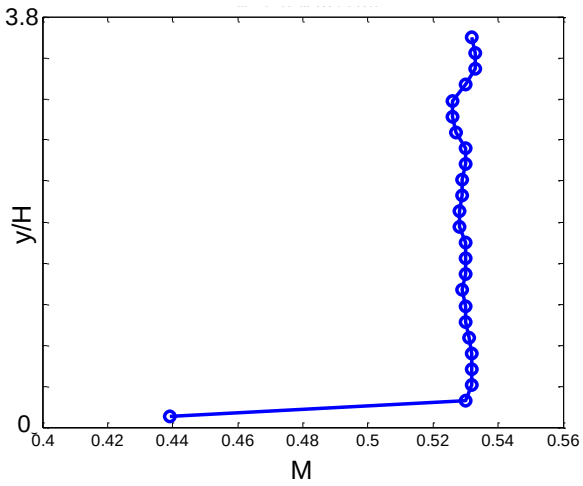

Figure 7.5 *Cross stream variation of the Mach number measured at the inlet of the thrust reverser tests section (x/H = -6.56) by traversing a pitot probe across the flow at* $P_i / P_{atm} = 1.24$*).*

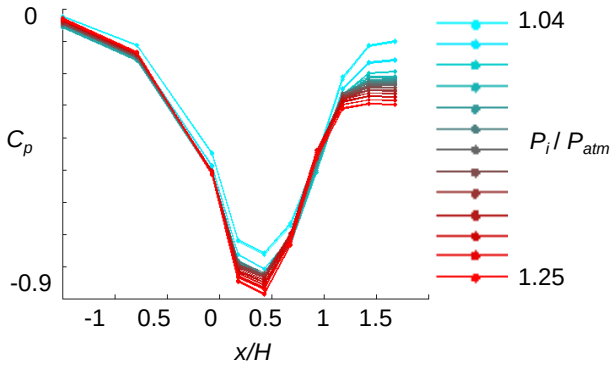

Figure 7.6 *Static pressure distribution along the centerline of the "baseline" bullnose over a range of pressure ratios* $1.04 < P_i / P_{atm} < 1.25$**.**

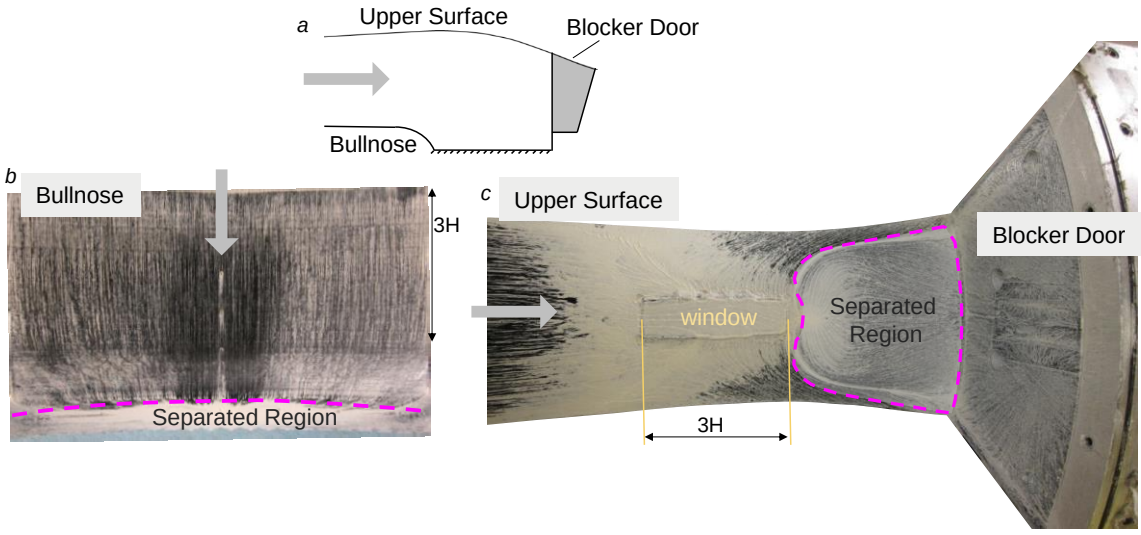

Figure 7.7 *Surface oil visualization at location indicated in (a) over the lower (bullnose, b) and upper (c)surfaces of the base flow.*

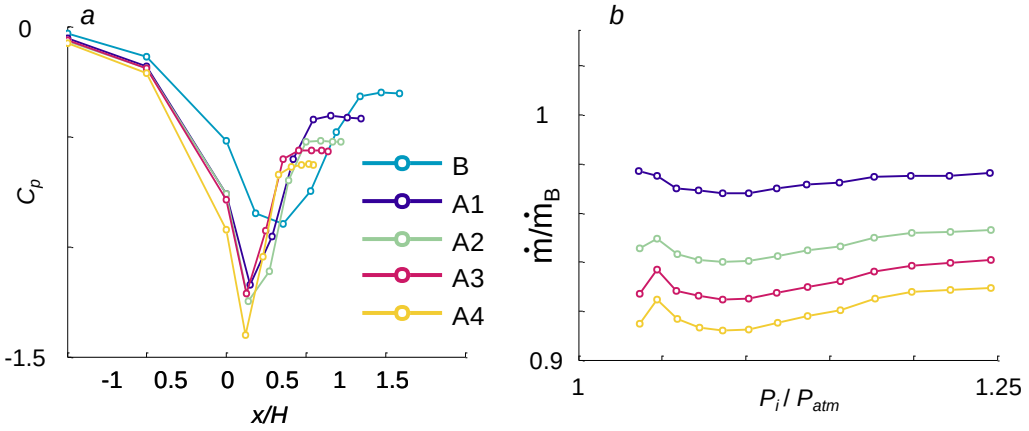

Figure 7.8 *The effects of reduction in bullnose length: a) Schematic diagram showing the relative lengths of several bullnose configurations of decreasing radius, b) Distributions of static pressure along the centerlines of these bullnose configurations for a P_i/P_{atm} = 1.25, and c)The variation of mass flow rate through the thrust reverser with global pressure ratio for the different bullnose shapes.*

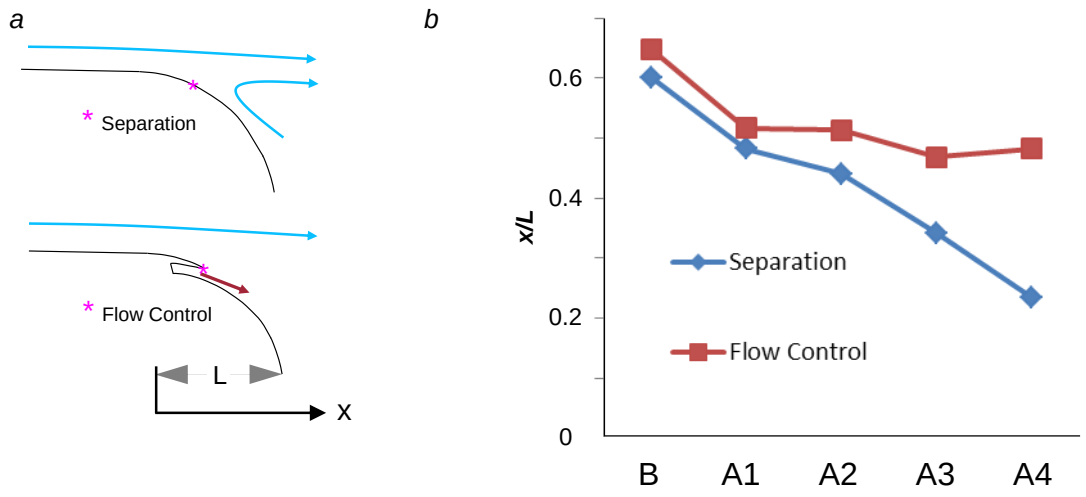

Figure 7.9 *A schematic of the bullnose and flow control overhang (a) Locations of measured separation and installed flow control overhang (b).*

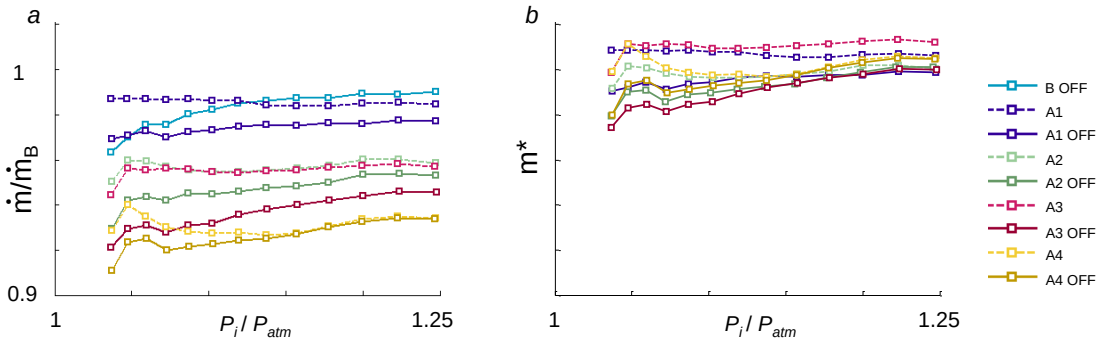

Figure 7.10 *Variation of mass flow rate with pressure ratio for five bullnose configurations in the absence (dashed lines) and presence (solid lines) of actuation with the actuation in an inactive state (OFF) (a), and the same values scaled as described in the text.*

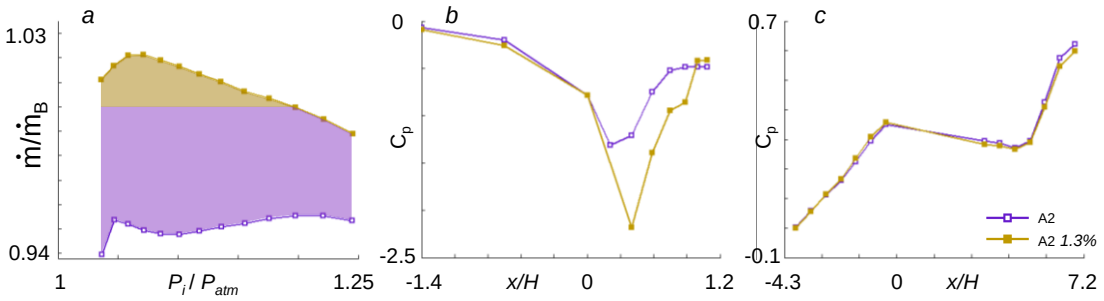

Figure 7.11 *The effects of the jet actuation on an A2 configuration: a) Variation of mass flow rate in the absence and presence of actuation. The range of mass flow rates 'recoverable' is indicated by the shading where the tan color indicates the region where the mass flow rate is recovered to levels better than the baseline (B) bullnose. The static pressure distributions (P_i/P_{atm} = 1.25) in the absence and presence of actuation on the bullnose (b), and on the duct's upper surface (c).*

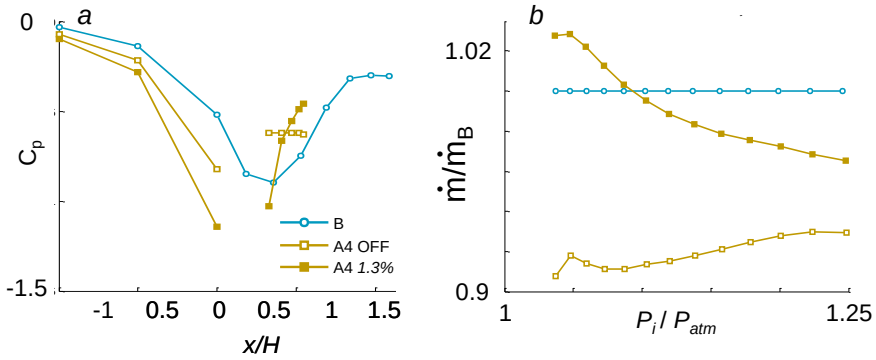

Figure 7.12 *a)Streamwise variation of the static pressure on A4 (P_i/P_{atm} = 1.25) in the absence and presence of actuation (the pressure distribution on B is included for reference), and b) Variation of the mass flow rate with P_i/P_{atm}.*

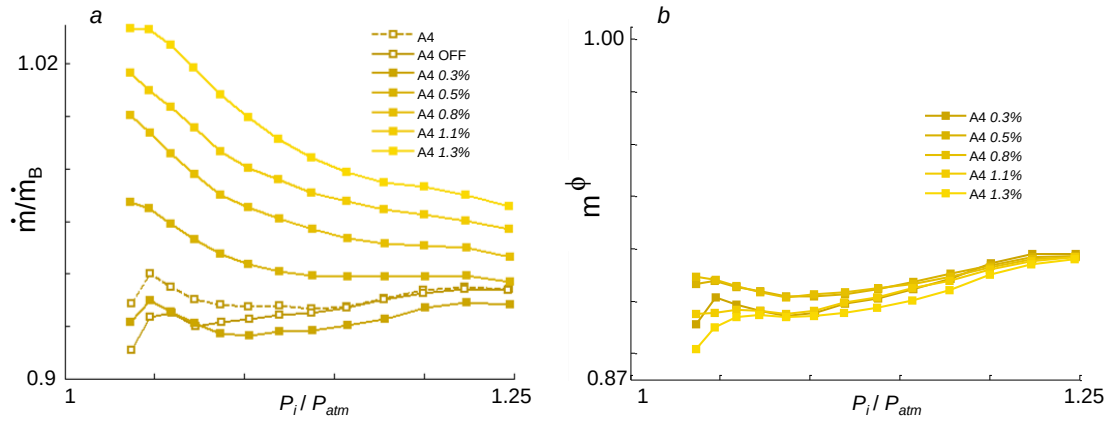

Figure 7.13 *Variation of the mass flow rate with P_i/P_{atm} for the A4 geometry, for a range of actuation magnitude (a). As with previous figures, the mass flow rate supplied to the jets is non-dimensionalized by the flow rate through the facility with the 'B' geometry at P_i/P_{atm} = 1.25. The offset in recovered mass flow rate through the test section due to increased mass flow rate to the jets (m_j) is found to be proportional to the m_j and inversely proportional to pressure ratio.*

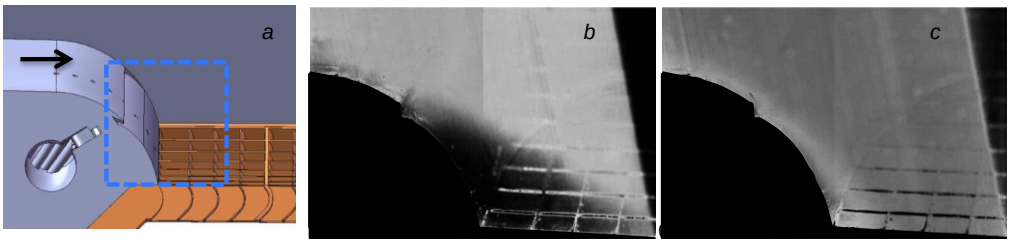

Figure 7.14 *Fog flow visualization near the A2 bullnose. a) A schematic drawing indicating the field of view for visualization (blue dashed line) and flow visualization in the absence (b) and presence (c) of actuation, showing the separated and attached flow, respectively.*

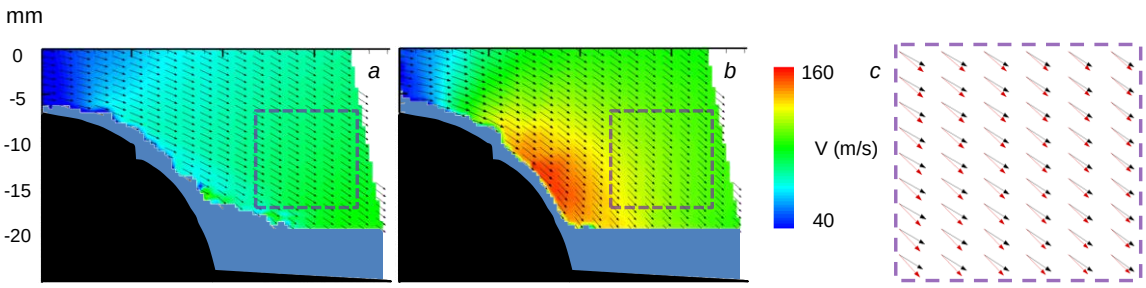

Figure 7.15 *PIV measurements in the cross stream (x-y) plane over the A2 bullnose: Color raster plots of the velocity magnitude superposed with velocity vectors in the absence (a) and presence (b) of jet. A smaller domain within the field (marked by a dashed box) shows velocity vectors from (a, in red) and (b) to illustrate the extent of flow vectoring.*

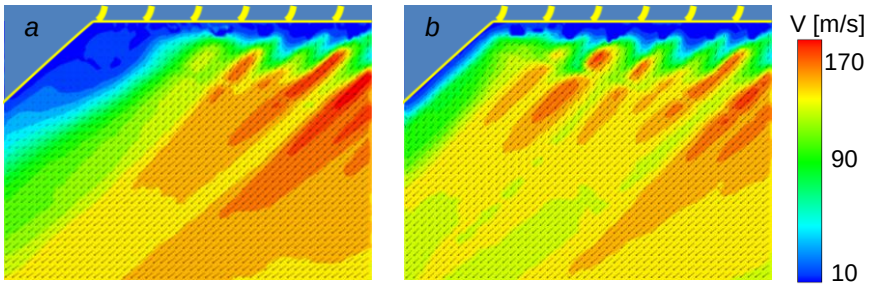

Figure 7.16 *Color raster plots of velocity magnitude superposed with velocity vectors in the cross stream x-y exit plane of the thrust reverser in the absence (a) and presence (b) of actuation. The yellow marks across the top mark the locations of the vanes.*

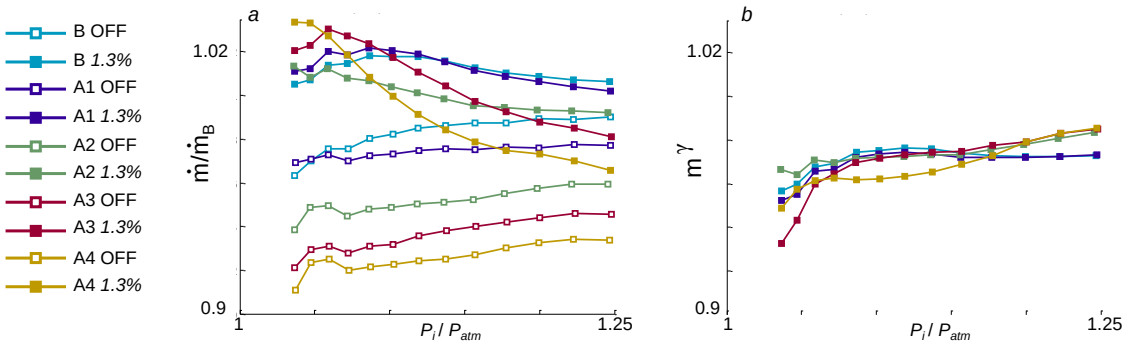

Figure 7.17 *Variation of the mass flow rate with P_i/P_{atm} for configurations B-A4 bullnose in the absence and presence of actuation (a), (b) shows the scaling parameters used to compare the performance of the flow control on the various bullnoses, note that C_1 is constant for all cases except the B geometry. Please see text for further details.*

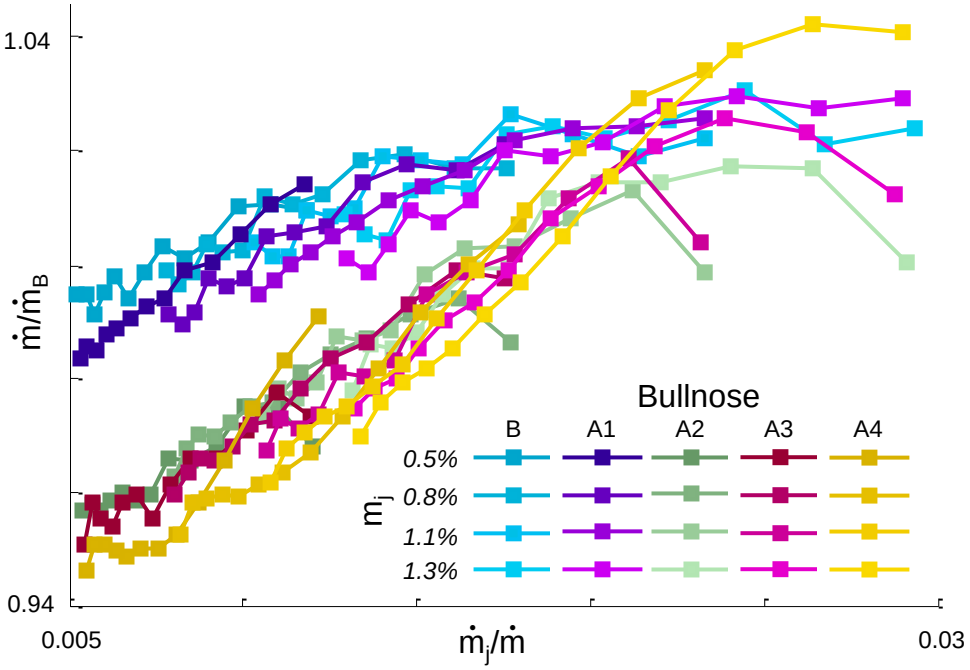

Figure 7.18 *The mass flow rate through the facility for the B-A4 bullnose geometry vs. the mass fraction supplied to the AFC.*

CHAPTER 8

HYBRID FLOW CONTROL IN A BOUNDARY LAYER INGESTING OFFSET DIFFUSER

8.1 Introduction

Chapter 8 builds on hybrid flow control methodology that was discussed in detail in Chapters 4-6 and explores its application to an offset diffuser.

Drag reductions resulting in improved aircraft efficiency may be attained in future Blended-Wing-Body aircraft (Liebeck 2004, Kawai, Friedman, and Serrano 2006) through the use of highly-integrated, boundary-layer-ingesting (BLI) inlets (Smith 1993) with embedded engines. However, the secondary flows (bilaterally symmetric swirling flow generated by an imbalance of centripetal forces), (Bansod and Bradshow 1972, Vakiliet. Al 1983, and Wellborn, Reichert, and Okiishi 1992), exacerbated through interactions with the ingested boundary layer, have an adverse effect on the total-pressure distortion and recovery at the engine face through the concentration of the ingested low speed flow in the bottom center quadrant of the AIP (Aerodynamic Interface Plane), (Anabtawi 1999), potentially resulting in undesirable engine performance caused by the circumferential imbalance of total pressure (Berrier and Allan 2004, Kurzke 2008).

The goal of the experimental work in the present investigations is to develop and investigate the effects of advanced flow control technologies for mitigation of pressure distortion that are primarily induced by the secondary flows within these complex offset inlet ducts in the absence of separation. This work is distinct from mitigation of flow distortion and recovery that are imposed by internal flow separation in aggressive offset diffusers (e.g., Amitay, Pitt, and Glezer 2002, Chiekh, Béra, and Sunyach 2003, Vaccaro et al. 2009).

The physically robust, passive flow control techniques that have been successfully applied to inlet systems to improve total-pressure distortion at the AIP (aerodynamic interface plane) (Kaldschmidt, Syltebo, and Ting 1974, Vakili et al. 1985, Anderson and Gibb 1993, Reichert and Wendt 1996, and Owens et al. 2008) inherently lack real-time adjustability of the structure and strength of the resulting flow patterns and, furthermore, incur a pressure-recovery penalty due to the energy extracted from the flow by the passive devices as they generate streamwise vorticity. Optimization and in-flight control of the performance of inlet ducts containing secondary flows, in the absence of flow separation over a broad flight envelope, can be achieved with active flow control. Steady blowing jets in various configurations have been shown to be effective in reducing the distortion at the AIP (Harrison 2013, Owens et al. 2008, Scribben et al 2004, Anderson et al. 2004,). Although it is predicted that active flow control has the potential for improving propulsion-system efficiency (through the ability to use submerged inlets) and operability in the Blended-Wing-Body aircraft (Dagget et al. 2003), deployment of active systems utilizing bleed air can be complex, not completely fail-safe (prone to power failure etc)and could require unacceptable amounts of parasitic engine bleed. A hybrid system which incorporates the strengths of both active and passive flow control strategies has been shown to be effective in the reduction of parasitic drag while maintaining fail-safe attributes (as passive devices do not require a power source to operate) and satisfying the need for adjustable flow control. There are a number of examples of these flow control strategies successfully controlling the flow in offset diffusers (eg. Owens et al. 2008, Anderson et al 2009). An approach that may have the potential to reduce engine bleed requirement was proposed by Harrison et al. (2013), who used an “ejector-pump” which combined suction of the upstream boundary layer with blowing to control the distortion in an offset diffuser.

By combining both passive and active flow control devices in a tandem configuration, the advantages of both flow control strategies can be realized. A hybrid actuation strategy

would be considered fail-safe (due to the passive flow control) and adjustable (through adjustments made to the active flow control). The selection of the active and passive components of the hybrid actuator employed in the present study is made with the goal of independently producing equivalent structures with individual components that can be combined in a manner that will cater to the strengths of both components. Vane type vortex generators have been extensively studied as a means for controlling separation in adverse pressure gradients(eg. Lin 2002, Godard and Stanislas 2006), alleviating the adverse effects of secondary flow in S-ducts (Tournier and Paduano 2005, Jirasek 2006, Anabtawi et. al 1999, Anderson et. al 2004) and as the passive component of hybrid flow control systems as in Owens (2008) where vane-type passive flow control devices were combined with steady blowing jets to reduce the distortion in an offset diffuser. In the present investigations, synthetic jets (Glezer and Amitay 2002) were selected as the active component of the flow control system since they eliminate the requirement for engine bleed and are relatively simple to manufacture and implement compared to potentially complex engine bleed systems, and have been demonstrated for mitigation of separation in low-speed duct flows (Amitay et al 2002, Chiekh et al, 2003). Gissen, Vukasinovic, and Glezer (2009) demonstrated that different configurations of synthetic jets can generate fluidic counterparts to passive sub-boundary layer vane type vortex generators in high subsonic flow over a 2D curved surface, which generated similar pressure gradients to that found in offset diffusers. It is interesting to note that numerical work on utilization of wall-bound streamwise vorticity for the flow separation control in a plane asymmetric diffuser (Törnblow and Johansson, 2007) was demonstrated by seeding the streamwise vorticity into the flow directly, thereby indicating that the source of streamwise vorticity (passive or active device) is unimportant. The effectiveness of hybrid actuation based on passive vane-type vortex generators, coupled with synthetic jet actuators, was demonstrated by Gissen et al. (2014) who showed that this hybrid flow control configuration produces favorable reductions in AIP distortion levels in an S-duct.

The necessity of using hybrid flow control for the engineering application described in this chapter stems from the particular end use of the research. In this case, the end use was intended to be on a commercial aircraft. For this reason, the system needed to be considered failsafe. The hybrid system benefited from the integration of passive devices by a reduction in the overall power required to run the system. In addition, the passive components were sized such that a failure in the active component would still allow for a margin of safety. While the concept of hybrid flow control is demonstrated in previous chapters, the components of the hybrid system appropriate for this specific application needed to be developed. The study which developed the passive and active components, with a specific focus on their interaction, is described in Gissen et al. 2009 and 2010. The application of hybrid flow control, demonstrated in chapter 3-5, is shown in the work presented below.

This chapter demonstrates viability of the hybrid flow control approach in a simulated boundary layer ingesting (BLI) offset diffuser in the absence of internal flow separation. It presents the nominally-steady effects of hybrid flow control on the diffuser's distortion and recovery, as well as the time-dependent aspects of the offset diffuser flow control using hybrid flow control aimed at mitigation of detrimental effects of secondary flows on the diffuser flow distortion through the introduction of streamwise vorticity with the opposite sense to that of the secondary flow. Dynamics of the active control-induced changes in the diffuser flow field are examined with respect to the resulting, time-dependent downstream changes in the AIP distortion.

8.2 Experimental Setup and Diagnostic Procedures

The present experiments are performed in a small, open-return pull-down, high-speed subsonic wind tunnel (test sections speeds of up to M = 0.75) and driven by a 150 HP blower, where the temperature of the return air is controlled using an external chiller, coupled with a low pressure drop heat exchanger. The tunnel is designed for installation

of a range of removable test sections between the inlet contraction exit (contraction ratio of 207, exit measures (12.3 x 12.3 cm) and the inlet of a downstream diffuser duct. In the present investigations, a scale S-duct model (based on a 5% BWB diffuser mold-line provided by Boeing) is installed using an inlet transition section (labeled as *diffuser adapter* in Figure 8.1) downstream of the contraction. The S-duct model has a D-shaped cross section H = 8.9cmand is 16.9cm wide at the 'inlet' or start of the s-duct section (x/D = 0). The S-duct model is 44.6cm long and ends at an aerodynamic interface plane (AIP) model having diameter, D_{AIP} = 12.7cm. The inlet transition section between the diffuser and the tunnel's contraction is equipped with a fence insert that is designed to mimic the effect of boundary layer ingestion at the blended inlet by thickening the incoming boundary layer. This insert is described in more detail in section 8.3.A removable surface segment within the bottom surface of the diffuser (beginning at x/D = -12.6, and spanning 15.2cm), is used for incorporating the flow control actuators on a removable SLA insert. The hybrid actuators developed for the experiments in this chapter are presented in detail in section 8.4.

Diagnostics include cross stream distributions of the streamwise velocity and are measured using hot wire anemometry upstream of the diffuser (z/H = -0.7)inlet within the domain $0 < y/H < 0.5$ at three spanwise positions z/H = -0.5, 0, and 0.5 (these measurements are shown in Figure 8.4). The hot wire sensor is traversed using a velmex controlled high resolution stepper motor attached to a screw driven linear stage. The distortion at the AIP in the diffuser flow is measured by a rake of 40total pressure tubes(Figure 8.1) according to the industry standard ARP1420b (SAE 2002). The probes are positioned along eight diametrical lines that are equally spaced azimuthally around the circumference of the AIP (Figure 8.1). The probe tips are located such that each probe is at the center of area per ARP guidelines. The rake assembly was designed to be interchangeable with a similar rake integrated with dynamic pressure sensors for measurements of dynamic distortion data. The total pressure rake is supplemented with

eight matching static pressure ports that are equally-spaced azimuthally along the inner surface of the diffuser at the edge base of each diametrical rake segment. In addition, twelve and five streamwise static pressure ports are equally spaced along the bottom and top surfaces of the diffuser, respectively, beginning at $x/D = 0$. All pressures are measured using the Pressure systems (now Measurement specialties) device that was described in Chapter 1.

Calibration of the S-duct facility to relate the blow motor RPM to the Mach number at the inlet to the S-duct model was performed by using the AIP pressure rake and a Pitot-static probe located in the center of the duct transition section just upstream from the diffuser inlet plane $x/H = -1$. Figures 8.2a and b show the variation of M with blower RPM and the variation of the static pressure along the centerline of duct. Note that corresponding Mach numbers at the inlet and the AIP are slightly different because of the change in the cross sectional areas (inlet is 5% smaller that the AIP). The nominal operating Mach number is based on the diffuser design requirements and is set to $M_{AIP} = 0.55$. The streamwise static pressure distributions in Figure 8.2b were measured in the range $0.5 < M_{AIP} < 0.72$starting at the diffuser inlet plane ($x = 0$) and ending at the AIP plane ($x/D = 2.5$). In addition to the twelve ports on the inner surface of the diffuser, a blank insert was equipped with additional ports (these ports cannot be easily incorporated in the presence of flow control hardware on the insert). Note that the region of peak flow acceleration, upon entering the diffuser ($x/D = 0 – 0.3$"), is not populated by static pressure ports. This profile is typical of a diffuser without separation, as indicated by the lack of distinct flattening of the profiles. In addition, it is interesting to note that this phenomenon is absent even at the highest Mach numbers measured. The slight upward trend in the profiles is due to the diffuser's cross sectional area slowly increasing with streamwise distance away from the entrance, partially due to the Gerlach shaping and partially due to the change from D to round shape.

8.3 Emulation of the Ingested Boundary Layer

Any experimental investigation of a BLI offset diffuser faces a significant challenge in emulating the effects of the surface boundary layer that the diffuser encounters on airborne platforms. Two key features of the approaching flow, a thick incoming boundary layer (relative to the inlet characteristic height *H*) and the interaction of this boundary layer with the inlet cowl lip, are not present in typical test configurations unless the airframe and the inlet sections are mounted in a wind tunnel. In a typical diffuser test, specially shaped bell mouths and screens are used to simulate the upstream boundary layer on an airborne platform (Bruce, 1974).

As discussed by Owens 2002, the flow that approaches a BLI inlet is bisected by the inlet so that a pair of necklace vortices is formed at the locations where the BLI intersects with the wall. One of each of these pairs of vortices that are formed are ingested into the inlet and, it should be noted, have the same sign as the natural secondary flows which form in the duct. The flow within the D-shaped inlet is characterized by two primary domains. The bottom wall region is dominated by the thick boundary layer and its roll-up in front of the cowl lip into a necklace vortex. The rest of the captured flow rotates as it enters the diffuser, sweeping the inner flow down along the wall towards the bottom center of the duct and, thereby, enhancing the secondary, streamwise vorticity. The thick boundary layer near the bottom surface and the counter-rotating corner vortices need to be emulated by flow conditioning hardware.

In the present investigations, these flow features are engendered by a ‘honeycomb’ fence that was developed at Georgia Tech (Figure 8.3).The momentum deficit is realized by a gradual reduction in the size of the cells towards the surface combined with streamwise thickening of the fence’s channels. In addition, the cells on both sides of the plane of symmetry are turned horizontally ‘inboard’ as their distance from the centerline increases (the turning flow in the real diffuser is most pronounced near the corner that is formed by

the intersection of the cowl with the surface).The fence is placed upstream of the diffuser's inlet at x/D = -2.4and forms the base flow for the present investigations.

The resulting baseflow at the inlet to the diffuser is characterized using the hot-wire measurements at three spanwise locations z/H = -0.5, 0, and 0.5, and x/H = -1 upstream of the diffuser throat where H is the diffuser throat height. The resulting cross stream distributions of the time-averaged velocity and RMS velocity fluctuations are shown in Figure 8.4 along with the corresponding distributions of the flow in the absence of the honeycomb fence, for reference. These data show that the boundary layer is significantly thickened by the fence to over a third of the diffuser's height while maintaining the flow's symmetry bout the center plane (z/H = 0) in the absence of the fence. It is also noteworthy that the difference in velocity deficit between the center plane and the outboard sections indicate the three-dimensionality of the oncoming flow that is consistent with the inlet flow in an airborne diffuser. Secondary peaks in the RMS velocity profile at the central plane are attributed to the shear layer that forms at the fence upper boundary, and they subsequently decay downstream.

The primary characterization of the diffuser's performance was based on the time-averaged, total-pressure measurements at the AIP using the 40-probe array and corresponding pressure measurements at the bases of the eight total pressure rakes. In addition, the baseflow was also characterized by measurements of the static pressure along the bottom and top surfaces between x/H = 0 and 3.4. Results for the base flow are shown in Figure 8.5.$DPCP_{avg}$is the circumferential distortion metric averaged over all five of the rings of total pressure tubes. This metric is defined in ARP1420b (2002). Each engine has a distortion limit above which it will not operate safely (stalled blades, high cycle fatigue, surge, stall etc). Therefore, any reductions in distortion improve the margin of safety for any engine which is paired to this inlet. The AIP contour map indicates that there is a low-pressure region in the bottom center domain. These measurements are compared with the AIP distribution during similar tests at NASA

Langley Research Center (Berrier, 2004) which utilized a surface-mounted inlet to simulate the natural evolution of an airborne-like flow at the diffuser inlet including the interaction with the inlet lip. The global AIP features in Figure 8.5aare similar to the distributions measured at LaRC at the same free stream Mach number and inlet capture ratios. The pressure profiles along the bottom wall, Figure 8.5b, further confirm the lack of separation and are similar to the curves shown in Figure 8.2b.

8.4 Flow Control Actuation

The development of the hybrid actuation begins with the design of the passive flow control devices. Vortex generating vanes were selected for this study due to their simple geometric shape, established ability to generate single sense vorticity, and ease of manufacture. The starting point for the development of the vanes is the optimized vane configuration used in Owens et al (2008). However, the goal of these flow control vanes was to provide a 'fail-safe' level of control with a minimum impact on the pressure recovery at the AIP. With this goal in mind, a study was performed of several vane configurations and resulted in a vane configuration with six vanes where each set of three vanes were offset outboard from the centerline in an effort to uniformly distribute the low speed flow that is entering the duct. These vanes are integrated into the flow control insert (shown in Figure 8.1), upstream from the active flow control component, as shown in Figure 8.6b. More details on the selection process of the passive flow control devices can be found in the NASA report by McMillan (2012).

Synthetic jets are selected as the active component of the hybrid actuator because they do not require an external air supply and can be operated over a relatively broad range of frequencies. For the hybrid control tests, the upstream insert was populated with passive flow control vanes in a pattern and location that was designated for the hybrid control integration. An active control insert was designed and built such that its control source corresponds to three rows of orifices. The jet centerline of the cylindrical orifice conduits

are canted at 45°in the spanwise direction relative to and away from the center plane. In the present investigations, high-speed synthetic jets are generated using three 38 mm piston actuators that drive a common plenum. These actuators are similar in structure and operation to the piston-driven synthetic jet actuators of Crittenden and Glezer(2006).The three pistons synchronously use a Baldor brand servo motor equipped with a speed controller over a frequency range (up to 133 Hz) which is nominally set at 133 Hz. The control insert is manufactured using stereolithography (SLA) and is split into two components so that its upstream section, which contains the vortex generating vanes, can be replaced independently of the synthetic jet insert (Figure 8.6b) and, therefore, enable testing with hybrid or jet-only configurations.

The overall, time-averaged effects of passive-only, active-only, and hybrid actuation are shown in Figure 8.7 (the pressure distribution of the base flow is shown in Figure 8.7a). In the presence of passive actuation (Figure 8.7b), the low pressure domain of the base flow, which exists in the bottom center quadrant of the AIP, is redistributed into three distinct low pressure lobes centered in the right, left and bottom quadrants due to the roll up of the streamwise vortices generated by the flow control vanes. This circumferential redistribution of the pressure deficit results in reduction of the baseline $DPCP_{avg}$ by about 20%. When the synthetic jets are activated in the absence of the passive vanes, the suppression of the pressure deficit in the central bottom quadrant is lowered, but the redistributed low pressure region up along the surface is confined to the near-wall region, (Figure 8.7c) without the generation of side lobes (Figure 8.7b). This effect at the AIP suggests that the synthetic jets act upon the baseline flow much like passive control elements by redistribution of the low pressure region, but their effect is more confined to the wall region. Furthermore, the region of high speed flow in the bottom half of the AIP has been with the low speed flow found in the baseline flue due to the enhanced circumferential mixing of the flow during the actuation cycle of the jets. *Consequently, jet actuation alone induces about the same reduction in the average overall distortion as*

passive control. Finally, when the two actuation methods are combined to form the hybrid actuation (Figure 8.7d), both effects seem to merge, as is evident in both formation of the three distinct lobes of low pressure and concomitant suppression in the magnitude of $DPCP_{avg}$. These combined effects result in additional suppression of the overall distortion by approximately 35% compared to the baseflow.

The overall impact of the actuation on the distortion pattern at the AIP over the range of tested Mach numbers is reflected in the time-averaged $DPCP_{avg}$ (Figure 8.8a). First, there is a clear and nearly-equal reduction in distortion compared to the base flow over the entire range of tested Mach numbers, both for passive and jet-only control approaches, which results in a reduction of about 20% in the average distortion over the baseline flows. Second, the superposition of the passive and jet actuation in hybrid control further reduces the distortion such that an overall reduction of 35% relative to the base flow is achieved at $M = 0.55$ (the design flow rate). Figure 8.8b illustrates that these improvements in distortion do not come at the expense of increased drag penalty, as shown by the total pressure recovery in the base flow and, in the presence of actuation, over the same range of the tunnel speeds (jet actuation has virtually no effect relative to the base flow, while passive and hybrid actuation only marginally reduce recovery).The patterns of pressure at the AIP shown in Figure 8.7 indicate that the individual streamwise structures formed by the hybrid flow control elements merge into large duct scale rotational structures which counteract the secondary flow in the duct resulting in the redistribution of the low speed fluid that resides in the lower center quadrant of the baseline flow up along the sidewall in a manner which results in a more uniform flow entering the simulated engine plane. It is important to note that the passive actuation is intended as a fail-safe system with acceptable AIP distortion level. These data indicate that further investigations of integration and optimization of passive and active flow control components into hybrid configurations can yield further improvements in performance.

8.5 The Time-Dependent Dynamics of the Actuated Flow

The effects of the superposition of passive (vanes) and active (synthetic jets) time-periodic actuation are further characterized using phase-locked measurements of the time-dependent dynamic, total-pressure at the AIP. To this end, the AIP rake of dynamic pressure sensors that is used is sampled phase-locked to a reference signal from the jet actuators. The phase-averaged ensembles of the pressure traces, $<p_o>$, are used to compute the variation of $<DPCP_{avg}>$with t/T during the actuation cycle (Figure 8.9). The two time-averaged levels of $DPCP_{avg}$, in the absence ($DPCP_{avg,OFF}$) and presence ($DPCP_{avg,ON}$) of jet actuation (but with the vane array present), are shown. A time trace of the phase-averaged *DPCP* includes phase-averaged color raster plots at 5 time steps (A-E) during the actuation cycle and illustrate the changes in the distribution of pressure.

The effect of the vanes is ascertained by the favorable reduction in distortion over the entire cycle as is apparent from the reduction in $DPCP_{avg,OFF}$ (passive control only), shown in Figure 8.9 as a straight line, and is a *25%* reduction compared to the baseline flow. This favorable reduction in the distortion coefficient due to the vanes is applied over the entire cycle since the distortion is ensemble-averaged with respect to the jet cycle. Therefore, the <DPCP> plot only reflects the additional, time-periodic changes that the synthetic jets generate while acting upon the flow produced by the interaction of the vanes with the flow.

There is a phase delay between the start of actuation (t/T = 0) and when the changes in total pressure are measured at the AIP. This phase delay is due in part to the advection of the flow structures generated by the flow control elements as well as their interactions with each other and with the diffuser flow.

At the beginning of the cycle (t/T = 0, A), the low speed, low total pressure at the bottom center of the AIP is redistributed to three distinct low pressure domains. This is similar to the pattern in the absence of synthetic jet actuation (Figure 8.7b). As the jets begin to alter the AIP pressure distribution, the magnitude of the low pressure in the three low-

pressure domains begins to decrease further as shown at B (t/T = 0.21). This leads to a slight reduction in the overall AIP-average distortion. Next, there is a distinct rise in the <*DPCP*> at C (t/T = 0.38) caused by a concentration of low pressure in the outer three total pressure tubes on the lower, center segment of the AIP. The <*DPCP*> then reverses its rise and decreases to a cycle-minimum at D (t/T = 0.58). However, instead of a clear redistribution of low-pressure flow caused by the formation of duct-scale vortical structures, it appears that the flow structures formed by the synthetic jets augment the existing structures formed by the vanes. This results in an increase in the total pressure in the three low-pressure domains that are induced by the vanes alone. These duct scale streamwise vortices are formed by the synthetic jets as the individual streamwise vorticies formed by each exit orifice merge to generate larger streamwise structures. The rotation of these structures formed by the jets force the low speed flow up the sidewall of the duct. As the momentum of the actuation jets begins to decrease near the end of the cycle, <*DPCP*> rises and distortion level is similar to the level at A. The resulting AIP contour of the total pressure <p_o>is shown at point E.

The flow dynamics during the actuation cycle of the jet is further analyzed using proper orthogonal decomposition or POD (e.g., Berkooz, Holmes, and Lumley 1993) of the time series of 'snap shots' of the AIP total-pressure fluctuating fields, with instantaneous total pressure $p_o = p_{o,m} + \text{sum}(a_i \cdot \phi_i)$, where i = 1 – N is the i^{th} of N POD modes ϕ_i , and a_i is it time coefficient. A positive time coefficient indicates that the computed mode sums with the other modes while preserving the same sign throughout the field, whereas a negative time coefficient would reverse the sign of the values within the computed mode. The main significance of this decomposition of the pressure field stems from the fact that POD modes are projected such that they are ordered from the most energetic to the least energetic mode, and the first several modes can be sufficient to capture the dominant time-dependent dynamics. Figure 8.10shows color raster plots of the first (most energetic) mode of the jet-induced fluctuating total-pressure field at the AIP at four AIP

Mach numbers. At the lowest Mach number, the mode shown in Figure 8.10a is of a single sign across the AIP, and the time coefficient is nearly sinusoidal. This is attributed to the fact that control jets are simply too powerful at this low Mach number, and this mode represents blockage and modulation of the flow (nearly sinusoidally) across the entire AIP when they are active. Streamwise vorticies still form as indicated by the two lobes in the upper right and upper left quadrant. As the Mach number is increased (Figure 8.10b), three distinct lobes of opposing sign begin to form at the bottom center and right and left sides . Despite this, the behavior of the magnitude of the coefficient indicates that the mode sums to zero over a single jet cycle. The dominant mode structure at $M = 0.48$ and 0.55 (Figures 8.10c and d, respectively) exhibit significantly different flow dynamics than at the low Mach numbers counterparts. The mode structure is characterized by distinct azimuthal domains of opposite sign with the upper right and left quadrants having the opposite sign compared to the same area in the two lower speed flows (8.10a and 8.10b).It is interesting that, at $M = 0.48$ and 0.55, the momentum exchange is always towards the bottom half of the AIP as indicated by the sign and magnitude of the plots in Figures 8.10c and d in the lower right and left quadrant. This is due to the pair of streamwise vorticies which draw high speed flow down toward the center bottom of the AIP and force the low speed flow up along the sidewall toward the upper half of the AIP.

The mode structure and time coefficients along with the coefficient power spectra of the first four most energetic POD modes during hybrid control at $M = 0.55$ are shown in Figure 8.11. The time coefficients show that the mode dynamics are associated with multiple dominant frequencies that for mode 3 and 4 appear to be only loosely coupled to the actuation frequency. Mode 1 is already discussed in detail in connection with Figure 8.10. Mode 2 is composed of three low pressure lobes at the bottom center and at the center of the left and right quadrants. These lobes contributes predominantly favorable changes to distortion suppression when its time coefficient is positive and unfavorably

when its time coefficient is negative due to the fact that its pattern is effectively opposite of that which contributes to unfavorable distortion. Mode 3 represents changes in the velocity among all four quadrants, although with a very low amplitude of its time coefficient a_3. Mode 4 also has a low contribution to the total pressure, while its momentum exchange is predominantly divided between upper and lower halves of the AIP for all times where a_4 is positive.

Finally, Figure 8.12compares <*DPCP*>with the time coefficients (a_1 and a_2) of the first two most energetic POD modes. The important features of the distortion were described in detail in Figure 8.9. The time traces show that modes 1 and 2 yield favorable contribution to distortion suppression as indicated by the fact that when their time coefficients are negative and positive, respectively, the distortion is lower than the time average distortion. Mode 2 has a local minimum at t/T = 0.4 and, as indicated by the vertical dashed line, this is coincident with the maximum distortion values measured. A declining$a_2$results in an increasing distortion. For example, the slight rise in distortion before the peak (the peak is marked with a vertical dashed line) corresponds to a section of time where a_2 is negative. Additionally, the distortion rise to its cycle peak, starting at t/T = 0.3, is coincident with an increase in magnitude of a negative a_2. In this region the distortion is decreasing while mode 1 is still relaxing from the previous cycle. These dynamics of mode 2 reduce total pressure at the bottom central zone due to the negative coefficient and the positive sense of the mode in that region which, in turn, increases distortion. This indicates that there is a slight initial decrease in the speed of the flow in this region due to the amount of energy that it takes to accelerate the flow exiting the synthetic jets. As this flow is exiting with zero velocity in the local streamwise direction, the process of formation of streamwise vorticity would necessarily include acceleration which is reflected in a momentary decrease in the speed of the flow in the lower central quadrant.

These data show that the peak distortion of<*DPCP*> at $t/T \approx 0.4$ approximately coincides with the negative peak of a_2.As $a_1$continues to become more negative $t/T > 0.4$, increasing the effect of mode 1, a_2 increases in value but decreases in magnitude decreasing the contribution of mode 2. This trend is due to the velocity increasing in the center of the lower right and lower left quadrants (a contribution of mode 1)and, at the same time, the flow in the bottom center of the duct is increasing in speed. This is a reflection of the fact that as streamwise vortices forming from the flow that emanates from the synthetic jets momentum is transferred up along the bottom center of the duct. Once the streamwise vorticies have been established, the low speed flow that is forced up along the bottom sidewall of the duct resides at the center right and center left quadrants of the duct which is reflected in the positive contribution of the first mode up until the minimum value of the distortion at $t/T \approx 0.55$. It is the same trend that results in $a_1$reaching its minimum amplitude just before the local minimum of <DPCP>. These data indicate that a streamwise tilt to synthetic jets would remove the spike in distortion due to the acceleration of the flow exiting the jets. Additionally, these data show that it is the formation and movement of the two large vortical structures that dominate the dynamics of the flow. This data indicates that flow control methods which are able to actuate faster than the relaxation time associated with the breakdown of these two large structures, shown by the relaxation of mode 2, would be able to control the flow with less variation in distortion during the cycle.

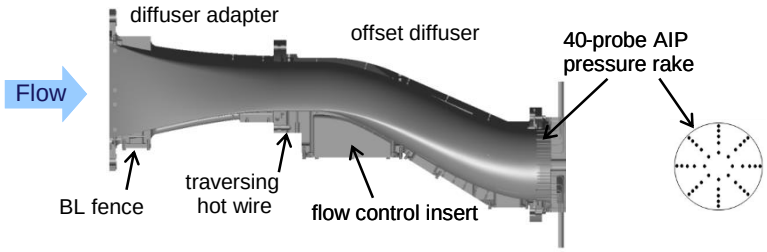

Figure 8.1*Schematic of the offset diffuser hardware.*

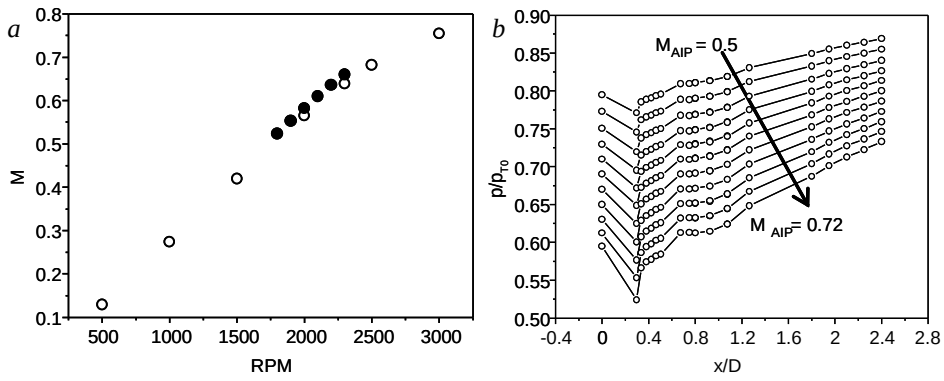

Figure 8.2 *a)Variation with blower RPM of the nominal Mach number measured at a station at the downstream extent of the diffuser adapter (start of the diffuser)(○) and at AIP (●), b) Streamwise distribution of the static pressure along the diffuser's lower surface at different M.*

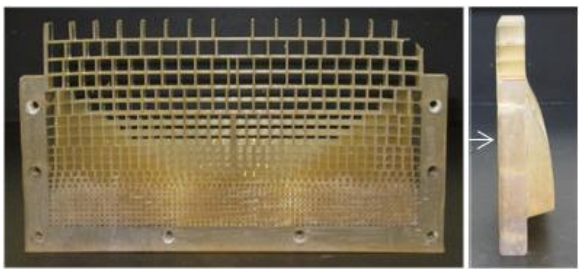

Figure 8.3 *A honeycomb fence designed for thickening of the diffuser's inlet boundary layer.*

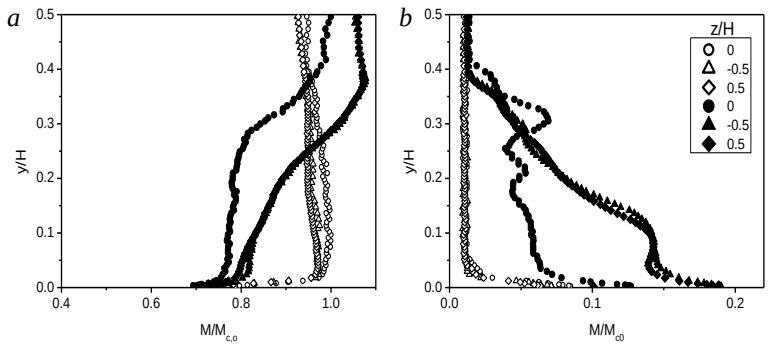

Figure 8.4 *Time average Velocity (a) and RMS velocity fluctuation profiles (b) for the natural (open symbols) and the base flow manipulated by the honeycomb fence (solid symbols) at the centerline (●), 0.5H (▲triangle), and starboard (♦diamond) hot-wire measurement locations.*

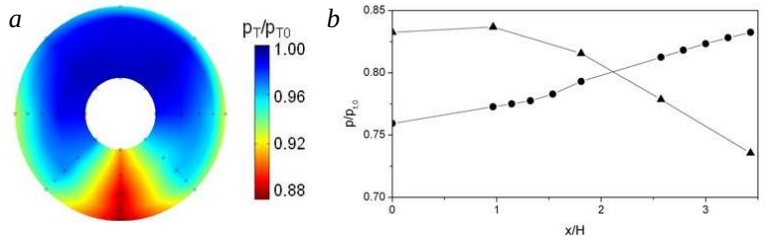

Figure 8.5 *Color raster plot of the time-averaged total pressure at the AIP (a), and static pressure distributions along the bottom (●) and top (▲) diffuser surfaces for the base flow at M_{AIP} = 0.55, $DPCP_{avg}$ = 0.028 (b).*

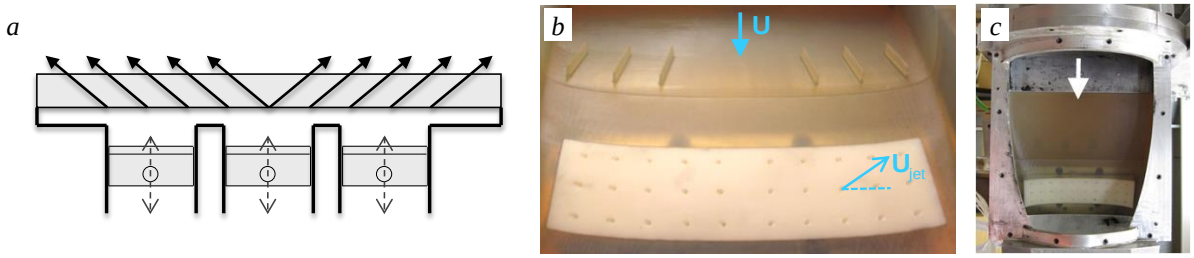

Figure8.6*Schematics diagram of the synthetic jet modules (a) the hybrid flow control configuration showing the flow control vanes and exit orifices for the synthetic jets(b) installed in the duct (c).*

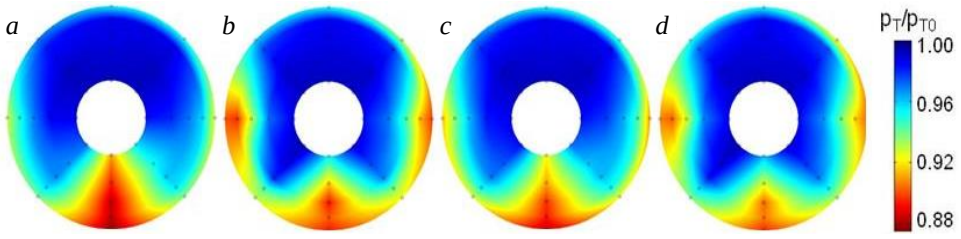

Figure 8.7*Time-averaged AIP total pressure contour maps, showing the base flow (a), and the effects of passive (b), active (c), and hybrid (d) actuation at M_{AIP} = 0.55. The respective $DPCP_{avg}$ values are: 0.0280, 0.0219, 0.0220, 0.0179.*

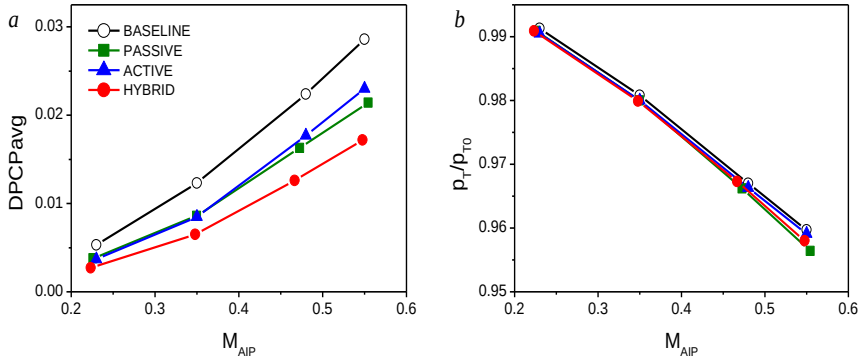

Figure 8.8*Variation with Mach number of: a) Time-averaged total pressure distortion at the AIP, and b) Total pressure recovery for the base flow and in the presence of passive, active, and hybrid actuation.*

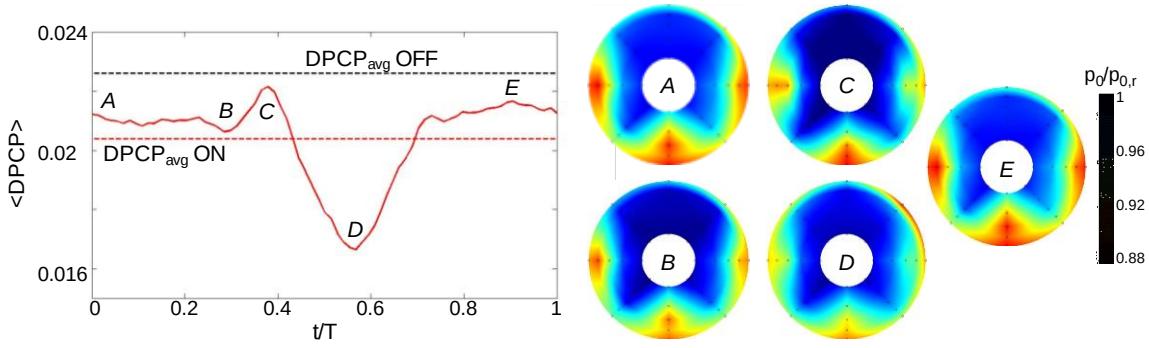

Figure 8.9*Time trace of the phase-averaged <DPCP> during hybrid control (left) and raster color plots of the AIP pressure distributions $<p_0>$ at times A through E.*

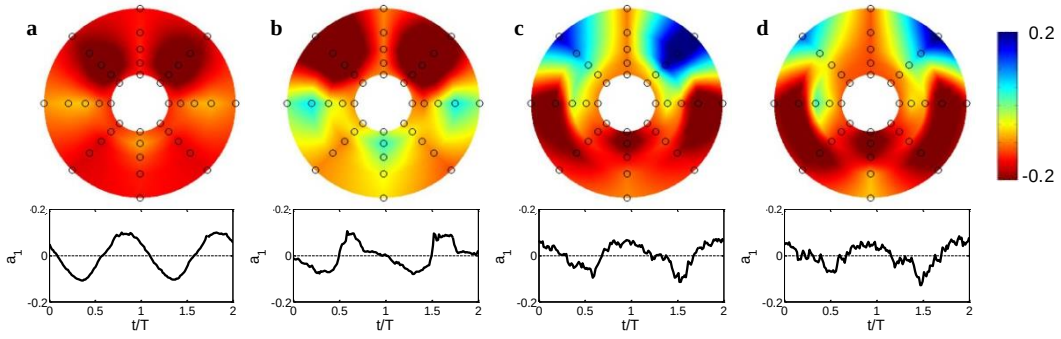

Figure 8.10*The most energetic POD mode and its time coefficients for hybrid actuation at M = 0.22 (a), 0.35 (b), 0.48 (c), 0.55 (d).*

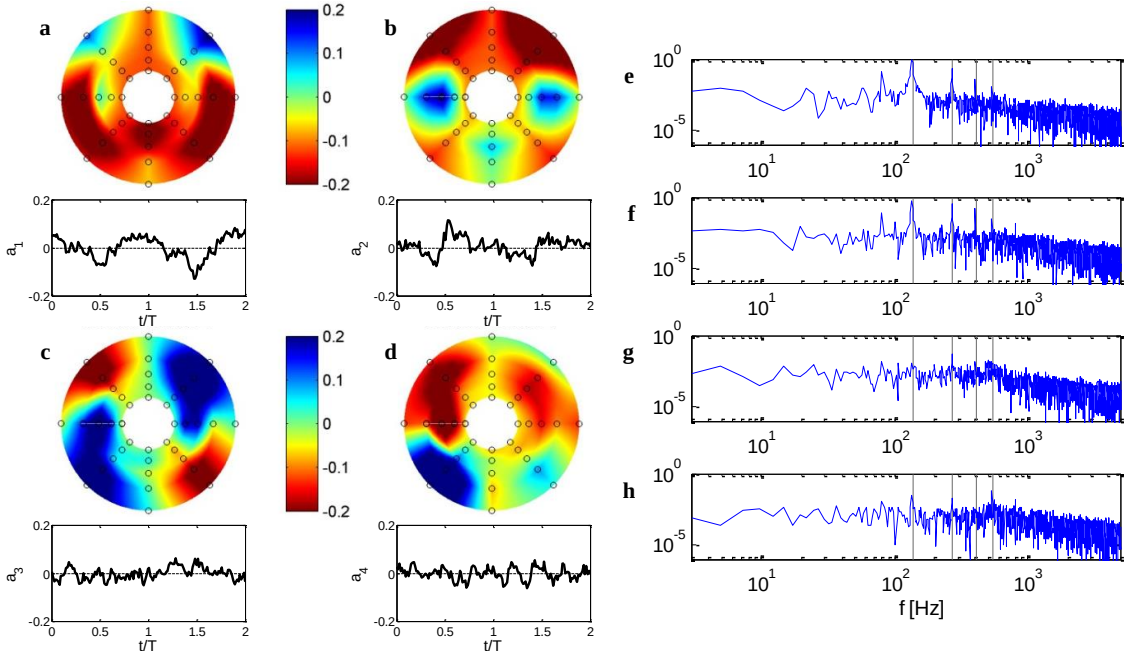

Figure 8.11*The most energetic four POD modes and their time coefficients (a–d) for hybrid actuation at M = 0.55, and the corresponding power spectra of the time coefficients (e–h).*

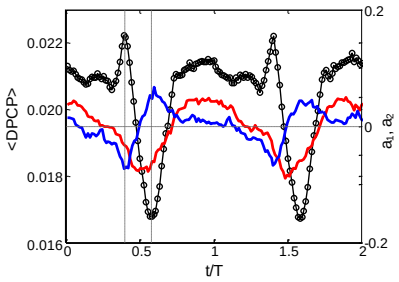

Figure 8.12*Time trace of the phase-averaged: distortion <DPCP>, and of the time coefficients of the first (red) and second (blue) POD mode for the hybrid flow control at M = 0.55.*

CHAPTER 9

CONCLUDING REMARKS

9.1 Summary

The dissertation focuses on investigations of the mechanisms, evolution, and effectiveness of active flow control in subsonic internal compressible flows with strong adverse pressure gradients that often result in local flow separation. The complexity of the compressible flow dynamics is especially exacerbated by the appearance of shocks and shock-induced separation when the flow becomes transonic as a result of the interplay and coupling between the shock, the incipient flow separation, and the dynamics of the ensuing separated shear layer. An important objective of the present research is to investigate and understand the control mechanisms of the shock structure and stability by exploiting the coupling between the induced separation and the shock. Control is effected *indirectly* by controlling the separated flow, and these fundamental aspects of the flow are investigated on a canonical 2-D converging-diverging insert where the flow typically separates on the diverging section. The ensuing active flow control approaches are demonstrated in two important applications. First, compressible flow in an aggressive thrust reverser model in which a strong adverse pressure gradient induces flow separation even at subsonic speeds, and second, mitigation of the adverse effects of compressible secondary flow within a subsonic offset diffuser.

The present research utilized an array of the active flow control elements that included fluidic oscillating jets, pulsed jets, and synthetic jets. Each of these flow control elements imparts unsteady momentum injection across the flow boundary over a broad range (100 to 10,000 Hz) of actuation frequencies that couples to instabilities of the base flow with or without net mass injection. Characterization of the flow in the absence and presence of actuation is accomplished using a suite of diagnostic tools. Static and dynamic

pressure measurements are used for assessing time-averaged and time-dependent changes in surface pressure distributions upstream and downstream of the shock that include effects of flow separation and its coupling to and interplay with the shock strength and displacement. In the offset diffuser, a rake of 40 static/dynamic pressure sensors is utilized to map the total pressure distributions and estimate the total pressure distortion. Global features of the flow fields and the shock dynamics are elucidated from the conditionally-sampled schlieren visualization using high-resolution video imaging at frame rates of up to 8,000 fps. Imaging of the shocks enables correlations between the dynamic pressure fluctuations in the separated flow domain and the unsteady shock dynamics. Finally, high-speed (about 3,000 fps) PIV measurements in the center cross-stream plane are used to characterize the time- and phase-averaged flow field upstream and downstream of the separation including the corresponding shock dynamics.

The effects of flow actuation are investigated in the separated flow domain over the converging-diverging 2-D curved surface insert. The strong adverse streamwise pressure gradient results in subsonic separation that transitions to shock-coupled separation when the flow becomes transonic. This transition occurs when the test section Mach number upstream of the insert is increased, and accelerating flow over the converging segment of the insert becomes critical at a pressure ratio of ~1.27, when a shock is formed past the apex. As the Mach number increases further, the shock is progressively displaced in the streamwise direction, tilts forward, and extends in the cross stream direction towards the opposite wall. Ultimately, the shock spans the full height of the test section when the flow through the tunnel becomes choked at a pressure ratio of 1.37.For a given Mach number (or pressure ratio), the shock in the base flow is characterized by its shape and the time-averaged cross stream profile and the cross stream variance profile in its streamwise position due to the inherent broad-band streamwise oscillations of the shock. For example the shock is translated from x/H = 0.6 to x/H = 1.8 (measured at y/H = 1) for a range of p_i/p_e = 1.27 to p_i/p_e = 1.39, while over the same range the shock ‘tilts’ forward

(cf. Figure 3.7). Furthermore, an important element of this characterization is the strong correlation of the shock oscillations with the dynamic pressure that is measured within the separated flow domain downstream of the shock.

When actuation is applied using a spanwise array of integrated fluidic oscillators, the flow attachment over the curved surface is extended, and the cross stream spreading of the separating shear layer is increased and is accompanied by enhanced small scale motions. For example at p_i/p_e = 1.39 the shock is translated from x/H = 1.3 to x/H = 2.5 at C_q x 10^3 = 2.5 as measured at y/H = 1 (cf. Figure 4.8). Of particular note is the tilting of the low-speed edge of the shear layer towards the surface. In the presence of a shock, the modified pressure field results in variation in the shock position and shape. Analysis of the shock displacement shows that in the presence of actuation, the effects of the local, flow control induced, changes in the pressure field on the shock are not the same as the effects of global changes in the pressure ratio (cf. Figure 4.8 and 4.9).The relation between the streamwise displacement of the shock and the actuation amplitude (given by the actuation flow rate coefficient, C_q) was established over a broad range of Mach numbers (i.e., pressure ratios between 1.27 and 1.4, as 1.27 corresponded to the first appearance of a shock and the highest pressure ratio was limited by the facility capabilities), and demonstrates that the shock position downstream of the apex of the insert can be tuned using variable actuation. This relation between the actuation and shock displacement, along with the strong correlation between the shock displacement and dynamic pressure measured on the surface downstream of the curved flow insert, indicate that this actuation approach can be utilized for closed-loop control of the shock stability.

One of the important aspects of the present approach to controlling the shock dynamics is the characteristic time scale of the shock response to the actuation input. The time scales are assessed from the combined flow response of the separated shear layer and the shock to step actuation which yields the response to the onset and termination of the actuation.

The actuation is applied using an array of fast, individually-controlled pulsed jet actuators having a frequency response of 1kHz. The flow response was analyzed using phase-locked Schlieren measurements, and the rate of change of the strength of the actuation jet (from bench top hotwire measurements) was related to the shock position as assessed from digitized Schlieren images and PIV computed vector fields. These measurements showed that at $p_i/p_e = 1.35$ the shock translates rapidly downstream from $t/T_r = 12$ to 20 (cf. Figure 5.12). The dependence of these timescales on the tunnel pressure ratio provides insight into the effect of the convective timescales on the transient response of the flow. For example, the shock (as measured at $y/H = 1$) begins to rapidly translate downstream at $t/T_r = 11.5$ for $p_i/p_e = 1.30$ whereas the shock begins to rapidly translate downstream at $t/T_r = 7$ for $p_i/p_e = 1.41$ (cf. Figure 5.18).

The response of the flow to repetitive actuation was investigated using actuation frequencies of up to 900 Hz. These investigations yielded the hysteresis associated with repeated actuation, the timescales and their relation to the response to step actuation, and the actuation's control authority were determined for a range of pressure ratio and actuation frequency.

Active flow control of a compressible separating flow using momentum injection across the flow boundary was applied for mitigation of flow separation owing to an aggressive adverse pressure gradient within a thrust reverser duct. These investigations demonstrated that control of the separation over the internal flow turning surface (dubbed the "bullnose") can lead to significant reduction in internal losses and therefore to an increase in the flow rate through the duct. In fact, reduction of the separation over the bullnose increases the flow through the cascade vanes at the exit plane of the duct. Furthermore, the ability to mitigate flow separation on increasingly more aggressive internal flow-turning surfaces enables an overall reduction in the duct length by reducing the required streamwise scale of the bullnose. The "baseline" configuration of the flow turning surface is selected to minimize the adverse effects of the separation in the absence

of separation control. In the absence of actuation, a reduction of 52% in the streamwise length of the bullnose results in 8%loss of mass flow rate. Improving the flow through the thrust reverser duct by control of separation was demonstrated using a number of increasingly aggressive (shorter) bullnose sections ranging from $L/H = 1.7$ to 0.8 (where L and H are the length and height of the bullnose, respectively) that in the absence of separation control led to increased separation and reduced overall mass flow rate. The actuation magnitude that was needed was up to 1.3% of the mass flow in the duct. It was shown that for pressure ratios between 1.04 and 1.24, separation control can recover the mass flow rate through the tunnel and bring it to the level of the base flow configuration (i.e., increases of up to 7% relative to the uncontrolled flow).

A second engineering application demonstrates the utility of compressible flow control through its effectiveness for reducing flow distortions due to secondary vortices in the absence of global separation within an offset diffuser ($M < 0.55$) that models the flow characteristics of a boundary layer ingesting, blended wing body (BLI-BWB) diffuser. In the full-scale diffuser, flow distortion is induced by the momentum deficit of the ingested thick boundary layer coupled with the evolution of secondary flows that leads to the formation of large-scale, streamwise vortices. In this, model scale, demonstration, control is affected using synthetic jets combined with passive vortex-generating vanes (to achieve fail-safe performance). It was shown that independently using passive (vanes) or active (synthetic jet) actuation leads to similar reductions in distortion (up to 21% at $M = 0.55$). However, superposition of active and passive components results in an overall reduction in distortion of 35% at $M = 0.55$.

9.2 Conclusions

The present dissertation focuses on investigations of the effects of control of flow separation in subsonic compressible internal flow in the presence of a strong adverse pressure gradient that is exacerbated by the formation of a shock at sufficiently high

Mach numbers. The present investigations placed specific emphasis on active manipulation (using jet actuation) of the separation over a two-dimensional curved (converging-diverging) surface, and on the interaction of a shock with the separating flow. The objective is to exploit separation control to mitigate the losses that are associated with the separation and to manipulate the reciprocal coupling between the separated flow and the shock to indirectly control the shock position and stability.

The present investigations confirmed that when the Mach number of the base flow is increased (in the absence of actuation), the separation is displaced downstream, as the upstream boundary layer becomes thinner and able to withstand higher adverse pressure gradients. A critical condition is reached at pressure ratios greater 1.26 when the flow becomes sonic at the apex of the curved surface (representing a 'throat'), and continues to accelerate over the diffusing aft section. Depending on the local surface curvature, the locally supersonic accelerating flow terminates in transonic shock past the apex and the flow becomes subsonic downstream. The present experiments showed that the separation does not immediately couple to the shock, i.e., an initial weak shock forms downstream of the incipient separation, which is still primarily induced by the strong adverse pressure gradient. However, as the Mach number increases, the shock moves upstream and becomes locked to the separation at a pressure ratio 1.30. This locking marks the transition to shock/boundary layer separation at which the separation and separating shear layer and the shock become coupled. This coupling is clearly significant from the standpoint of flow control approaches.

The present investigations demonstrated the utility of active flow based on momentum injection across the flow boundary using spanwise arrays of jet actuators for delaying compressible separation in the presence of a strong adverse pressure gradient well before the critical flow conditions for the formation of a shock are realized. The effectiveness of this approach was demonstrated in a thrust reverser duct (cf. Chapter 7) leading to significant reduction in internal losses.

This approach to separation control was used to develop a novel approach for *indirect* control of the shape and stability of transonic shocks by exploiting their strong coupling to the separated flow. Flow attachment induced by flow control actuation leads to streamwise advection of the location of separation, and to significant vectoring and cross stream spreading of the separating shear layer. As a result, the concomitant changes in the local pressure field affect the shock position and shape. The present investigations demonstrate that the actuation jet causes a low pressure region to develop downstream of the shock and beneath the separated shear layer and causes the flow to vector and attach ostensibly due to Coanda-like effect of the convex surface. The acceleration farther along the curved surface results in streamwise translation of the shock. Furthermore, the attachment increases the effective cross sectional area of the duct downstream of the shock and results in pressure recovery.

Analysis of the shock displacement caused by flow control actuation is effected by local, somewhat subtle, changes in boundary conditions and it is different from the response of the shock to global changes in the flow (Mach number or pressure ratio). The present work has not only demonstrated a strong reciprocal coupling between the actuation amplitude and the changes in the shock position and structure, but also pointed to strong correlation between the shock displacement and surface dynamic pressure downstream of the shock (within the separated flow domain) thereby indicating that this actuation approach can be utilized for closed-loop control of the shock position and stability.

At a number of combinations of pressure ratio (p_i/p_e) and flow rate (C_q) supplied to the flow control devices a lambda shock is seen to exist. The emergence of the lambda shock structure is attributed to shock locking to the separation point, while the increasing jet momentum continues to vector the shear layer and upper flow. Therefore, the shock near the surface slants to accommodate increasing flow vectoring. At the point that the flow past the weakened shock is still supersonic, it further accelerates and eventually terminates in a normal shock that forms the downstream leg of the lambda shock

structure. Although the flow initially remains separated off the leading leg of the lambda shock, the full jet momentum is capable of fully attaching the flow underneath the lambda shock and even further downstream of the shock.

It is important to elucidate the time scales inherent to the propagation of the changes in pressure imposed by motion in the separated shear layer (due to the rapid onset or termination of actuation) and which are directly linked to the motion of the shock. As was shown in Chapter 5, the rapid onset of actuation (cf. Figure 5.5) results in the rapid downstream translation of the shock commensurate with the reattachment of the separating shear layer (cf. Figure 5.7-5.10). The changes in the shock strength (as indicated by the density gradient using schlieren) and shape during its rapid downstream motion indicate the shock is moving in a non-equilibrium fashion which could be considered unsteady. The rapid motion of the shock associated with a step change in downstream conditions is characterized (cf. Figure 5.12) for three pressure ratios (p_i/p_e = 1.3, 1.35 and 1.41, cf. Figure 5.18) and it is found that both the 'delay' time and the rate of change of the shock are affected. The delay time, the time between when the actuation is triggered and the shock begins its rapid downstream motion, decreases for increasing pressure ratio (t/T_r = 11.5, 10, and 7 for p_i/p_e = 1.3, 1.35 and 1.41 respectively), whereas the rate at which the shock translates downstream decreases for increasing pressure ratio. These two trends, which are observed for increasing pressure ratio, are due to the combination of: an increase in the size of the supersonic bubble, which increases the distance over which the downstream changes need to propagate; an increase in the convective speed downstream from the shock, which decreases the rate at which the downstream changes propagate upstream and the rate at which the shear layer can reattach, and a downstream motion of the shock which moves the shock closer to the flow control array. Quantification of the rate at which the downstream pressures are affected by the rapid reattachment of the shear layer are shown in Figure 5.19. These contour maps, shown in Figure 5.19, indicate that both the time at which the changes start

and over which they occur and the rate of change (the magnitude in the contour plot) are not only strong functions of the pressure ratio, but are tied to the formation of the shock, and the point at which the facility chokes. These pressure gradient maps, along with the shock positions (Figure 5.18 and 5.19), provide insight into the timing, actuation location, actuator response rate and feedback rate that would be an integral part of a closed loop flow control system to control the shock position. The next step in developing such a system is investigation of the effects of repeated actuation pulses.

The response time (or delay) of the shock to the onset and termination of the actuation is investigated by repetitive actuation. When the repetition frequency is increased, attachment of the separated shear layer and the shock migrate downstream and oscillate about that point at the actuation frequency, but without full detachment and regression between pulses. As was the case in the pulsed actuation, it is also shown that the cyclic pulsed flow actuation leads to a momentary attachment of the separated shear layer. This, in turn, alters the downstream pressure and effects a significant synchronized streamwise translation of the shock, which is then followed by a longer relaxation as the surface vorticity layer re-separates over the jet inactive portion of the actuation cycle. Hysteresis associated with the repetitive actuation is shown to decrease with increasing pressure ratio (cf. Figure 6.10 and 6.11) however, the changes imparted during the onset portion of the flow control cycle are more rapid than the shock can respond to over all of the pressure ratios tested, indicating high enough response rate of the flow control during this portion of the cycle, with the opposite being true for the portion of the cycle associated with the termination of the flow control.

The characteristic time of the controlled shock motion in the present investigation is on the order of 0.5 ms. This indicates that active stabilization of the shock, or changes in its position in internal flows can be controlled with bandwidth of about 1-2 kHz, and may also apply to control of shock waves in external aerodynamic applications. The time scales to which the shock is naturally susceptible in this transonic regime have been

investigated by a number of authors. The interaction between a normal shock and a turbulent boundary layer at high transonic speeds was examined by Messiter (1980), where the pressure distributions which are associated with these interactions were derived both using asymptotic methods and review of experimental investigations. An analytical investigation of unsteady transonic flows (Adamson, 1971) indicates the motion of the transonic region and the time scales of the motions depend on a number of parameters, such as surface curvature, Mach number, gas properties etc. Tijdeman (1977), divided the periodic motion of the shock over an airfoil into three categories based on the shock strength. The shock disappears during certain portions of the cycle at higher frequencies (eg. 120 Hz for a $\delta M_1/\delta x$ of 3), due to the decrease in the upstream (oncoming) relative velocity. A similar effect is expected at lower free stream Mach numbers. The receptivity of the flow is therefore a function of $\delta M_1/\delta x$ and the free stream Mach number for external flows. It is expected that similar trends hold for internal flows in Chapters 5 and 6, when the pressure ratio is sufficiently low to maintain the pre-choked flow (cf. Figure 2.5).

The flow control concepts developed in the present investigations were demonstrated in two challenging high speed internal flows. The first application is that of improving the flow through an aggressively shortened thrust reversing duct and the second is controlling the dynamics of an unsteady and unstable secondary flow in an offset diffuser duct.

In the thrust reverser duct a reduction in the streamwise length of the internal flow turning surface (the bullnose) is limited by flow separation. The present investigations demonstrated that active control of the separation by using fluidic actuation can significantly reduce the losses within the duct and at its exit plane and thereby increase the flow rate through the duct and the effective open area of the exit plane compared to the base configuration in which the length of the flow turning surface is relaxed to avoid separation. These investigations yielded a range of operational parameters that related

the characteristic dimensions of the flow surface and the magnitude of the actuation to the performance of the duct to compute its benefits during system studies.

Flow control was also utilized for mitigation of flow distortion in offset ducts, when the adverse pressure gradient does not induce separation but intensifies the formation of secondary flow structures. Hybrid (passive vortex generators coupled with synthetic jet actuators) actuation led to relaxation of the streamwise vortical structures, as evidenced by significant reduction in the flow distortion (up to 27%). The investigations demonstrated that the time-invariant effects of the vortex generator arrays was comparable to the time-periodic effects of the jets (which produce less drag). Therefore, it is argued that the full potential of the active flow control can be realized by overcoming the characteristic flow relaxation time between successive actuation vortices, based on the flow-relevant time scales as can be achieved at higher actuation frequencies. However at larger scales (scales > 3x), the actuation method presented here would be suitable for the convective times associated with the transit through the duct to the AIP.

The present results indicate that hybrid actuation can enable the design of more aggressive, serpentine diffusers by utilizing a control system that is both fail safe (passive) and does not require bleed air (synthetic jets).

9.3 Applications and Recommendations

Following the present demonstration of control authority in open-loop control of the position and stability of a transonic shock in internal duct flow, a closed loop controller should be developed to fully realize the advantages of the present control scheme. The present work demonstrated the feasibility of such a system and identified the relevant time scales and appropriate actuators and sensors including their placement. Furthermore, the present results can also be extended to address problems that involve shock-induced separation and shock stability in external aerodynamics.

Another area that merits further investigations is the extension of the present work to 3-D actuation effects such as edge effects of a nominally 2-D actuator array, actuation spacing, and discrete actuation. This study can lead to optimization of the flow control effectiveness and reduce the required actuation power.

REFERENCES

Ackeret, J. Feldmann, F. and K. Rott, "Investigations of Compression Shocks and Boundary Layers in Gases Moving at High Speed," NACA TM 1113 (1947).

Adamson Jr. T.C. and Messiter, A.F. "Analysis of Two-Dimensional Interactions Between Shock Waves and Boundary Layers," Ann. Rev. Fluid Mech. 12 103-138 (1980).

Amitay, M. Smith, B.L. Glezer, A. "Aerodynamic Flow Control Using Synthetic Jet Technology," AIAA 98-0208, (1998)

Amitay, M., Pitt, D., Glezer, A. (2002) "Separation Control in Duct Flows," J. Aircraft., 39(4): 616-620.

Anabtawi, A.J., Blackwelder, R.F, Liebeck, R.H., and Lissaman, P.B.S. (1999) "An Experimental Study of the Effect of Offset on Thick Boundary Layers Flowing Inside Diffusing Ducts." AIAA Paper 99-3590.

Anabtawi, A.J., Blackwelder, R.F., Lissaman, P. B.S., and Liebeck, R.H., (1999) "An Experimental Investigation of Boundary Layer ingestion in a Diffusing S-Duct With and Without Passive Flow Control," AIAA Paper 99-0739.

Anderson, B.H., Gibb, J. (1993) "Study on Vortex Generator Flow Control for the Management of Inlet Distortion," J. Prop. Power 9(3): 422-430.

Anderson, B.H., Mace, J.L., and Mani, M., (2009) "Active "Fail Safe" Micro-Array Flow Control For Advanced Embedded Propulsion Systems," AIAA Paper 2009-741.

Anderson, B.H., Miller, D.N., Addington, G.A., Agrell, J. (2004) "Optimal Micro-Vane Flow Control for Compact Air Vehicle Inlets," NASA/TM.2004-212936.

Anderson, B.H., Miller, D.N., Addington, G.A., Agrell, J. (2004) "Optimal Micro-Jet Flow Control for Compact Air Vehicle Inlets," NASA/TM.2004-212937.

Andreopoulos J. and Muck, K.C. "Some New Aspects of the Shock-Wave/Boundary-Layer Interaction in Compression-Ramp Flows," J. Fluid Mech. 180 405-428 (1987).

Arbiter D.G. Nasa Contractor Report 178036

Arwatz, G. Fono, I. Seifert, A. "Suction and Oscillatory Blowing Actuator," IUTAM, Symposium on Flow Control and MEMS, 19-22 Sept, 2006.

Ashill, P.R. Fulker, J.L. and Hackett, K.C. "Research at DERA on Sub Boundary Layer Vortex Generators (SBVGs)," AIAA 2001-0887 (2001).

Babinsky H. and Harvey J. K. Shock Wave-Boundary-Layer Interactions (Cambridge University Press, (2011).

Bansod, P., Bradshaw, P. (1972) "The Flow in s-shaped Ducts," Aeronaut. Quart., 23: 131-140.

Barakos, G. Huang, J.C. Benard, E. Yapalparvi, R. Raghunathan, S. "Investigation of Transonic Flow over a Bump: Base Flow Control," AIAA 2008-357 (2008).

Barter, J.W. and Dolling, D.S. "Experimental Study of the Use of Vortex Generators to Reduce Fluctuating Pressure Loads in Shock Wave Turbulent Boundary Layer Interactions," AIAA 1993-4335 (1993).

Beresh, S.J. Henfling, J.F. Spillers, R.W. Pruett, B.O.M. "Unsteady Shock Motion in a Transonic Flow over a Wall-Mounted Hemisphere," AIAA 2013-3201 (2013).

Berkooz, G., Holmes, P., and Lumley, J. L., (1993) "The Proper Orthogonal Decomposition in the Analysis of Turbulent Flows" Ann. Rev. Fluid Mech., 25: 539-575.

Berrier, B.L., Allan, B.G. (2004) "Experimental and Computational Evaluation of Flush-Mounted, S-Duct Inlets," AIAA Paper 2004-764.

Bons, J.P. Sondergaard, R. River, R. B. "Turbine Separation Control Using Pulsed Vortex Generator Jets," ASME 123, April. (2001).

Bruce, E.P. (1974) "Design and Evaluation of Screens to produce Multi-cycle +/- 20% Amplitude Sinusoidal Velocity Profiles," AIAA Paper 74-623.

Bushnell, D. M. "Shock Wave Drag Reduction," Annual Review of Fluid Mechanics, Vol. 36, 2004, pp. 81-96.

Chiekh, M. B., Béra, J.-C., and Sunyach, M., (2003) "Synthetic jet control for flows in a diffuser: vectoring, spreading and mixing enhancement", J. Turbulence 4: 032.

Crittenden, T. and Glezer, A., "A High-Speed Compressible Synthetic Jet," Physics of Fluids, Vol. 18, No. 1, 017107, 2006.

Crouch, J.D. Garbaruk, A. Magidov, D. Travin, A. "Origin of Transonic Buffet on aerofoils," J. Fluid Mech. 628, pp 357-369, (2009).

Delery, J. M. "Experimental Investigation of Turbulence Properties in Transonic Shock/Boundary-Layer Interactions," AIAA J. 21 180-185 (1983).

Delery, J. M. "Shock Wave/Turbulent Boundary Layer Interaction and its Control," Prog.Aero.Sci.22, 209-280 (1985).

DeSalvo, M. Whalen, E. Glezer, A. "High-Lift Enhancement using Fluidic Actuation," AIAA 2010-863, (2010).

Dietrich D. and Gutierrez O. "Performance of a Cascade Thrust Reverser for Short-Haul Applications," J. Air.13 185-191 (1976).

Dagget, D. L., Kawai, R., and Friedman, D. (2003) "Blended Wing Body Systems Studies: Boundary Layer Ingestion Inlets With Active Flow Control", NASA CR212670.

Englar, R. J. "Two-Dimensional Transonic Wind Tunnel Tests of Three 15-percent Thick Circulation Control Airfoils," NSRDC T.N. AL-182 (1970).

Ferri, A. "Experimental Results with Airfoils Tested in the High-Speed Tunnel at Guidonia," NACA T.M. 946 (1939).

Gerlach, C. R. and Schroeder, E. C., (1969) "Study of Minimum Pressure Loss in High Velocity Duct Systems," NASA CR-102499.

Gissen, A. N., Vukasinovic, B., and Glezer, A. (2009) "Controlled Streamwise Vorticity in Diffuser Boundary Layer using Hybrid Synthetic Jet Actuation" AIAA Paper 2009-4021.

Gissen, A. N., Vukasinovic, B., and Glezer, A. (2010) "Manipulation of Streamwise Vorticity in an Emulated Diffuser Boundary Layer Using Hybrid Flow Control" AIAA Paper 2010-4586.

Gissen, A. N., Vukasinovic, B., McMillan, M. L., and Glezer, A. (2014) "Distortion Management in a Boundary Layer Ingestion Inlet Diffuser using Hybrid Flow Control." J. Prop. Power, 30: 3, May-June 2014.

Glezer, A., and Amitay, M. (2002) "Synthetic Jets," Annu. Rev. Fluid Mech., 34: 503-529.

Glezer, A. Amitay, M. "Synthetic Jets," Annu. Rev. Fluid Mech. 34, 503-529 (2002).

Glezer, A. "Some aspects of aerodynamic flow control using synthetic-jet actuation," Phil. Trans. R. Soc. 369, 1476-1494, (2011).

Godard, G. and Stanislas, M. (2006) "Control of a decelerating boundary layer. Part 1: Optimization of passive vortex generators," Aerosp. Sci. Technol., 10: 181-191.

Gordeyev, S. Burns, R. Jumper, E. Gogineni, S. Paul, M. and Wittich, D. "Aero-Optical Mitigation of Shocks Around Turrets at Transonic Speeds Using Passive Flow Control," AIAA 2013-0717 (2013).

Gregory, J.W. Tomac, M.N. "A Review of fluidic Oscillator Development and Application for Flow Control," AIAA 2013-2474 (2013).

Gregory, J.W. "A Review of Fluidic Oscillator Development and Application for Flow Control," AIAA 43rd Fluid Dynamics Conference June 24-27 2013 San Diego 2013-2474

Hadjadj, A. Onofri, M. "Nozzle Flow Separation," Shock Waves, 19, 163-169, (2009).

Hall, S. Cooper R. and Raghunathan S. "Fluidic Flow Control of a Natural Blockage Thrust Reverser," AIAA Conf. San Francisco CA June 2006.

Harrison, N. A., Anderson, J., Fleming, J. L., and Ng, W. F., (2013) "Active Flow Control of a Boundary Layer-Ingesting Serpentine Inlet Diffuser", J. Aircraft, 50(1): 262-271.

Hegen G.H. and Kooi J.W. "Investigation of Aricraft Performance with Deployed Thrust Reversers in DNW," AIAA conf. Tucson AZ July 2005.

Holman, R. Utturkar, Y. Mittal, R. Smith, B. Cattafesta, L. "Formation Criterion for Synthetic Jets," AIAA J. 43, 10, (2005).

Holden H. and Babinsky, H. "Effect of Microvortex Generators on Separated Normal Shock/Boundary Layer Interactions," J. Aircraft 44 170-174 (2007).

Jacquin, L. Molton, P. Deck, S. Maury, B. Soulevant, D. “Experimental Study of Shock Oscillation over a Tranosnic Supercritical Profile,” AIAA Journal, 47, 9, Sept. (2009).

Jirásek, A., (2006) “Development and Application of Design Strategy for Design of Vortex Generator Flow Control in Inlets,” AIAA Paper 2006-1050.

Johns, C. J. “Solution of an engine inlet compatibility problem during C-17 low cost N/EAT nacelle thrust reverser development”. AIAA-2000-5579. 2000 World Aviation Conference, San Diego, CA, Oct. 10-12.

John, J.E., Keith, T. G. *Gas Dynamics*, 3rd edition, Prentice Hall, Upper Saddle River NJ.07458, 2006.

Kaldschmidt, G., Syltebo, B.E., and Ting, C.T. (1974) “727 Airplane Center Duct Inlet Low-Speed Performance Confirmation model Test for Refanned JT8D Engines Phase II.” NASA CR-134534.

Kalra, C.S Shneider, M.N. and Miles, R.B. “Numerical Study of Boundary Layer Separation Control Using Magnetogasdynamic Plasma Actuators,” Phys. Fluids 21 106101 (2009).

Kalra, C.S. Zaidi, S.H. Miles, R.B. and Macheret, S.O. “Shockwave–Turbulent Boundary Layer Interaction Control Using Magnetically Driven Surface Discharges,” Exp. in Fluids 50 547-559 (2011).

Kawai, R. T., Friedman, D. M., and Serrano, L. (2006) “Blended Wing Body (BWB) Boundary Layer Ingestion (BLI) Inlet Configuration and System Studies,” NASA CR-214534.

Kibens, V. William, B. “An Overview of Active Flow Control Applications at The Boeing Company,” AIAA 2004-2624. (2004).

Kostas, J. Foucaut, J.M. Stanislas, M. “The Flow Structure Produced by Pulsed-jet Vortex Generators in a Turbulent Boundary Layer in an Adverse Pressure Gradient,” Flow Turbulence Combust, 78, pp 331-363. (2007).

Kohl R. and Algranti J.S. “Investigation of a Full-Scale, Cascade-Type Thrust Reverser,” NACA TN # 3975, April 1957.

Krogmann, P. Stanewsky, E. and Thiede, P. “Effects of Suction on Shock/Boundary-Layer Interaction and Shock-Induced Separation,” J. Aircraft 22 37-42 (1985).

Kundar, K.L. Carpenter, P.W. “Numerical Investigation and Feasibility Study of a PZT-driven Micro-valve Pulsed-jet Actuator,” Flow Turbulence Combust, 78, pp 223-254 (2007).

Kurzke, J. (2008) “Effects of Inlet Flow Distortion on the Performance of Aircraft Gas Turbines.” J. Eng. Gas Turb. Power 130: 041201.

Kyrazis, D.T. “Airborne Laser Laboratory departure from Kirtland Air Force Base and a brief history of aero-optics,” Optical Engineering 52, 7, July (2013).

Lee, B.H.K. “Self-sustained shock oscillations on airfoils at transonic speeds,” Prog.Aero.Sci.37, pp 147-196, (2001).

Lee, S. Loth E. and Babinsky, H. “Normal Shock Boundary Layer Control with Various Vortex Generator Geometries,” Comput. Fluids 49 233-246 (2011).

Liebeck, R.H. (2004) “Design of the Blended Wing Body Subsonic Transport,” J. Aircraft., 41(1): 10-25.

Liepmann, H. W. “Interaction between boundary layer and shock waves in transonic flow,” J. Aero.Sci.13, 623-637 (1946).

Liepmann, H. W. Roshko, A. and Dhawan, S. “On reflection of shock waves from boundary layers,” Nat. Adv. Comm. Aero.1100 889-917 (1951).

Lin, J.C. (2002) “Review of research on low-profile vortex generators to control boundary-layer separation,” Prog. Aerosp. Sci. 38(4-5): 389-420.

Liu X. and Squire, L.C. “An Investigation of shock/boundary-layer interactions on curved surfaces at transonic speeds,” J. Fluid Mech. 187 467-486 (1987).

McManus, K. Magill, J. “Separation control in incompressible and compressible flows using pulsed jets,” AIAA 96-1948, (1996)

McMillan, M.L. Mackie, S.A. Gissen, A. Vukasinovic, B. Lakebrink, M.T. Glezer, A. Mori, M. Mace, J.L. “Inlet Flow Control and Prediction Technologies for Embedded Propulsion Systems,” NASA TR #20120002597, 2012.

Narayanaswamy, V. Clemens, N.T. and Raja, L.L. “Investigation of a Pulsed-Plasma Jet for Shock / Boundary Layer Control,” AIAA 2010-1089 (2010).

Nave L.H. and Coffey, G.A. "Sea Level Side Loads in High-Area-Ratio Rocket Engines," AIAA 9th Propulsion Confernce, Nov. 5-7, (1973).

Owens, L.R., Allan, B.G., Gorton, S.A., (2008) “Boundary-Layer-Ingesting Inlet Flow Control,” J. Aircraft., 45(4): 1431-1440.

Pearcey, H.H. Holder, DW. “Examples of the Effects of Shock-Induced Boundary Layer separation in Transonic Flight,” Ministry of Tech. ARC 3510 (1954).

Raghu, S. “Feedback-Free Fluidic Oscillator and Method,” U.S. Patent No. 6,253,782, issued Jul. 3, 2001.

Raghu, S. “Fluidic oscillators for flow control,” Exp. in Fluids, Vol. 54, 2, (2013).

Raman, G. Raghu, S. “Cavity Resonance Suppression Using Miniature Fluidic Oscillators,” AIAA J. 42, 12 (2004).

Reichert, B. A., and Wendt, B. J. (1996) “Improving Curved Subsonic Diffuser Performance with Vortex Generators.” AIAA J., 34(1):65-72.

Sartor, F. Losfeld, G. Bur. R. “PIV study on a shock-induced separation in a transonic flow,” Exp Fluids 53 815-827 (2012).

Sartor, F. Losfeld, G. Bur, R. “PIV study on a shock-induced separation in a transonic flow,” Exp Fluids. Vol. 53, 2012, pp. 815-827.

Scribben, A.R., Ng, W., Burdisso, R., (2006) “Effectiveness of a Serpentine Inlet Duct Flow Control Technique at Design and Off-Design Simulated Flight Conditions,” J. Turbomach., 128(2): 332-339.

Seifert, A. Bachar, T. Koss, D. Shepshelovich, M. Wygnanski, I. “Oscillatory Blowing: A Tool to Delay Boundary-Layer Separation,” 31, 11, Nov. (1993).

Seifert, A. Pack, L.G. “Active Flow Separation Control on Wall-Mounted Hump at high Reynolds Numbers,” AIAA J. 40, 7, 2002.

Seifert. A. “Closed-Loop Active Flow Control Systems: Actuators,” Active Flow Control 2006, Berlin Sept 27-29, (2006).

Smith, T.E. Patent #4047381 granted Sept 13 1977.

Smith, L. H. (1993) “Wake Ingestion Propulsion Benefit,” J. Propul. Power 9(1): 74-82.

Smith, B.L. Glezer, A. “The formation and evolution of synthetic jets,” Phys. of Fluids.10, 9, Sept. (1998).

Souverein L.J. and Debieve, J.F. “Effect of Air Jet Vortex Generators on a Shock Wave Boundary Layer Interaction,” Exp. in Fluids 49 1053-1064 (2010).

Society of Automotive Engineers Aerospace Recommended Practice 1420 Revision B, 2002-03-01

Stainback, P.C, Nagabushana, K.A. “Review of Hot-Wire Anemometry Techniques and the Range of their Applicability for Various Flows,” Electronic Journal of Fluids Engineering, Transactions of the ASME 1990.

Stanewsky, E. Delery, J. Fulker, J. and Matteis, P. Drag Reduction by Shock and Boundary Layer Control (Springer, 2002).

Törnblom, O. and Johansson, A. V., (2007) “A Reynolds stress closure description of separation control with vortex generators in a plane asymmetric diffuser”, Phys. Fluids, 19(11): 115108.

Tournier, S.E., Paduano, J.D., and Pagan, D. (2005) “Flow Analysis and control in a Transonic Inlet,” AIAA Paper 2005-4734.

Tichener, N. Babinsky, H. “Shock Wave/Boundary-Layer Interaction Control Using a combination of Vortex Generators and Bleed,” AIAA J. 51, 5 1221-1233 (2013).

Tijdeman, H., “Investigation of the Transonic Flow Around Oscillating Aero-foils,” Nation Aerospace Lab., Amsterdam, The Netherlands, TR-77-090U, 1977.

Verma, S.B. "Shock unsteadiness in a thrust optimized parabolic nozzle," Shock Waves, 19, 193-212, (2009).

Vukasinovic, B. Glezer, A. Gordeyev, S. Jumper, E. and Bower., W. “Flow Control for Aero-Optics Application,” Exp. Fluids 50:1492, 2013.

Vukasinovic, B. Gissen, A.N. Glezer, A. and Gogineni, S. “Fluidic Control of Transonic Shock-Induced Separation,” AIAA 2013-0529 (2013).

Wallis R.A. and Stuart, C.M. “On the Control of Shock-Induced Boundary-Layer Separation with Discrete Air Jets,” AARC C.P. No. 595 (1958).

Wallis, R.A. Stuart, C.M. “On the Control of Shock-Induced Boundary-Layer Separation with Discrete Air Jets,” ARC, 595, (1962).

Wood S. K. and McCoy J. “Design and Control of the 747 Exhaust Reverser Systems,” SAE National Air Trans. Mtg. April 1969.

Vaccaro, J. C., Sahni, O., Olles, J., Jansen, K.E., and Amitay, M., (2009) “Experimental and Numerical Investigation of Active Control of Inlet Ducts.” Int. J. Flow Control, 1(2): 133-154.

Vakili, A., Wu, J. M., Liver, P., and Bhat, M. K. (1983) “Measurements of Compressible Secondary Flow in a Circular S-Duct.”, AIAA Paper 83-1739.

Vakili, A.D., Wu, J. M., Liver, P., and Bhat, M. K. (1985) “Flow Control in a Diffusing S-Duct.” AIAA Paper 85-0524.

Wellborn, S.R., Reichert, B.A., and Okiishi, T.H. (1992) “An Experimental Investigation of the Flow in a Diffusing S-Duct.” AIAA Paper 92-3622.

Woo, G. T. K., Crittenden, T., and Glezer, A., (2009) “Transitory Separation Control over a Stalled Airfoil,” AIAA Paper 2009-4281.